

7-20-05

1745

IFW

\$ ec

Applicant : Ralph, et al  
 Publication. No. : US 2005/0106447  
 Publication Date : 5/19/05  
 Title : IRON-BASED PEROVSKITE CATHODES FOR SOLID OXIDE FUEL CELLS  
 TC/A.U. : 1745  
 Examiner : Melissa J. Austin  
 Docket No. : 279  
 Customer No. :

RECEIVED

JUL 25 2005

IN THE UNITED STATES PATENT AND TRADEMARK OFFICE **TC 1700**

MAIL STOP AMENDMENT  
 COMMISSION FOR PATENTS  
 P.O. BOX 1450  
 ALEXANDRIA, VA 22313-1450

EXPRESS MAIL MAILING LABEL	
NUMBER:	EV 629 093 190 US
DATE OF DEPOSIT:	July 19, 2005
PURSUANT TO 37 C.F.R. § 1.10, I HEREBY CERTIFY THAT I AM PERSONALLY DEPOSITING THIS PAPER OR FEE WITH THE U.S. POSTAL SERVICE, "EXPRESS MAIL POST OFFICE TO ADDRESSEE" SERVICE ON THE DATE INDICATED ABOVE IN A SEALED ENVELOPE (A) HAVING THE ABOVE-NUMBERED EXPRESS MAIL LABEL AND SUFFICIENT POSTAGE AFFIXED, AND (B) ADDRESSED TO THE COMMISSIONER FOR PATENTS, MAIL STOP AMENDMENT; P.O. BOX 1450, ALEXANDRIA, VA 22313-1450.	
07/19/2005	 DAVID M. HOFFMAN
DATE	

## THIRD-PARTY SUBMISSION IN A PUBLISHED APPLICATION UNDER 37 CFR 1.99

Enclosed herewith is a listing and copy of references relevant to the published application listed above, together with the processing fee required under 37 CFR 1.17(p). The list of the references for the Examiner to consider is attached in Appendix A.

Accordingly, it is respectfully suggested that each of the requirements under 37 CFR 1.99 have been met with this Third Party Submission of Prior Art in a Published Application, as follows: this Submission has properly identified the application to which it is directed by application number (US 2005/0106447 entitled, "IRON-BASED PEROVSKITE CATHODES FOR SOLID OXIDE FUEL CELLS," having a serial number of 10/716,331, a publication date of May 19<sup>th</sup>, 2005 and a filing date of November 18<sup>th</sup>, 2003); the fee as set forth in 1.17(p) for \$180.00 accompanies the submission; a list of the patents or publications has been submitted for consideration by the Office, including the date of publication of each patent or publication in Appendix A; and a copy of each listed patent or publication in has been provided in the English language and in written form.

STATEMENT OF SERVICE: I hereby state that a copy of this submission and related references has been served upon the Applicant's attorney via Certified First Class Mail on July 19, 2005, in accordance with 37 CFR 1.248.

It is respectfully requested that the Examiner enter the references identified in Appendix A in the application file associated with publication US 2005/0106447.

07/21/2005 SSITHIB1 00000017 10716331

01 FC:1806

180.00 OP

Dated: July 19, 2005

Respectfully submitted,

  
 David Hoffman, Reg. 54,174  
 P. O. Box 692289  
 Houston, TX 77269-2289

OK X  
 Wm. W. Miller  
 C. Mills

CC: **VIA FIRST CLASS MAIL ON 7/19/05:**

James J. Hill  
 Emrich & Dithmar, LLC  
 125 South Wacker Drive, Suite 2080  
 Chicago, IL 60606-4401

GREGORY MILLS  
 QUALITY ASSURANCE SPECIALIST

## RECEIVED

Sheet 1 of 1

SUBSTITUTE FORM PTO-1449

JUL 25 2005

U.S. DEPARTMENT OF COMMERCE  
PATENT AND TRADEMARK OFFICEATTY. DOCKET NO.  
279SERIAL NO.  
10/716,331TC 1700  
APPENDIX A

## INFORMATION DISCLOSURE STATEMENT

LIST OF ITEMS

Applicant

JAMES RALPH, ET AL

Filing Date  
11/18/03Group  
1745

## U.S. PATENT DOCUMENTS

*EXAMINER INITIAL	DOCUMENT NUMBER	DATE	NAME	CLASS	SUBCLASS	FILING DATE IF APPROPRIATE
AA						
AB						

## FOREIGN PATENT DOCUMENTS

		DOCUMENT NUMBER	DATE	COUNTRY	CLASS	SUBCLASS	TRANSLATION YES NO
	BA						

## OTHER INFORMATION (Including Author, Title, Date, Pertinent Pages, etc.)

CA	S. Tanasescu, et al, "The Influence of Compositional Variables on the Thermodynamic Properties of Lanthanum Strontium Ferrite Manganites and Lanthanum Strontium Manganites", Materials Research Bulletin, Vol.32, No. 7, pp. 915-923, 1997.
CB	F. Zeng, et al, "Phase Behavior of Lanthanum Strontium Manganites", Journal of the Electrochemical Society, 146 (8), pp. 2810-2816, 1999.
CC	S. Badawal, et al, "Chemical Diffusion in Perovskite Cathodes of Solid Oxide Fuel Cells: the Sr doped LaMn <sub>1-x</sub> M <sub>x</sub> O <sub>3</sub> (M=Co, Fe) systems, Ceramics International 27, pp. 419-429, 2001.
CD	G. Kostoglouidis, et al, "Properties of A-site-deficient La <sub>0.6</sub> Sr <sub>0.4</sub> Co <sub>0.2</sub> Fe <sub>0.8</sub> O <sub>3-δ</sub> -based perovskite oxides", Solid State Ionics 126, pp. 143-151, 1999.
CE	R. Doshi, et al, "Development of Solid-Oxide Fuel Cells That Operate at 500°C", Journal of The Electrochemical Society, 146 (4), pp. 1273-1278, 1999.
CF	L. Kindermann, et al, "Chemical compatibility of the LaFeO <sub>3</sub> be perovskites (La <sub>0.6</sub> Sr <sub>0.4</sub> ) <sub>z</sub> Fe <sub>0.8</sub> M <sub>0.2</sub> O <sub>3-δ</sub> (z= 1, 0.9; m=Cr, Mn, Co, Ni) with yttria stabilized zirconia", Solid State Ionics 89, pp. 215-220, 1996.
CG	D. Fagg, et al, "Redox behavior and transport properties of La <sub>0.5-x</sub> Sr <sub>0.5-x</sub> Fe <sub>0.4</sub> Ti <sub>0.6</sub> O <sub>3-δ</sub> (0<x<0.1) validated by Mossbauer spectroscopy", Solid State Ionics 146, pp. 87-93, 2002.
CH	D. Waller, et al, "The effect of thermal treatment on the resistance of LSCF electrodes on gadolinia doped ceria electrolytes", Solid State Ionics 86-88, pp. 767-772, 1996.
CI	S. Otoshi, et al, "Changes in the Phases and Electrical Conduction Properties of (La <sub>1-x</sub> Sr <sub>x</sub> ) <sub>1-y</sub> MnO <sub>3-δ</sub> ", J. Electrochem. Soc. Vol. 138, No. 5, pp. 1519-1523, May 1991.
CJ	"S. Simner, et al, Development of lanthanum ferrite SOFC cathodes", Journal of Power Sources 113, pp. 1-10, 2003.

EXAMINER	DATE CONSIDERED

EXAMINER: Initial if reference considered, whether or not citation is in conformance with MPEP 609; Draw line through citation if not in conformance and not considered. Include copy of this form with next communication to applicant



Pergamon

Materials Research Bulletin, Vol. 32, No. 7, pp. 915-923, 1997  
Copyright © 1997 Elsevier Science Ltd  
Printed in the USA. All rights reserved  
0025-5408/97 \$17.00 + .00

PII S0025-5408(97)00054-8

## THE INFLUENCE OF COMPOSITIONAL VARIABLES ON THE THERMODYNAMIC PROPERTIES OF LANTHANUM STRONTIUM FERRITE MANGANITES AND LANTHANUM STRONTIUM MANGANITES

S. Tanasescu, N.D. Totir, D.I. Marchidan and A. Turcanu

Institute of Physical Chemistry, Splaiul Independentei 202, 77208 Bucharest, Romania

(Refereed)

(Received October 7, 1996; Accepted March 11, 1997)

### ABSTRACT

In order to obtain a better understanding of the stability limits of perovskite phases used in new SOFC (solid oxide fuel cell) cathodes materials, a study of the thermodynamic properties of some perovskite-type oxides based on lanthanum strontium ferrite manganite and lanthanum strontium manganite was initiated. For the determination of thermodynamic quantities, a solid state electrochemical technique has been employed. The relative partial molar free energies, enthalpies, and entropies of oxygen dissolution in the perovskite phase, as well as the partial pressures of oxygen, have been obtained in the temperature range of 1073–1273 K. The results evidence the influence of different compositional variables on the thermodynamic properties. © 1997 Elsevier Science Ltd

**KEYWORDS:** A. ceramics, A. oxides, C. electrochemical measurements, D. thermodynamic properties

### INTRODUCTION

The composite materials based on lanthanum strontium manganite and lanthanum strontium ferrite manganite are receiving considerable attention because of promising application as cathodes for solid oxide fuel cells. Besides the determination of their electrical and structural characteristics, a thorough knowledge of the chemistry and thermodynamics of the new materials is very important. Except for theoretical (1–3) and experimental (4–6) studies regarding the phase stability and thermodynamic properties of the perovskite-type oxides  $\text{La}_{1-x}\text{Sr}_x\text{MnO}_{3+\delta}$ , the literature data are lacking concerning the thermodynamic data of multicomponent oxides based on lanthanum strontium ferrite manganite.

As we showed in a previous paper (6), the thermodynamic stability limits of nonstoichiometric lanthanum manganites and lanthanum strontium manganites are conveniently situated within the range of oxygen chemical potentials which can be measured by galvanic cells incorporating a  $ZrO_2(Y_2O_3)$  solid electrolyte and an iron-wüstite reference electrode.

In the present study, new measurements have been made by using EMF solid electrolyte galvanic cells method in order to characterize from the thermodynamic point of view the perovskite-type materials of general formula  $La_{1-x}Sr_xMn_{1-y}Fe_yO_3$ ,  $(La_{1-x}Sr_x)_{0.95}Mn_{1-y}Fe_yO_3$ , and  $(La_{1-x}Sr_x)_{0.95}MnO_3$ . The relative partial molar free energy, enthalpy, and entropy of oxygen dissolution in the perovskite phase, as well as the partial pressure of oxygen, in the temperature range of 1073–1273 K were obtained. The results evidence the effect of the compositional variables x, y and of the overall A-site stoichiometry on the thermodynamic properties.

## EXPERIMENTAL

The design of the apparatus based on requirements following from the specific character of perovskite-type compounds and theoretical and experimental considerations related to the method applied are described elsewhere (7). Following are the principal characteristics:

- The geometry of the work cell ensures a compact electrode electrolyte assembly, so that temperature uniformity is easily reached and the extraneous thermoelectric potentials are minimized.
- The measurements are affected in vacuum at a residual gas pressure of  $10^{-4}$ – $10^{-5}$  Pa, after a previous rinsing of the installation with purified argon. The insulation of the electrodes in compartments which are separately evacuated and monitored for the gas pressure provides an adequate solution to remove the oxygen transfer between the electrodes through the gas.
- Prevention of signal pick-up from external heating sources is achieved by the use of a noninductive furnace and the earthed screening of cell and leads.

**Materials.** The solid electrolyte was a disc of 12.84 wt% yttria stabilized zirconia (10 mm diameter, 6 mm thick) supplied by Risø National Laboratory, Roskilde, Denmark. The powders of the specimens were supplied by Haldor Topsøe A/S, Lyngby, Denmark; their composition is listed in Table 1. The samples were prepared by drip pyrolysis, and the phase content (X-ray diffraction), specific area, carbon content, particle size, and elemental compositions were checked on the processed powders (8,9). All compositions investigated were single phase perovskites with rhombohedral (samples S1, S2, S4, S5, S6, S8) or orthorombic (samples S3, S7, S9) crystalline structure. The powders were pressed into small pellets (2 mm thick and 2 mm high) weighing 70 mg and were sintered at 1273 K in air for 4 h. The reference electrode was prepared from electrolytic iron and  $Fe_2O_3$  powders mixed in a molar ratio of 4:1, pressed at 15 MPa, and sintered at 1373 K in vacuum for 12 h.

**Measurements.** After the cell was rinsed with pure argon, the installation was emptied to  $10^{-4}$  Pa and slowly heated. The heating was gradually performed at a constant rate so that

TABLE 1  
Composition of the Samples

S1	$(La_{0.75}Sr_{0.25})_{0.95}Mn_{0.80}Fe_{0.20}O_3$
	$(La_{0.75}Sr_{0.25})_{0.95}Mn_{0.80}Fe_{0.20}O_2$
	$(La_{0.75}Sr_{0.25})_{0.95}Mn_{0.80}Fe_{0.20}O_3$
S2	$(La_{0.70}Sr_{0.30})_{0.95}Mn_{0.80}Fe_{0.20}O_3$
S3	$(La_{0.70}Sr_{0.30})_{0.95}Mn_{0.30}Fe_{0.70}O_3$
S4	$(La_{0.75}Sr_{0.25})_{0.95}MnO_3$
S5	$(La_{0.70}Sr_{0.30})_{0.95}MnO_3$
S6	$La_{0.70}Sr_{0.30}Mn_{0.80}Fe_{0.20}O_3$
S7	$La_{0.70}Sr_{0.30}Mn_{0.30}Fe_{0.70}O_3$
S8	$La_{0.70}Sr_{0.30}Mn_{0.50}Fe_{0.50}O_3$
S9	$La_{0.70}Sr_{0.30}Mn_{0.45}Co_{0.05}Fe_{0.50}O_3$

the rest of the pressure in the apparatus did not exceed  $10^{-3}$ – $10^{-4}$  Pa. The temperature gradient across the cell must be less than 1 K.

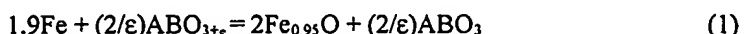
The EMF measurements were undertaken with a Keithley 197 microvoltmeter. The electromotive force was measured at increasing and decreasing temperature, within the 1073–1273 K range. The readings were made at 50 K intervals, every time waiting until the equilibrium values were recorded. The determinations were considered to be satisfactory when values for increasing and decreasing temperatures agreed within 1 or 2 mV. The potential was measured with the furnace on, since tests have shown that the variation of potential on switching off the furnace was only 0.05 mV.

## RESULTS AND DISCUSSION

For simplicity, we note with  $ABO_3$ , a  $(La, Sr)(Mn, Fe)O_3$  perovskite-type oxide, the overall reaction for the cell



can be written as follows:



where  $\varepsilon \rightarrow 0$  and  $\text{Fe}_{0.95}\text{O}$  is the approximate composition in equilibrium with iron at temperatures of about 1273 K.

The cell reaction is the sum of the two partial reactions:



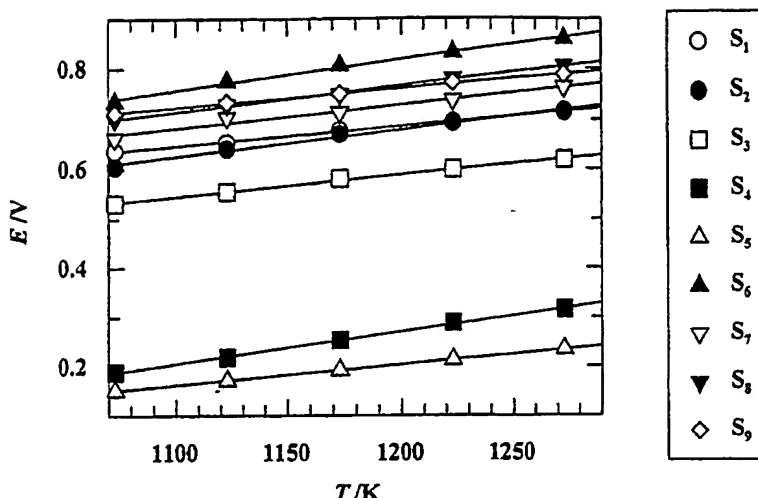


FIG. 1  
Electromotive force of the cells as a function of temperature.

Since the electrolyte of the cell shows only ionic conduction due to migration of oxygen ions in the electrolyte, the virtual cell reaction may be expressed in terms of oxygen transfer from the right-hand to the left-hand electrode. Hence, the EMF of the cell is

$$E = \frac{\mu_{O_2} - \mu_{O_2(\text{ref})}}{4F} \quad (4)$$

where  $\mu_{O_2}$  and  $\mu_{O_2(\text{ref})}$  are, respectively, the oxygen chemical potentials of the perovskite and of the reference electrode and  $F$  is the Faraday constant. Upon substituting the

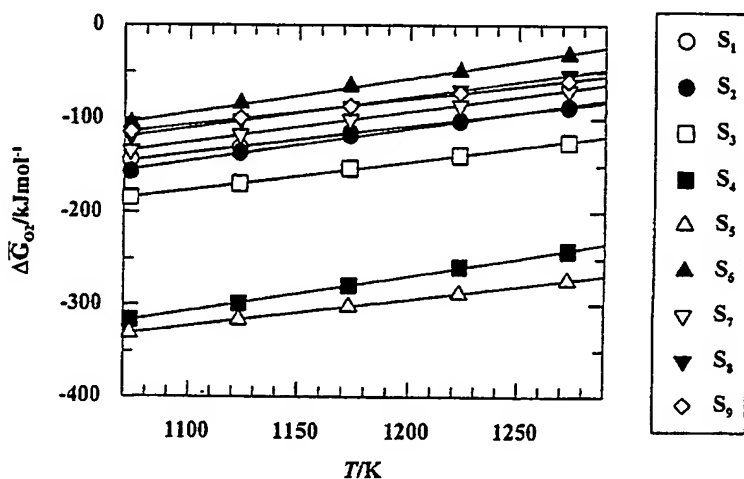


FIG. 2  
The variation of  $\Delta\bar{G}_{O_2}$  with the temperature for the selected compositions listed in Table 1.

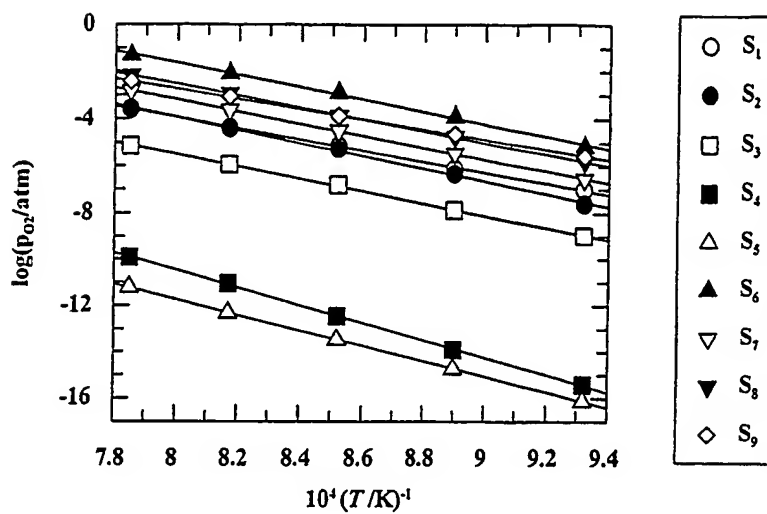


FIG. 3  
The plot of  $\log p_{O_2}$  vs.  $1/T$  for the selected compositions listed in Table 1.

experimental values of  $E$  in the above equation and knowing the free energy change of the reference electrode reaction evaluated from calorimetrically verified gas equilibrium measurements (10,11),

$$2\Delta G_{Fe, \text{wustite}} = [-529.15 + 0.131 T] \text{ kJ mol}^{-1} \quad (5)$$

the values of the relative partial molar free energy of the solution of oxygen in the perovskite phase and hence the pressures of oxygen in equilibrium with the solid can be calculated:

$$\Delta \bar{G}_{O_2} = RT \ln p_{O_2} \quad (6)$$

The relative partial molar enthalpies and entropies were obtained according to the known relationships:

$$\frac{\partial \frac{\Delta \bar{G}_{O_2}}{T}}{\partial T} = \frac{\Delta \bar{H}_{O_2}}{T^2} \quad (7)$$

$$\Delta \bar{G}_{O_2} = \Delta \bar{H}_{O_2} - T \Delta \bar{S}_{O_2} \quad (8)$$

The representative results for the selected compounds listed in Table 1 are depicted in Figures 1-6.

The overall uncertainty due to temperature and potential measurement (taking into account the overall uncertainty of a single measurement and also the quoted accuracy of

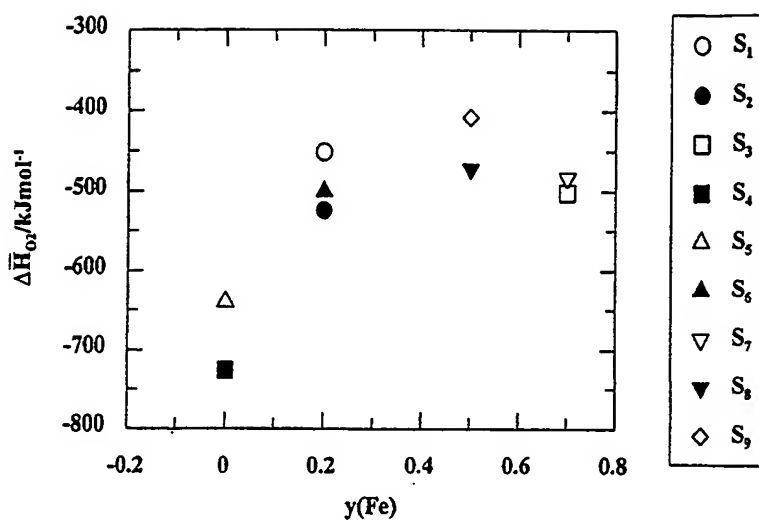


FIG. 4  
 $\Delta\bar{H}_{O_2}$  as a function of iron content for the selected compositions listed in Table 1.

the voltmeter) was  $\pm 1.5$  mV. This was equivalent to  $\pm 0.579$  kJ mol $^{-1}$  for the free energy change of the cell. Considering the uncertainty  $\pm 0.523$  kJ mol $^{-1}$  in the thermodynamic data for the iron-wüstite references (10,11), the overall accuracy of the data was estimated to be 1.6 kJ. For the enthalpies, the errors were  $\pm 0.45$  kJ mol $^{-1}$  and for the entropies,  $\pm 0.0011$  kJ mol $^{-1}$  K $^{-1}$ .

The variations of  $\Delta\bar{G}_{O_2}$  and  $\log p_{O_2}$  with temperature are presented in Figures 2 and 3. The partial molar free energy is a linear function of temperature. The partial molar entropies

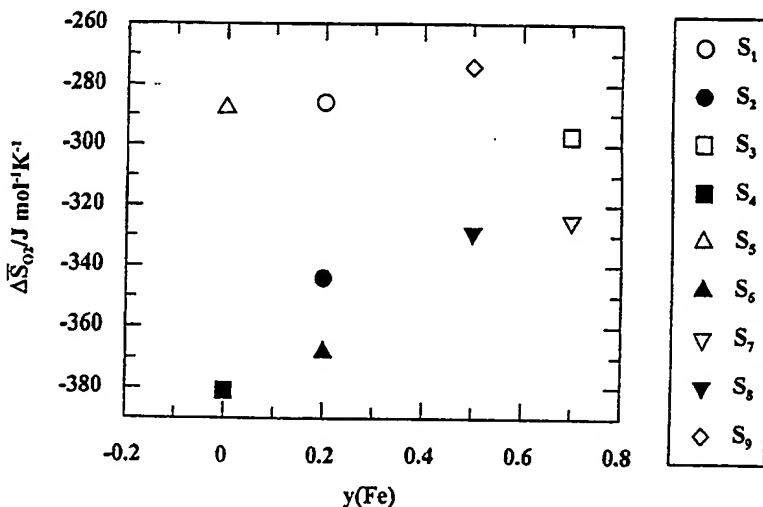


FIG. 5  
 $\Delta\bar{S}_{O_2}$  as a function of iron content for the selected compositions listed in Table 1.

and enthalpies are consequently independent of temperature. The calculated values of  $\Delta\bar{H}_{O_2}$  and  $\Delta\bar{S}_{O_2}$  are shown in Figures 4 and 5.

**Effect of A-Site and B-Site Doping on the Thermodynamic Properties.** The comparative study of the compounds  $LaMnO_3$  and  $La_{0.7}Sr_{0.3}MnO_3$  (6) showed that the presence of  $Sr^{2+}$  as A-site dopant is accompanied by an increase of the partial molar free energy and of the partial pressure of oxygen. This can be explained by the increase of the oxygen vacancies concentration when  $La^{3+}$  ions are replaced by  $Sr^{2+}$  ions.

As one can see in Figures 1-3, the two groups of lanthanum strontium manganites and lanthanum strontium ferrite manganites are distinguished very well by the EMF values and by their thermodynamic data.

In the group of the lanthanum strontium manganites (samples S4 and S5), a small variation in the strontium content of 5% gives a distinct change of partial molar quantities, which is more evident at higher temperatures. Thus, between the corresponding  $\Delta\bar{G}_{O_2}$  values for the samples S4 and S5, a difference of  $\sim 14 \text{ kJ mol}^{-1}$  is observed at 1073 K, while at 1273 K, the difference is  $\sim 32 \text{ kJ mol}^{-1}$ . At the same time, the relative partial molar enthalpies and entropies vary with  $85.83 \text{ kJ mol}^{-1}$  and  $93 \text{ J mol}^{-1} \text{ K}^{-1}$ , respectively.

In the case of compounds in which iron is present, the influence of such small variations in concentration of strontium ions is diminished and variations of only  $1-10 \text{ kJ mol}^{-1}$  in  $\Delta\bar{G}_{O_2}$  values between the samples S1 and S2 are found. A similar comment can be made referring to the  $\log p_{O_2}$  values (Fig. 3), which are very close for the samples S1 and S2. These findings can be explained by the relative redox stability of the B<sup>3+</sup> ions. The Fe<sup>3+</sup> ions tends to bind the O<sup>2-</sup> ions more strongly than Mn<sup>3+</sup> which seems to decrease (at the same A-site composition) both the mobility and the concentration of the oxygen vacancies. This statement agrees with the model suggested by Steele and others (12,13) and also is confirmed by the observations of Teraoka et al. (14,15) in a study of the ionic conductivities and oxygen permeation in cobaltites doped by iron. Regarding the  $\Delta\bar{H}_{O_2}$  values (Fig. 4), they are comparatively higher in lanthanum strontium ferrite manganites than in lanthanum

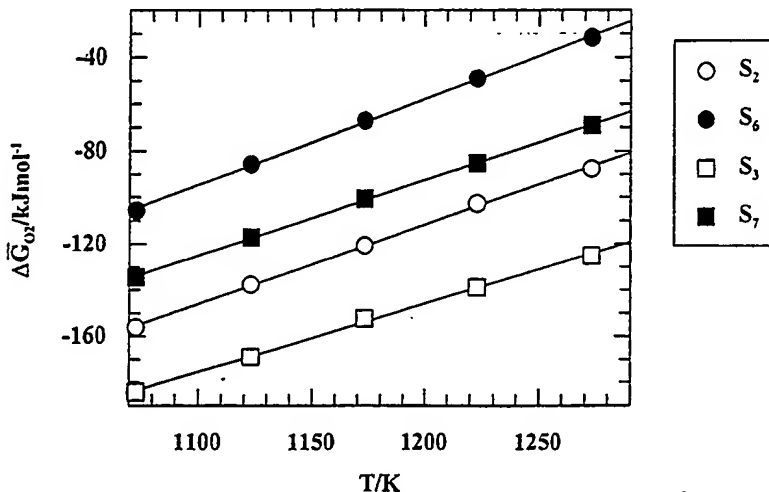


FIG. 6

The effect of overall A-site stoichiometry on the variation of  $\Delta\bar{G}_{O_2}$  with temperature in lanthanum strontium ferrite manganites.

strontium manganites with the same strontium content, suggesting that the predominant defects are different in the two groups of compounds. It is also interesting to note that the increase in A-site substitution from  $x = 0.25$  to  $x = 0.30$  affects oppositely the values of  $\Delta\bar{H}_{O_2}$  and  $\Delta\bar{S}_{O_2}$  for the samples S4, S5 (in absence of iron) and S1, S2 (with 20% iron), respectively (Figs. 4 and 5). The increase of these values in the first case can indicate that the oxygen vacancies distribute randomly on the oxygen sublattice, while the decrease of  $\Delta\bar{H}_{O_2}$  and  $\Delta\bar{S}_{O_2}$  in the iron-containing samples suggests the increase of the binding energy of oxygen and an increase of order in the oxygen sublattice of the perovskite-type structure, respectively.

The change of the thermodynamic data with the iron content in the group of lanthanum strontium ferrite manganites at the same strontium content ( $x = 0.3$ ), can be observed comparing the samples S3, S7 (with 70% iron) and S2, S6 (with 20% iron), respectively. The  $\Delta\bar{G}_{O_2}$  values obtained for S3 and S7 are  $\sim 28 \text{ kJ mol}^{-1}$  (at 1073 K) and  $\sim 37 \text{ kJ mol}^{-1}$  (at 1273 K) more negative compared with the values found for S2 and S6. The values of  $\Delta\bar{H}_{O_2}$  and  $\Delta\bar{S}_{O_2}$  increase correspondingly at a higher iron content with  $\sim 20 \text{ kJ mol}^{-1}$  and  $\sim 45 \text{ J mol}^{-1} \text{ K}^{-1}$ , respectively.

At a medium iron content (50% Fe), the higher values of  $\Delta\bar{H}_{O_2}$  and  $\Delta\bar{S}_{O_2}$  are found for the sample S9 with 0.5% Co. In this case, the  $\Delta\bar{H}_{O_2}$  and  $\Delta\bar{S}_{O_2}$  values increase with  $64 \text{ kJ mol}^{-1}$  and  $55 \text{ J mol}^{-1} \text{ K}^{-1}$ , respectively, compared with the values obtained for the sample S8 without cobalt.

**Effect of Overall A-Site Stoichiometry on the Thermodynamic Properties.** The effect of the reduction in the A-site stoichiometry from 1 to 0.95 on the thermodynamic properties can be observed in Figure 6, where the variations of  $\Delta\bar{G}_{O_2}$  with the temperature are presented comparatively for the samples S2, S3 and S6, S7, respectively.

As one can see, the reduction in the A-site stoichiometry is followed by a decrease of  $\Delta\bar{G}_{O_2}$  with  $\sim 50 \text{ kJ mol}^{-1}$  at 1073 K and  $\sim 55 \text{ kJ mol}^{-1}$  at 1273 K. Similarly, the  $\log p_{O_2}$  values decrease from  $-5.14$  to  $-7.60$  and from  $-6.55$  to  $-8.97$ , respectively, with the reduction of the stoichiometry (Fig. 3). However, the  $\Delta\bar{S}_{O_2}$  values increase with  $\sim 25 \text{ J mol}^{-1} \text{ K}^{-1}$ . The data are tentatively interpreted to indicate an increase of order in the oxygen sublattice with the change in the A-site stoichiometry.

In the future, new measurements on compounds with different A-site and B-site dopants concentrations will help determine the variation of thermodynamic properties over larger ranges of the compositional variables  $x$  and  $y$ .

#### ACKNOWLEDGMENTS

The authors are indebted to the Commission of the European Communities (Science, Research and Development) for financial support in the frame of the Contract JOU 2-CT 92-0063.

We wish to thank Risø National Laboratory for supplying the solid electrolyte and Haldor Topsøe A/S for preparing the samples used in this study. Many thanks are extended to Dr. M. Mogensen and Dr. N. Bonanos for helpful discussions.

## REFERENCES

1. H. Yokokawa, N. Sakai, T. Kawada and M. Dokiya, *Proceedings International Symp. on SOFC, Nagoya*, ed. H. Tagawa and O. Yamamoto, M. Dokiya, p. 118 (1989).
2. H. Yokokawa, N. Sakai, T. Kawada and M. Dokiya, *Proceedings Second International Symp. on SOFC, Athens*, ed. F. Gross, P. Zegers, S.C. Singhal and O. Yamamoto, p. 663 (1991).
3. H. Yokokawa, N. Sakai, T. Kawada and M. Dokiya, *Solid State Ionics* 52, 43 (1992).
4. J.H. Kuo, H.U. Anderson and D.M. Sparlin, *J. Solid State Chem.* 83, 52 (1989).
5. J. Mizusaki and H. Tagawa, *Solid State Ionics* 49, 111 (1991).
6. S. Tanasescu, N.D. Totir and D.I. Marchidan, submitted to *Electrochim. Acta*.
7. S. Tanasescu, N.D. Totir and D.I. Marchidan, *Mater. Res. Bull.* 32 (1997), in press.
8. P. Gordes and N. Christiansen, *Proceedings First European SOFC Forum*, Lucerne, ed. U. Bossel, Vol. 2, p. 567 (1994).
9. P. Gordes and N. Christiansen, Technical Reports of Haldor Topsøe A/S for the EC Project "New SOFC Materials and Technology" (1994-1995).
10. L.S. Darken and R.W. Gurry, *J. Am. Chem. Soc.* 67, 1398 (1945).
11. K.K. Kelley, U.S. Bur. Mines Bull. No. 584 (1960); K.K. Kelley and E.G. King, U.S. Bur. Mines Bull. No. 592 (1961).
12. B.C.H. Steele, *Proceedings of the 14th Risø International Symp. on Materials Science, Roskilde*, ed. F.W. Poulsen, J.J. Bentzen, T. Jacobsen, E. Skou and M.J.L. Østergaard, p. 423 (1993).
13. S. Carter, A. Selcuk, R.J. Chater, J. Kajda, J.A. Kilner and B.C.H. Steele, *Solid State Ionics* 53-56, 597 (1992).
14. Y. Teraoka, H.M. Zhang, K. Okamoto and N. Yamazoe, *Mater. Res. Bull.* 23, 51 (1988).
15. Y. Teraoka, H.M. Zhang, S. Furukawa and N. Yamazoe, *Chem. Lett.*, 1743 (1985).

**This Page Blank (uspto)**

## Phase Behavior of Lanthanum Strontium Manganites

Feng Zheng<sup>a</sup> and Larry R. Pederson<sup>b</sup>

<sup>a</sup>Department of Materials Science and Engineering, University of Washington, Seattle, Washington 98195-2120, USA

<sup>b</sup>Battelle Pacific Northwest National Laboratory, Materials and Chemical Sciences Department, Richland, Washington 99352, USA

The phase stability of Sr-doped  $\text{LaMnO}_3$  (LSM) perovskite in the La-Sr-Mn-O system was investigated as a function of Sr content and A/B cation ratio. The perovskite structure changed with both Sr content and A/B cation ratio. As the Sr content was increased to 0.2 mol, the perovskite structure adopted an orthorhombic distortion. This changed to a monoclinic or hexagonal structure for  $0.2 \leq \text{Sr} \leq 0.3$  mol. When the Sr content increased to 0.3 mol, the structure reverted to orthorhombic symmetry. Data from X-ray powder diffractometry, scanning electron microscopy, transmission electron microscopy, and energy-dispersive X-ray emission spectroscopy, showed that secondary phases in the La-Sr-Mn-O system were underdeveloped with respect to changes of the doped Sr content, A/B cation ratio, and thermal history. X-ray detectable minor phases present in the LSM material were  $\text{Mn}_3\text{O}_4$ ,  $(\text{La}, \text{Sr})\text{Mn}_2\text{O}_4$ ,  $\text{La}_2\text{O}_3$ ,  $\text{La}(\text{OH})_3$ ,  $(\text{La}, \text{Sr})_3\text{Mn}_2\text{O}_7$ , and  $(\text{La}, \text{Sr})_2\text{MnO}_4$ .

© 1999 The Electrochemical Society. S0013-4651(98)11-108-X. All rights reserved.

Manuscript submitted November 23, 1998; revised manuscript received March 15, 1999.

Lanthanum strontium manganites ( $\text{La}_{1-x}\text{Sr}_x\text{MnO}_{3-\delta}$ —LSM) are p-type electrically conducting oxides of  $\text{ABO}_3$ -type perovskite structure. Because of their desirable properties, they have been chosen as the cathode material in solid oxide fuel cells (SOFCs).<sup>1,2</sup> The phase behavior of LSM is vital to our understanding of SOFC operation. This is especially true when we consider fuel cell stability and long-term performance. We need to monitor the possible reactions that occur between the LSM and adjacent fuel cell components. There have been numerous studies conducted to investigate the material properties of LSM, in terms of crystal structure,<sup>3-10</sup> defect chemistry,<sup>11-13</sup> thermodynamics,<sup>11,12,14-24</sup> phase diagrams,<sup>14-17,25</sup> electrical conductivity,<sup>12,26-28</sup> thermal expansion behavior,<sup>1,28</sup> processing methods,<sup>29-32</sup> and sintering.<sup>33,34</sup>

Hashimoto *et al.* reported that the structure of  $\text{La}_{0.9}\text{Sr}_{0.1}\text{MnO}_3$  is orthorhombic with lattice constants  $a = 0.55464$ ,  $b = 0.55919$ ,  $c = 0.77408$  nm (space group 17,  $P222_1$ ).<sup>3</sup> When the Sr content increased to 0.2 mol ( $\text{La}_{0.8}\text{Sr}_{0.2}\text{MnO}_3$ ), the structure changed to a monoclinic symmetry with  $a = 0.5484$ ,  $b = 0.55349$ ,  $c = 0.77916$  nm and  $\beta = 90.746^\circ$  (space group 13:b1,  $P2/c$ ). The monoclinic structure was stable with increased Sr doping up to 0.4 mol. The unit cell volume decreased with increasing Sr content.

Hammouche *et al.* characterized  $\text{La}_{1-x}\text{Sr}_x\text{MnO}_3$  ( $0 < x < 0.5$ ) by X-ray diffraction. They indexed all of their X-ray patterns as hexagonal-rhombohedral distorted perovskites<sup>4</sup> and found that the decrease in  $a_b$  and  $\alpha_h$  with increasing Sr content was due to the creation of  $\text{Mn}^{4+}$ . They claimed that their  $c_h$  values were independent of the Sr doping content.

Millini *et al.* studied X-ray data for  $\text{La}_{1-x}\text{Sr}_x\text{MnO}_3$  ( $0.1 < x < 0.5$ ) by a full-profile fitting method.<sup>5</sup> They found that  $\text{La}_{1-x}\text{Sr}_x\text{MnO}_3$  adopted a hexagonal-rhombohedral distortion, derived from the ideal cubic symmetry through the rotation of the  $[\text{MnO}_6]$  octahedron. The extent of the distortion depended on the doping level. The unit cell volume was calculated as  $V = 355.99 - 21.188x$  ( $\text{\AA}^3$ ), where  $x$  represents the doped Sr mole content.

Berg *et al.* reviewed structural data for LSM<sup>3-7</sup> and reported that  $\text{La}_{0.8}\text{Sr}_{0.2}\text{MnO}_3$  can be indexed either as rhombohedral with  $a = 0.55188(8)$  and  $c = 1.3359(8)$  nm (space group 167:H,  $R\bar{3}c$ ) or monoclinic with  $a = 0.548$ ,  $b = 0.553$ ,  $c = 0.779$  nm, and  $\beta = 90.7^\circ$  (space group 13:b1,  $P2/c$ ).<sup>8</sup>

Zhang and coworkers found that the structure of LSM changes with Sr content.<sup>9</sup> They observed three different perovskite-type phases at room temperature: orthorhombic for  $0 < x < 0.15$ , hexagonal for  $0.15 < x < 0.45$ , and cubic for  $x > 0.45$ . The unit cell volume of the LSM decreased with increasing Sr concentration. They also reported that the electrical conductivity showed a peak value of 200 S/cm at  $x = 0.5$  for a temperature of 1273 K in air.

Benabad *et al.* studied the structure of  $\text{SrLaMnO}_4$  [ $a = 0.3804(5)$ ,  $c = 1.310(1)$  nm] and found that its solid solution  $\text{Sr}_{1+x}\text{La}_{1-x}\text{MnO}_4$  has a  $\text{K}_2\text{NiF}_4$ -type structure.<sup>10</sup> The  $c/a$  ratio of the unit cell was related to the electronic configuration of the  $\text{Mn}^{3+}$  ions. Thermodynamic properties of the  $\text{SrLaMnO}_4$  phase and two Ruddelesden-Popper phases  $\text{LaSr}_2\text{Mn}_2\text{O}_7$  and  $\text{La}_2\text{SrMn}_2\text{O}_7$  were reported by Yokokawa *et al.*<sup>16</sup>

To date, most work was focused on one or two LSM compositions, with a few exceptions<sup>3-5,9</sup> that covered narrow composition regions. We are not aware of any work on the structural changes affected by varying A/B cation ratio, although it is important because A-site deficient LSM perovskites are candidates for SOFC cathode materials.<sup>1,2,33</sup>

The objective of this work was to study the phase behavior of the LSM perovskites with regard to stability and phase development in the La-Sr-Mn-O system. The Sr content was varied from 0.1 to 0.7 mol and the A/B cation ratio was varied from 0.8 to 1.2.

### Experimental

To understand the phase behavior of the La-Sr-Mn-O system, stoichiometric (A/B = 1) and off-stoichiometric (A/B ≠ 1) powders were made by the glycine/nitrate (GNP) method.<sup>29,30</sup> The ash produced by GNP was amorphous. Calcination at 900°C for 1 h removed residual organic materials. Calcined powders were uniaxially pressed into green disks of the desired diameters at 55 MPa. The disks were then pressed isostatically at 135 MPa prior to sintering in a furnace at 1000, 1200, 1250, 1350, 1400, or 1450°C for 1, 2, or 4 h. Phase development was characterized by X-ray diffractometry, and data were collected on a Philips 3100 X-ray generator, using  $\text{Cu K}\alpha_1$  with an operating power of 40 kV, 45 mA. Indexing for each phase was accomplished using Jade + Ver. 2.1 (Materials Data, Inc., MDI, Livermore, CA).

After sintering bulk materials were crushed and ground manually with an agate mortar and pestle. The particles were sieved to 325 mesh (<45  $\mu\text{m}$ ). Specimens were mounted in a front-loading, shallow-cavity holder fabricated from low-background, off-axis, single-crystal quartz provided by Gem Dugout, State College, PA. Data collection was performed at room temperature ( $26 \pm 2^\circ\text{C}$ ). The instrumental conditions and diffraction scan parameters used in this study are listed in Table I.

The X-ray diffraction intensities were determined from observed peak heights after background subtraction. In addition, the reported experimental intensities were corrected to the fixed-slit approximation using the  $1/\sin\theta$  function resident in the X-ray powder diffraction pattern processing code JADE 2.1.

The  $2\theta$  error-corrected experimental d-spacings were indexed using the Louer algorithm-based code included in Micro-INDEX,

Ver. 2.0. The  $hkl$ -space search was limited to maximum lattice parameter of  $a = 1.0$ ,  $b = 1.0$ , and  $c = 2.0$  nm with input unit cell volume of  $4000 \text{ \AA}^3$ . Lattice parameters that resulted from the indexing and the  $2\theta$  error-corrected experimental d-spacings were input to the Appleman-Evans algorithm-based, autoindexing cell refinement program resident in Micro-CELLREF, Ver. 2.0. The refinement code was allowed to execute three least-squares cycles to reach convergence with a  $\Delta 2\theta$ -error limit of  $0.03^\circ$  ( $\Delta = |\text{obs.} - \text{calc.}|$ ).

An environmental SEM (Electro Scan, 1990) operated at  $20 \text{ keV}$  was used to study the microstructure of the material. TEM was used (JOEL 1200 EX electron microscope operated at  $120 \text{ keV}$  and equipped with an EDS) to identify each phase.

### Results

**Sintering behavior.**—The sintering behavior changed with respect to the Sr content, A/B cation ratio, and sintering temperature. Sintering shrinkage decreased with increased Sr content (maximum shrinkage occurred at  $\text{Sr} = 0 \text{ mol}$ ). The sintered density was inversely proportional to the A/B cation ratio. For  $A/B > 1$ , sintering cracks at the surfaces of sample disks were often observed with Sr content greater than  $0.3 \text{ mol}$ .

Because of their use as SOFC cathode materials, A-site deficient compositions have been recognized and suggested for the LSM material. Stevenson *et al.* found that the mechanism of sintering in LSM materials was strongly dependent on Mn vacancies in the B site of the perovskite.<sup>33</sup> If  $A/B < 1$ , more Mn vacancies can be created, thereby improving the sintering of the LSM perovskites. Our current study supports this understanding. The trend is clear, with an increase in A/B cation ratio and/or Sr content, more and larger fired cracks appeared in the samples.

**XRDP patterns.**—Undoped lanthanum manganite ( $\text{LaMnO}_3$ ) exhibited an orthorhombic distortion under our test conditions. The calculated lattice parameters are  $a = 0.553861(5)$ ,  $b = 0.567805(5)$ , and  $c = 0.771987(8)$  nm. The unit cell volume is  $242.778(3) \text{ \AA}^3$ . These parameters are comparable to the database provided inside Jade+ *i.e.*, Powder Diffraction Files (cf., PDF 33-0713). For LSM, the situation becomes more complicated. Beside the variations in lattice constants and changes in symmetry for the primary perovskites, secondary phase(s) were also developed.

For instance, LSM-16 and LSM-24 (here 16 and 24 represent the doped Sr content in mol %) sintered at  $1400^\circ\text{C}$  for 1 h were hexagonal perovskites for A/B cation ratio varying from 0.95 to 1.05. The remaining materials (LSM-10 to LSM-70) sintered at  $1450^\circ\text{C}$  for 2 h adopted a monoclinic, orthorhombic, or hexagonal structure, with A/B ratio changed from 0.9 to 1.1. The changes in the A/B cation ratio had a significant influence on minor-phase evolution. For example, when  $A/B > 1$ , the secondary phase,  $\text{La}_2\text{O}_3$ , was formed with the LSM per-

ovskite phase. The main influence of temperature was in the lattice constant variations and structure change, whereas its effect on phase equilibrium was minor. It is believed that the Sr doping increased the activity of the perovskite, and consequently promoted the formation of secondary phases.<sup>35</sup> At a higher doping level,  $(\text{La}, \text{Sr})_2\text{MnO}_4$  began to form when the Sr content reached  $0.3 \text{ mol}$ . Furthermore,  $\text{SrCO}_3$ , came into play when  $0.4 \text{ mol}$  or higher Sr was present. However, this carbonate decomposed upon prolonged heating. To summarize, there were five minor phases within the XRPD detection limit, apart from the primary LSM perovskite. The lattice constants of the LSM perovskite phase are listed in Table II. In addition, the lattice constants of two tetragonal-type minor phases,  $(\text{La}, \text{Sr})_3\text{Mn}_2\text{O}_7$  and  $(\text{La}, \text{Sr})_2\text{MnO}_4$  are listed in Tables III and IV, respectively. These phases are new to our knowledge and deserve special attention. Because there is no entry for  $(\text{La}, \text{Sr})_2\text{MnO}_4$  in Jade, (*i.e.*, no PDF card) we made our own reference pattern by the GNP method with La and Sr at an equal mole ratio. Calcined at  $900^\circ\text{C}$  for 16 h and sintered at  $1450^\circ\text{C}$  for 24 h, the lattice constants of this  $(\text{La}, \text{Sr})_2\text{MnO}_4$  pattern were indexed as  $a = 0.384653(4)$ ,  $c = 1.25832(1) \text{ nm}$  with unit cell volume  $V = 186.179(4) \text{ \AA}^3$ .

We have extended our study to the phase behavior of off-stoichiometric LSM materials as the A-site deficient LSMs are preferred for SOFC cathodes. We held the La content fixed at  $0.8 \text{ mol}$  and allowed the Sr content to vary from zero to  $0.4 \text{ mol}$ . With increased Sr content, the perovskite adopted a hexagonal structure for  $\text{Sr} < 0.3 \text{ mol}$ . For  $\text{Sr} > 0.3 \text{ mol}$ , the structure changed to an orthorhombic symmetry. Phase development was similar to the stoichiometric LSM with one exception, the  $(\text{La}, \text{Sr})_3\text{Mn}_2\text{O}_7$  phase was not detectable. The nature of the tetragonal  $(\text{La}, \text{Sr})_3\text{Mn}_2\text{O}_7$  is a high-temperature Ruddlesden-Popper phase, which decomposes at lower temperatures.<sup>16</sup> Our off-stoichiometric LSM materials were sintered at  $1200^\circ\text{C}$  (for 2 h), which may be below the stable temperature region of  $(\text{La}, \text{Sr})_3\text{Mn}_2\text{O}_7$ .

The minor phase development in the LSM materials can be demonstrated by comparing multiple X-ray spectra as a function of Sr content ( $x$ , in mole fraction) at a fixed A/B ratio. For instance, at  $A/B = 1.10$ , the results are shown in Fig. 1 with  $x = 0.1$  to  $0.7 \text{ mol}$ . From the plot we can see clearly that there are at least three minor phases,  $\text{La}_2\text{O}_3$ ,  $(\text{La}, \text{Sr})_3\text{Mn}_2\text{O}_7$ , and  $(\text{La}, \text{Sr})_2\text{MnO}_4$ , being developed. The changes in secondary phases, with respect to the variations in the A/B cation ratio and Sr content for  $\text{La}_{0.8}\text{Sr}_x\text{MnO}_3$ , sintered at  $1200^\circ\text{C}$  for 2 h, is shown in Fig. 2. The lattice constants are listed in Table V. Detailed structure analysis for minor phases  $(\text{La}, \text{Sr})_3\text{Mn}_2\text{O}_4$  and  $(\text{La}, \text{Sr})_2\text{MnO}_4$  in the  $\text{La}_{0.8}\text{Sr}_x\text{MnO}_3$  systems was impossible due to the limited data collected.

SEM images showed that the samples were porous and fully homogenous with very fine grains ( $< 1 \mu\text{m}$ ). No noticeable morphological changes were observed due to the heat-treatment above  $1000^\circ\text{C}$ . TEM images, diffraction patterns, and corresponding EDS spectra associated with the primary perovskite phase and the minor phases  $\text{Mn}_3\text{O}_4$ ,  $(\text{La}, \text{Sr})_3\text{Mn}_2\text{O}_4$ ,  $\text{La}_2\text{O}_3$ ,  $\text{La}(\text{OH})_3$ , and  $(\text{La}, \text{Sr})_2\text{MnO}_4$  were collected and analyzed.

Using TEM, the primary LSM perovskite was detected throughout the samples. EDS spectra recorded for different Sr contents confirmed the perovskite compositions of  $(\text{La}_{1-x}\text{Sr}_x)\text{MnO}_3$ . For samples with  $A/B < 1$ , EDS identified two minor phases  $\text{Mn}_3\text{O}_4$  and  $(\text{La}, \text{Sr})_3\text{Mn}_2\text{O}_4$ . For  $A/B > 1$ , the minor phases present are  $\text{La}_2\text{O}_3$ ,  $(\text{La}, \text{Sr})_2\text{MnO}_4$  and  $(\text{La}, \text{Sr})_3\text{Mn}_2\text{O}_7$ .

### Discussion

The perovskite-type phase of composition  $(\text{La}, \text{Sr})\text{MnO}_3$  dominates the material properties of the cathode. The ideal perovskite structure is cubic, however, atomic distortions are often observed.<sup>3-5,9</sup> The primary perovskite phase could possess either an orthorhombic, monoclinic, or hexagonal structure, depending on sample composition and thermal history.

**Primary perovskite phase LSM.**—For the stoichiometric ( $A/B = 1$ ) compositions of LSM-16 and LSM-24 sintered at  $1400^\circ\text{C}$  for 1 h, the observed structure of the primary phase was hexagonal perovskite.

Table I. X-ray instrumental conditions and diffraction scan parameters.

Instrument conditions		
Goniometer	Philips type PN3550/00X, vertical	
X-ray source	Fixed anode LFF Cu tube	
Power	40 kV, 45 mA (1800 W)	
Radiation, $\lambda$	$\text{Cu K}\alpha_1$ , $1.54060 \text{ \AA}$	
Monochromator	Graphite	
Counter	Scintillation	
Soller slits	Employed on incident beam side only	
Divergence slit	Variable	
Receiving slit	Fixed, 0.2 mm	
Diffraction scan parameters		
2 $\theta$ Range	Scan rate	Comments
5-75°	0.04°/2 s	No internal standard used
5-75°	0.02°/10 s	No peaks observed below 15°

Table II. The Lattice constants of the primary LSM perovskite phase in the La-Sr-Mn-O system.

A/B cation ratio in the La-Sr-Mn-O system ( $x$ = mole of Sr)								
$x$	0.900	0.925	0.950	0.980	1.000	1.020	1.050	1.100
0.10	$a = 5.4836(7)$ $b = 5.5233(8)$ $c = 7.794(2)$ $\beta = 90.89(2)$ $V = 236.04(5)$	$a = 5.48894(9)$ $b = 5.5422(1)$ $c = 7.7727(1)$ $\beta = 90.640(1)$ $V = 236.435(5)$	$a = 5.512(1)$ $b = 5.5247(8)$ $c = 7.787(1)$ $\beta = 90.640(1)$ $V = 237.14(5)$	$a = 5.5152(2)$ $b = 5.5312(3)$ $c = 7.7974(6)$ $\beta = 90.640(1)$ $V = 237.86(2)$	$a = 5.515(1)$ $b = 5.535(1)$ $c = 7.795(2)$ $\beta = 90.640(1)$ $V = 237.97(7)$	$a = 5.5406(4)$ $b = 5.5196(3)$ $c = 7.7896(6)$ $\beta = 90.640(1)$ $V = 238.22(2)$	$a = 5.5164(2)$ $b = 5.5220(2)$ $c = 7.8020(4)$ $\beta = 90.640(1)$ $V = 237.66(1)$	$a = 5.5348(1)$ $b = 5.5204(1)$ $c = 7.8030(2)$ $\beta = 90.640(1)$ $V = 238.416(6)$
0.16 <sup>a</sup>	Not studied	Not studied	$a = 5.5298(3)$ $b = 5.5298$ $c = 13.373(1)$ $V = 354.14(4)$	$a = 5.5251(3)$ $b = 5.5251$ $c = 13.362(1)$ $V = 353.25(4)$	$a = 5.5233(3)$ $b = 5.5233$ $c = 13.3630(9)$ $V = 353.04(4)$	$a = 5.5284(3)$ $b = 5.5284$ $c = 13.365(1)$ $V = 353.75(4)$	$a = 5.5278(3)$ $b = 5.5278$ $c = 13.366(1)$ $V = 353.70(4)$	Not studied
0.20	$a = 5.4806(4)$ $b = 5.5261(4)$ $c = 7.7538(9)$ $\beta = 90.633(9)$ $V = 234.82(3)$	$a = 5.5205(2)$ $b = 5.5205$ $c = 13.3584(5)$ $\beta = 90.78(2)$ $V = 352.57(2)$	$a = 5.4786(8)$ $b = 5.514(2)$ $c = 7.763(2)$ $\beta = 90.78(2)$ $V = 234.47(7)$	$a = 5.52175(7)$ $b = 5.52175$ $c = 13.3724(2)$ $\beta = 90.78(2)$ $V = 353.10(1)$	$a = 5.5041(3)$ $b = 5.5041$ $c = 13.330(1)$ $\beta = 90.78(2)$ $V = 349.72(4)$	$a = 5.51444(8)$ $b = 5.51444$ $c = 13.3594(3)$ $\beta = 90.78(2)$ $V = 351.82(1)$	$a = 5.523(1)$ $b = 5.523$ $c = 13.367(3)$ $\beta = 90.78(2)$ $V = 353.1(1)$	$a = 5.5212(2)$ $b = 5.5212(2)$ $c = 13.3755(7)$ $\beta = 90.78(2)$ $V = 353.11(2)$
0.24 <sup>a</sup>	Not studied	Not studied	$a = 5.5156(5)$ $b = 5.5156$ $c = 13.368(1)$ $V = 352.18(6)$	$a = 5.5134(7)$ $b = 5.5134$ $c = 13.370(2)$ $V = 351.96(8)$	$a = 5.5106(4)$ $b = 5.5106$ $c = 13.366(1)$ $V = 351.49(5)$	$a = 5.5083(2)$ $b = 5.5083$ $c = 13.3580(6)$ $V = 351.00(2)$	$a = 5.5153(5)$ $b = 5.5153$ $c = 13.366(2)$ $V = 352.10(6)$	Not studied
0.30	$a = 5.4703(2)$ $b = 5.5020(1)$ $c = 7.7431(3)$ $\beta = 90.372(3)$ $V = 233.04(1)$	$a = 5.4993(2)$ $b = 5.4993$ $c = 13.3667(7)$ $\beta = 90.47(2)$ $V = 350.08(2)$	$a = 5.4722(8)$ $b = 5.5004(8)$ $c = 7.739(1)$ $\beta = 90.47(2)$ $V = 232.94(6)$	$a = 5.4499(2)$ $b = 5.4955(2)$ $c = 7.7551(3)$ $\beta = 90.47(2)$ $V = 232.26(1)$	$a = 5.4683(2)$ $b = 5.5041(2)$ $c = 7.7587(4)$ $\beta = 90.423(5)$ $V = 233.51(1)$	$a = 5.4345(3)$ $b = 5.4962(2)$ $c = 7.7508(3)$ $\beta = 90.423(5)$ $V = 231.51(1)$	$a = 5.4400(9)$ $b = 5.5014(5)$ $c = 7.7530(8)$ $\beta = 90.423(5)$ $V = 232.03(4)$	$a = 5.4378(4)$ $b = 5.5018(3)$ $c = 7.7572(4)$ $\beta = 90.423(5)$ $V = 232.08(2)$
0.40	$a = 5.4593(2)$ $b = 5.4796(2)$ $c = 7.7143(2)$ $V = 230.77(1)$	$a = 5.4647(7)$ $b = 5.4677(6)$ $c = 7.728(3)$ $V = 230.90(8)$	$a = 5.45280(6)$ $b = 5.48252(6)$ $c = 7.7233(3)$ $V = 230.890(7)$	$a = 5.4674(2)$ $b = 5.4713(4)$ $c = 7.7483(4)$ $V = 231.78(1)$	$a = 5.455(1)$ $b = 5.475(1)$ $c = 7.718(2)$ $V = 230.49(5)$	$a = 5.46819(6)$ $b = 5.4677(1)$ $c = 7.74417(9)$ $V = 231.539(5)$	$a = 5.4409(2)$ $b = 5.4902(1)$ $c = 7.7438(3)$ $V = 231.317(9)$	$a = 5.4408(3)$ $b = 5.4890(2)$ $c = 7.7505(4)$ $V = 231.46(2)$
0.50	$a = 5.4251(8)$ $b = 5.4613(8)$ $c = 7.723(2)$ $V = 228.81(5)$	$a = 5.4456(6)$ $b = 5.4442(2)$ $c = 7.744(1)$ $V = 229.59(7)$	$a = 5.467(2)$ $b = 5.4553(4)$ $c = 7.7216(5)$ $V = 230.30(6)$	$a = 5.4583(8)$ $b = 5.4621(3)$ $c = 7.7196(4)$ $V = 230.15(3)$	$a = 5.4547(6)$ $b = 5.4658(6)$ $c = 7.716(1)$ $V = 230.05(5)$	$a = 5.4547(9)$ $b = 5.4636(7)$ $c = 7.7339(9)$ $V = 230.48(3)$	$a = 5.4567(2)$ $b = 5.4677(6)$ $c = 7.7386(6)$ $V = 230.88(2)$	$a = 5.4590(2)$ $b = 5.4627(1)$ $c = 7.7341(2)$ $V = 230.63(1)$
0.60	$a = 5.4463(1)$ $b = 5.4381(2)$ $c = 7.6868(2)$ $V = 227.666(8)$	$a = 5.4431(2)$ $b = 5.4720(4)$ $c = 7.6815(3)$ $V = 228.79(2)$	$a = 5.4382(1)$ $b = 5.4707(1)$ $c = 7.6818(2)$ $V = 228.539(4)$	$a = 5.43961(7)$ $b = 5.44656(6)$ $c = 7.7017(1)$ $V = 228.180(4)$	$a = 5.4366(1)$ $b = 5.4778(6)$ $c = 7.6713(2)$ $V = 229.29(2)$	$a = 5.43647(8)$ $b = 5.44897(7)$ $c = 7.7016(2)$ $V = 228.145(6)$	$a = 5.4383(4)$ $b = 5.4537(5)$ $c = 7.6978(5)$ $V = 228.30(2)$	$a = 5.43780(5)$ $b = 5.45822(6)$ $c = 7.7166(1)$ $V = 229.036(4)$
0.70	$a = 5.4189(2)$ $b = 5.4213(1)$ $c = 7.6631(4)$ $V = 225.12(1)$	$a = 5.42033(4)$ $b = 5.42396(5)$ $c = 7.6727(1)$ $V = 225.575(3)$	$a = 5.428(1)$ $b = 5.4278(6)$ $c = 7.6710(5)$ $V = 226.00(5)$	$a = 5.4201(2)$ $b = 5.4274(3)$ $c = 7.6763(3)$ $V = 225.81(1)$	$a = 5.418(1)$ $b = 5.4276(4)$ $c = 7.6712(6)$ $V = 225.59(4)$	$a = 5.4248(2)$ $b = 5.4417(3)$ $c = 7.6879(5)$ $V = 226.95(1)$	$a = 5.42438(7)$ $b = 5.44092(6)$ $c = 7.68792(6)$ $V = 226.898(3)$	$a = 5.426(1)$ $b = 5.443(1)$ $c = 7.681(2)$ $V = 226.81(8)$

<sup>a</sup> LSM-16 and LSM-24 were sintered at 1400°C for 1 h (the remaining materials were sintered at 1450°C for 2 h).

The remaining LSM materials (LSM-10 to LSM-70), sintered at 1450°C for 2 h, adopted a monoclinic, orthorhombic, or hexagonal structure. The lattice constants and the cell volume of these perovskite phases decreased consistently with increased Sr doping. Considering the difference in sample preparation methods, level of impurities, and thermal history, our results are consistent with data presented in the literature.<sup>3-9</sup> In the present study, for instance, the changes in the lattice cell volume for the  $\text{La}_{1-x}\text{Sr}_x\text{MnO}_3$  ( $0.1 < x < 0.7$ ) perovskites are  $V = 357.51 - 25.884x$  (Å<sup>3</sup>) (see Table II, VII, and Fig. 3 for more details). This relationship is similar to that reported by Millini *et al.*,<sup>5</sup> where they found  $V = 355.99 - 21.188x$  (Å<sup>3</sup>) ( $0.1 < x < 0.5$ ) for their LSM perovskites.

Because the LSM perovskites possess different lattice structures, the pseudocubic method that converts noncubic structures into a cubic structure was used to provide a basis for comparison. Figure 3

shows such a pseudo-cubic lattice ( $a_c$ ) changes with the Sr content and the A/B cation ratio for the LSM materials.

Linear relationships between the pseudo-cubic lattice parameter  $a_c$  vs. Sr content for fixed A/B cation ratios were observed. The pseudo-cubic lattice constant  $a_c$  decreased linearly as the Sr content increased. Table VI lists the relationships found by least-square regression. The lower  $R^2$  values for the stoichiometric LSM indicate that the secondary peaks merged and overlapped into the primary phase peaks. For the off-stoichiometric samples, secondary phases were sufficiently developed to allow us to exclude their peaks from the lattice parameter analysis of the primary perovskite phase. Consequently, better lattice parameters could be indexed with higher  $R^2$  values. The influence of the A/B cation ratio on the changes in the lattice constants and cell volume of the perovskite phase was minor, compared to the effect of the Sr content. When varying the A/B ratio,

Table III. Lattice constants of the tetragonal phase  $(La, Sr)_3Mn_2O_7$ <sup>a</sup> in the La-Sr-Mn-O system.

A/B cation ratio in the La-Sr-Mn-O system ( $x$ = mole of Sr)								
$x$	0.900	0.925	0.950	0.980	1.000	1.020	1.050	1.100
0.100	—	—	—	—	—	—	—	—
0.200	—	—	—	—	—	—	—	—
0.300	—	—	—	?	—	?	?	?
0.400			$a = 3.87008(9)$	$a = 3.87485(6)$		$a = 3.86771(8)$	$a = 3.8699(1)$	$a = 3.8714(3)$
			$c = 20.0322(6)$	$c = 20.0523(3)$	—	$c = 20.1135(3)$	$c = 20.1309(4)$	$c = 20.171(1)$
			$V = 300.03(1)$	$V = 301.074(8)$		$V = 300.88(1)$	$V = 301.48(2)$	$V = 302.32(3)$
0.500		$a = 3.8549(2)$	$a = 3.87008(9)$	$a = 3.86161(7)$		$a = 3.875(2)$	$a = 3.875(1)$	$a = 3.87215(8)$
		$c = 19.966(1)$	$c = 20.0322(6)$	$c = 19.9947(4)$	—	$c = 19.988(9)$	$c = 19.994(6)$	$c = 19.9731(5)$
		$V = 296.71(2)$	$V = 300.03(1)$	$V = 298.161(9)$		$V = 300.1(3)$	$V = 300.2(1)$	$V = 299.47(1)$
0.600		$a = 3.85209(5)$	$a = 3.87008(9)$	$a = 3.8611(3)$		$a = 3.8570(3)$	$a = 3.8467(2)$	$a = 3.8610(4)$
		$c = 19.8723(3)$	$c = 20.0322(6)$	$c = 19.926(1)$	?	$c = 19.982(1)$	$c = 19.934(1)$	$c = 19.843(3)$
		$V = 294.877(6)$	$V = 300.03(1)$	$V = 297.06(3)$		$V = 297.26(4)$	$V = 294.95(2)$	$V = 295.81(6)$
0.700	$a \sim 3.8+$	$a = 3.85664(6)$	$a = 3.87008(9)$	$a = 3.85917(5)$		$a = 3.85354(7)$	$a = 3.8464(3)$	$a = 3.837(4)$
	$c \sim 20$	$c = 19.8205(5)$	$c = 20.0322(6)$	$c = 19.8999(2)$	?	$c = 19.9869(3)$	$c = 19.970(1)$	$c = 19.96(2)$
		$V \sim 300$	$V = 294.805(7)$	$V = 300.03(1)$		$V = 296.373(6)$	$V = 296.801(9)$	$V = 295.45(3)$
								$V = 293.9(5)$

<sup>a</sup> If the minor phase is not detectable by XRPD then a dash is placed for that material. A question mark shows that the phase is detected but without enough peaks available for possibly indexing.

extra vacancies were introduced into cation sites (either in the A or B site) that led to the creation of more free volume in the lattice structures. The perovskite could then undergo a change in size without disturbing symmetry.

Hexagonal and orthorhombic perovskite structures were observed in off-stoichiometric  $La_{0.8}Sr_xMnO_3$ . Their pseudo-cubic constants ( $a_c$ ) were computed and are listed in Table VII. Further analysis showed that the correlation between  $a_c$  and doped Sr content in  $La_{0.8}Sr_xMnO_3$  was relatively poor, compared to those found in  $La_{1-x}Sr_xMnO_3$  (see Fig. 3). The difference can be explained by the presence of more vacancies in  $La_{0.8}Sr_xMnO_3$  than in  $La_{1-x}Sr_xMnO_3$  for the same Sr content. The impact of the Sr doping on the lattice structure was therefore weaker in  $La_{0.8}Sr_xMnO_3$ . Note that from Fig. 3, due to the cre-

ation of  $Mn^{4+}$  and oxygen vacancies,<sup>4,38</sup> the pseudo-cubic constants  $a_c$  decreases with Sr content ( $Mn'_{Mn} = Sr'_{La}$  or  $V_O'' = 1/2 Sr'_{La}$ ). In addition, the pseudo-cubic constants  $a_c$  increases with A/B ratio (where the proportionality of  $Mn^{4+}$  and  $V_O''$  decreases with A/B ratio).<sup>38</sup>

**Minor phases.**—Theoretically, any off-stoichiometry (A/B ≠ 1) will result in the formation of secondary phase(s) when the solid solubility in the primary phase is small, as in most ceramic materials. Fortunately, pure  $LaMnO_3$  has a large solubility range.<sup>25</sup> One can obtain a single-phase region with the A/B cation ratio varying from ~0.92 to ~1.2. Our study confirmed the Sr solubility in  $LaMnO_3$  reported by Roosmalen *et al.*,<sup>25</sup> however, minor phases formed and increased in concentration as the A/B cation ratio deviated from

Table IV. Lattice constants of the tetragonal phase  $(La, Sr)_2MnO_4$ <sup>a</sup> in the La-Sr-Mn-O system.

A/B cation ratio in the La-Sr-Mn-O system ( $x$ = mole of Sr)								
$x$	0.900	0.925	0.950	0.980	1.000	1.020	1.050	1.100
0.100	—	—	—	—	—	—	—	—
0.200	—	—	—	—	—	—	—	—
0.300	—	—	—	—	—	—	—	—
0.400								$a = 3.86060(8)$
								$c = 12.4994(2)$
								$V = 186.294(6)$
0.500		$a = 3.8344(2)$				$a = 3.8562(8)$		$a = 3.85629(5)$
		$c = 12.4099(9)$	?	—	—	$c = 12.412(2)$	?	$c = 12.4150(1)$
		$V = 182.46(2)$				$V = 184.57(7)$		$V = 184.624(4)$
0.600	$a = 3.83092(5)$	$a = 3.8351(1)$		$a = 3.84795(6)$		$a = 3.84964(4)$	$a = 3.84647(6)$	$a = 3.84367(6)$
	$c = 12.3999(1)$	$c = 12.4018(3)$	?	$c = 12.3975(2)$	?	$c = 12.3972(1)$	$c = 12.3920(2)$	$c = 12.3828(1)$
	$V = 181.968(4)$	$V = 182.405(9)$		$V = 183.567(4)$		$V = 183.723(4)$	$V = 183.344(5)$	$V = 182.941(5)$
0.700	$a = 3.83207(7)$	$a = 3.83207(7)$		$a = 3.83212(9)$		$a = 3.84106$	$a = 3.83529(8)$	$a = 3.829(3)$
	$c = 12.4207(2)$	$c = 12.4207(2)$	?	$c = 12.4260(3)$	?	$c = 12.4168(2)$	$c = 12.4251(2)$	$c = 12.408(8)$
	$V = 182.394(6)$	$V = 182.394(6)$		$V = 182.477(7)$		$V = 183.195(4)$	$V = 182.766(6)$	$V = 181.9(2)$

<sup>a</sup> If the minor phase is not detectable by XRPD then a dash is placed for that material. A question mark shows that the phase is detected but without enough peaks available for possibly indexing.

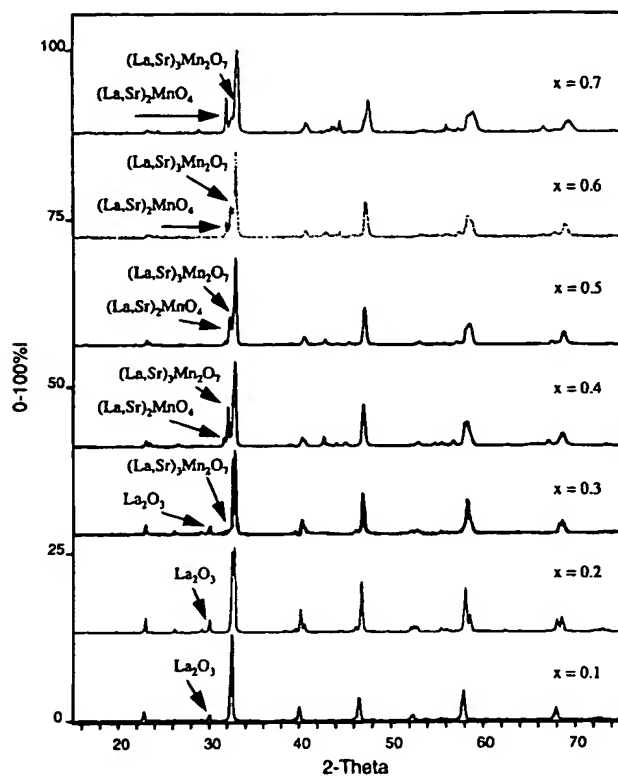


Figure 1. XRPD patterns of LSM with various Sr doping content at  $A/B = 1.10$ .

unity. In the case of  $A/B < 1$ , the minor phases observed were  $Mn_3O_4$ ,  $(La, Sr)Mn_2O_4$  (low-temperature tetragonal phase),  $(La, Sr)_3Mn_2O_7$  (Ruddlesden-Popper phase), and  $(La, Sr)_2MnO_4$  (tetragonal phase). When  $A/B = 1$ , secondary phases  $La_2O_3$  and  $(La, Sr)_3Mn_2O_7$  were observed [it is possible that  $(La, Sr)_2MnO_4$  could be present, however, it was not observed]. For  $A/B > 1$ ,  $La_2O_3$ ,  $La(OH)_3$ ,  $(La, Sr)_3Mn_2O_7$ , and  $(La, Sr)_2MnO_4$  were found.

For  $A/B < 1$ , we would expect to see  $Mn_3O_4$ ,<sup>25</sup> which may actually benefit SOFC operation by enhancing the electrocatalytic activity for oxygen reduction. All other minor phases observed adopted a tetragonal structure. Of great interest among these is  $(La, Sr)Mn_2O_4$ , which is present at low temperatures (observed at 1200°C but not at 1450°C). This is consistent with an earlier study conducted by Sieter

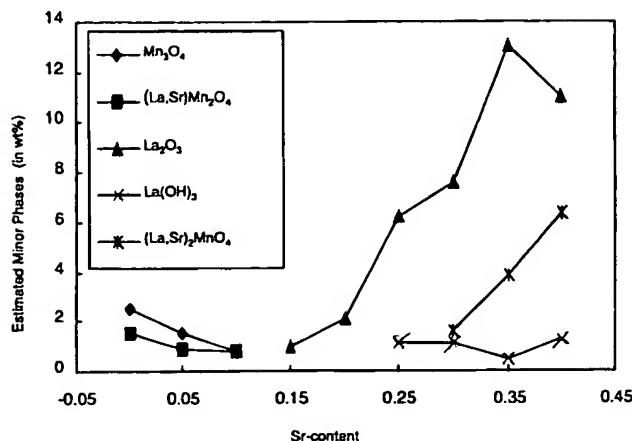


Figure 2. Minor phases in  $La_{0.8}Sr_xMnO_3$  perovskites (sintered at 1200°C for 2 h).

Table V. The lattice constants of the  $La_{0.8}Sr_xMnO_3$  perovskite phase in the La-Sr-Mn-O System.  
A/B cation ratio the in La-Sr-Mn-O system ( $0 \leq x \leq 0.4$ )

	0.800	0.850	0.900	0.950	1.000	1.050	1.100	1.150	1.200
$a^a$	$a = 5.524(2)$	$a = 5.5226(4)$	$a = 5.5234(4)$	$a = 5.5219(6)$	$a = 5.5126(3)$	$a = 5.4959(5)$	$a = 5.5005(6)$	$a = 5.444(2)$	$a = 5.4457(7)$
$b$	$b = 5.524$	$b = 5.5226$	$b = 5.5234$	$b = 5.5219$	$b = 5.5126$	$b = 5.4959$	$b = 5.415(1)$	$b = 5.495(2)$	$b = 5.4981(4)$
$c$	$c = 13.353(5)$	$c = 13.353(1)$	$c = 13.363(2)$	$c = 13.360(2)$	$c = 13.354(1)$	$c = 13.378(2)$	$c = 7.760(1)$	$c = 7.749(2)$	$c = 7.7440(9)$
$V$	$V = 352.9(2)$	$V = 352.69(5)$	$V = 353.07(6)$	$V = 352.80(8)$	$V = 351.44(4)$	$V = 349.95(7)$	$V = 231.12(4)$	$V = 231.82(8)$	$V = 231.86(3)$
$a^b$	$a = 5.5343(4)$	$a = 5.5324(4)$	$a = 5.5318(2)$	$a = 5.5318(2)$	$a = 5.5139(3)$	$a = 5.5033(5)$	$a = 5.5087(7)$	$a = 5.435(2)$	$a = 5.432(2)$
$b$	$b = 5.5343$	$b = 5.5324$	$b = 5.5318$	$b = 5.5318$	$b = 5.5139$	$b = 5.5033$	$b = 5.508$	$b = 5.498(1)$	$b = 5.4967(9)$
$c$	$c = 13.365(1)$	$c = 13.367(1)$	$c = 13.363(2)$	$c = 13.3688(9)$	$c = 13.3595(8)$	$c = 13.377(1)$	$c = 13.383(3)$	$c = 7.755(2)$	$c = 7.754(2)$
$V$	$V = 354.50(5)$	$V = 354.33(3)$	$V = 354.33(3)$	$V = 353.39(4)$	$V = 351.75(3)$	$V = 351.11(6)$	$V = 351.69(9)$	$V = 231.73(9)$	$V = 231.52(8)$

<sup>s</sup> = samples sintered at 1200°C for 2 h.

<sup>q</sup> = after sintering, samples were annealed at 1000°C for 4 h, then quenched on a steel plate.

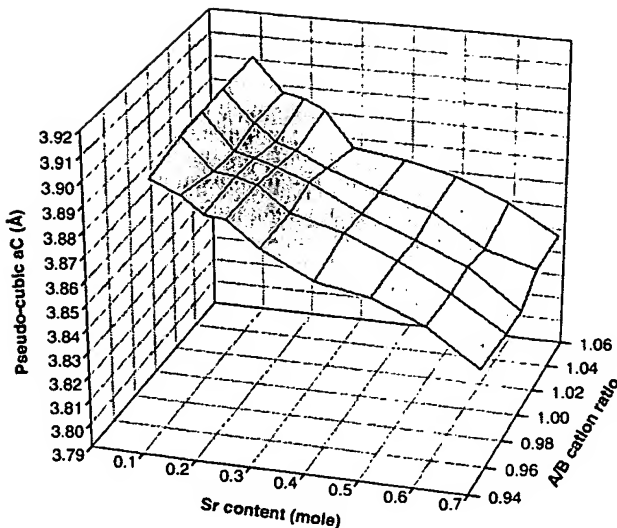


Figure 3. Pseudo-cubic lattice changes vs. Sr content and A/B cation ratio.

and Kaiser,<sup>36</sup> in which they observed  $\text{LaMn}_2\text{O}_4$  at 800°C with an orthorhombic symmetry and lattice constants  $a = 3.88$ ,  $b = 10.09$ , and  $c = 10.05$  Å. However the existence of this phase was not confirmed in a later study conducted by Borlera and Abbattista.<sup>37</sup> Another phase,  $(\text{La}, \text{Sr})_3\text{Mn}_2\text{O}_7$ , is observed only at  $T = 1450^\circ\text{C}$ , which is consistent with reference.<sup>16</sup> The third phase,  $(\text{La}, \text{Sr})_2\text{MnO}_4$ , is stable at all temperatures.

For a cation ratio of unity, no secondary phase is expected to form, however, at least three were detected. The first one was  $\text{La}_2\text{O}_3$ , and then its hydrated product,  $\text{La}(\text{OH})_3$ . It is understood that in a fine-powder system any local atom distribution derivation may favor the formation of the  $\text{La}_2\text{O}_3$ , and  $\text{La}_2\text{O}_3$  can react with the water in air to form  $\text{La}(\text{OH})_3$ .  $\text{La}(\text{OH})_3$  is not a desirable phase in SOFC cathode material, because of its very low melting point ( $\sim 252^\circ\text{C}$ ) and its tendency to swell and degrade the strength of the cathode. Another minor phase found was  $(\text{La}, \text{Sr})_3\text{Mn}_2\text{O}_7$  which can be produced by withdrawing a few Mn atoms from the perovskite structure; the composition fluctuation in the LSM system can make this occur.

All of the secondary phases appeared at  $\text{A}/\text{B} = 1$  [ $\text{La}_2\text{O}_3$ ,  $\text{La}(\text{OH})_3$ ,  $(\text{La}, \text{Sr})_3\text{Mn}_2\text{O}_7$ , and  $(\text{La}, \text{Sr})_2\text{MnO}_4$ ] appeared when  $\text{A}/\text{B} > 1$ . The electrical conductivity of these secondary phases is much lower than that of the LSM perovskite, therefore the presence of these secondary phases degrades SOFC performance ( $\text{Mn}_3\text{O}_4$  is an exception).

Because perovskite was the majority phase present, the morphology of these secondary phases could only be observed at grain boundaries, using high-resolution, high-magnification TEM. Beside the perovskite and the secondary phases mentioned above, small

Table VI. Linear relationship between pseudo-cubic lattice and the Sr-doping content ( $x$ ).

A/B	$a_c$ vs. Sr ( $x$ )	$R^2$
0.900	3.906 - 0.102x	0.993
0.925	3.906 - 0.097x	0.982
0.950	3.906 - 0.095x	0.983
0.980	3.917 - 0.116x	0.951
1.000	3.906 - 0.096x	0.907 <sup>a</sup>
1.020	3.907 - 0.095x	0.930
1.050	3.907 - 0.095x	0.958
1.100	3.910 - 0.097x	0.948

<sup>a</sup> Indicates the influence of secondary phases.

Table VII. Pseudo-cubic lattice constant ( $a_c$ ) of  $\text{La}_{0.8}\text{Sr}_x\text{MnO}_3$  in the La-Sr-Mn-O system.

$x$ (mol)	$a_c$ (Å) (sintered)	$a_c$ (Å) (quenched)
0.000	3.889	3.895
0.050	3.888	3.894
0.100	3.890	3.894
0.150	3.899	3.891
0.200	3.884	3.885
0.250	3.878	3.882
0.300	3.866	3.884
0.350	3.870	3.869
0.400	3.870	3.868

The lattice correlation found in  $\text{La}_{0.8}\text{Sr}_x\text{MnO}_3$

Samples	$a_c$ vs. Sr ( $x$ )	$R^2$
Sintered	3.893 - 0.063x	0.804
Quenched	3.899 - 0.071x	0.879

amounts of  $\text{SrO}$ ,  $\text{SrMnO}_3$ , and  $\text{LaMnO}_3$  were clearly observed using TEM, even though they were not detected using XRPD. Their existence can be explained by basic thermodynamic theory. No matter how homogeneous the initial synthesis was, the material may not have reached equilibrium during the solid-state reaction. Even if the material was equilibrated, composition fluctuations and atom vibrations could still provide nucleation sites locally favorable to form very small particles (phases) of different structure.

By normalizing the intensity of the 100% crystalline peak of each minor phase to that of the primary LSM perovskite, we determined the amount of secondary phases (see Fig. 2). It is worth pointing out that the XRPD resolution limit is often reported as approximately 5 to 1 wt %, however we were able to detect secondary phases of less than 1 wt %. We took two approaches to assure this capability. First, we changed the composition of our test materials systematically so that unindexable peaks repeatedly appeared in X-ray spectra with intensities that reflected the compositions. Second, we made our own "standard" samples with the compositions of the suspected minor phases to compare them to the observed unindexable peaks. The minor-phase behavior in the La-Sr-Mn-O system appeared to be a consistent function of composition, *i.e.*, the doped Sr content and the A/B cation ratio. High Sr doping and significant off-stoichiometry resulted in additional minor phases of higher concentration.

Except for the phase identification, we did not attempt to refine the lattice parameters of the minor phases  $\text{Mn}_3\text{O}_4$ ,  $\text{La}_2\text{O}_3$  and its readily hydrated product  $\text{La}(\text{OH})_3$ , because quality reference patterns are already available from ICDD (for example, PDF 24-734 for  $\text{Mn}_3\text{O}_4$ , 05-0602 for  $\text{La}_2\text{O}_3$ , and 36-1481 for  $\text{La}(\text{OH})_3$ ) that JADE uses. Similar to the phase behavior of the perovskite, the tetragonal-type minor phases  $(\text{La}, \text{Sr})\text{Mn}_2\text{O}_4$ ,  $(\text{La}, \text{Sr})_3\text{Mn}_2\text{O}_7$ , and  $(\text{La}, \text{Sr})_2\text{MnO}_4$  showed a direct relationship with Sr content. Their lattice constants and unit cell volumes also changed with compositions [cf., Table IV for  $(\text{La}, \text{Sr})_3\text{Mn}_2\text{O}_7$  and Table V for  $(\text{La}, \text{Sr})_2\text{MnO}_4$ ].

In general, the results found by using XRPD and TEM (EDS) are consistent with each other within the experimental error. The results are also consistent with available phase diagram information.<sup>16,25,37</sup> Because XRPD detection limit is about 1 wt %, it is impossible to observe very small amounts of secondary phases, *e.g.*, like  $\text{SrO}$ ,  $\text{SrMnO}_3$ , etc. By using high-magnification TEM, these small particles become visible and therefore detectable.

The perovskite single-phase region in the La-Sr-Mn-O system changed with both the Sr content and the A/B cation ratio. If a tolerance of 1 wt % (the XRPD limit) of minor phases can be accepted as a criterion in determining the boundary of the single phase, then a reasonable composition region of the single LSM perovskite can be defined. Table VIII summarizes optimized window for single-phase LSM materials. To obtain the single perovskite phase for the cathode material, it is strongly recommended that the A/B cation ratio be less than unity.

**Table VIII.** The possible single LSM perovskite phase region in the La-Sr-Mn-O system.<sup>a</sup>

A/B	0.900	0.925	0.950	0.980	1.000	1.020	1.050	1.100
Sr	< 0.600	< 0.500	< 0.400	< 0.400	< 0.400	< 0.200	< 0.100	No

<sup>a</sup> As A/B increases, a smaller Sr content is allowed for single LSM perovskite phase.

### Conclusions

With the knowledge of phase behavior and phase relations in the constituent binary and ternary phase diagrams for the La-Sr-Mn-O system, some general conclusions can be drawn.<sup>38</sup>

1. The primary perovskite phase of formula  $(La, Sr)MnO_3$  can have an orthorhombic, monoclinic, or hexagonal-distorted structure.

2. The minor phase  $Mn_3O_4$ , was found when the A/B cation ratio was less than unity (A/B < 1). This minor phase can enhance the performance of the cathode material.

3. The phase  $La_2O_3$  appeared when A/B > 1. This phase is not desirable because of the low conductivity and poor mechanical strength that arise from its hydrated product  $La(OH)_3$ .

4. When the Sr level reaches 0.3 mol or higher, a high-temperature tetragonal phase  $(La, Sr)_2Mn_2O_7$  with a  $\sim 0.38+$ ,  $c \sim 1.99+$  nm was formed. This phase has a low conductivity and is detrimental to the performance of the cathode materials.

5. At lower temperatures (1200°C), the tetragonal-phase  $(La, Sr)Mn_2O_4$  with lattice constants  $a \sim 0.38+$  and  $c \sim 1.2+$  nm was formed. It is believed that this phase is stable only at low temperatures.

6. When A/B > 1,  $(La, Sr)_2MnO_4$  with  $a \sim 0.38+$ ,  $c \sim 1.2+$  nm, was present.

The LSM structure changes with Sr content and thermal history. In most cases, distorted (monoclinic, orthorhombic, or rhombohedral) perovskite was observed but not the ideal cubic symmetry. According to the above analytic results for each individual phase developed in the La-Sr-Mn-O system, the solid solubility region for LSM perovskite was defined (cf., Table VIII) and nonstoichiometry for ternary oxides or so-called double oxides was assumed.

### Acknowledgment

Battelle Memorial Institute is operated by the U.S. Department of Energy under contract DE-AC06-76RLO 1830.

F.Z. was with Washington State University at TriCities, Washington, when this work was conducted. He thanks the Pacific Northwest National Laboratory through Associated Western Universities, Inc., Northwest Division, for a Fellowship for this work. Thanks are extended to Dr. Larry Chick, Dr. Timothy Armstrong, and Dr. Jeffry Stevenson for their help using the GNP method for sample preparation. Thanks are also given to Dr. Jun Liu and Dr. Y. L. Chen for their assistance with the TEM and EDS analysis. Special thanks go to

Greg Coffey for his help on the instrumentation and David E. McCready for X-ray powder diffraction analysis. Dr. Harumi Yokokawa is due special thanks for sending all his papers.

### References

1. N. Q. Minh, *J. Am. Ceram. Soc.*, **76**, 563 (1993).
2. N. Q. Minh and T. Takahashi, *Science and Technology of Ceramic Fuel Cells*, Elsevier Science B.V., Amsterdam (1995).
3. T. Hashimoto, N. Mizutani, and M. Kato, *J. Cryst. Growth*, **84**, 207 (1987).
4. A. Hammouche, E. Siebert, and A. Hammou, *Mater. Res. Bull.*, **24**, 367 (1989).
5. R. Millini, M. F. Gagliardi, and G. Piro, *J. Mater. Sci.*, **29**, 4065 (1994).
6. A. Chakraborty, P. S. Devi, and H. S. Maiti, *Mater. Lett.*, **20**, 63 (1994).
7. P. Shu, L. Tichonova, and U. Guth, *Solid State Ionics*, *Diffusion & Reactions*, **68**, 177 (1994).
8. R. W. Berg, M. M. Andersen, and N. J. Bjerrum, in *Proceedings of 2nd European Solid Oxide Fuel Cell Forum*, B. Thorstensen, Editor, pp. 413-422, Oslo, Norway (1995).
9. Z. T. Zhang, O. Y. Lin, and Z. L. Tang, in *Solid Oxide Fuel Cells IV*, M. Dokiya, H. Tagawa, and S. C. Singhal, Editors, PV 95, p. 502, The Electrochemical Society Proceedings Series, Pennington, NJ (1995).
10. A. Benabad, A. Daoudi, R. Salmon, and G. Le Flem, *J. Solid State Chem.*, **22**, 121 (1977).
11. J. H. Kuo, H. U. Anderson, and D. M. Sparlin, *J. Solid State Chem.*, **83**, 52 (1989).
12. J. H. Kuo, H. U. Anderson, and D. M. Sparlin, *J. Solid State Chem.*, **87**, 56 (1990).
13. J. A. M. Van Roosmalen and E. H. P. Cordfunke, *J. Solid State Chem.*, **110**, 106 (1994).
14. H. Yokokawa, N. Sakai, T. Kawada, and M. Dokiya, *Denki Kagaku*, **57**, 821 (1989).
15. H. Yokokawa, N. Sakai, T. Kawada, and M. Dokiya, *Denki Kagaku*, **57**, 829 (1989).
16. H. Yokokawa, N. Sakai, T. Kawada, and M. Dokiya, *Denki Kagaku*, **58**, 161 (1990).
17. H. Yokokawa, N. Sakai, T. Kawada, and M. Dokiya, *Solid State Ionics*, **52**, 43 (1992).
18. J. Mizusaki, H. Tagawa, K. Naraya, and T. Sasamoto, *Solid State Ionics*, **49**, 111 (1991).
19. A. Belzner, T. M. Gur, and R. A. Huggins, *Solid State Ionics*, **57**, 327 (1992).
20. J. A. M. van Roosmalen and E. H. P. Cordfunke, *Solid State Ionics*, **52**, 303 (1992).
21. J. A. M. van Roosmalen and E. H. P. Cordfunke, *J. Solid Chem.*, **110**, 113 (1994).
22. R. Hildrum, M. Brustad, C. Wang, and W. Johannessen, *Mater. Res. Bull.*, **29**, 851 (1994).
23. J. Kjaer, I. G. Krogh Andersen, N. Mogensen, and E. Skou, in *Proceedings of 1st European Solid Oxide Fuel Cell Forum*, Ulf Bossel, Editor, p. 513, Lucerne, Switzerland (1994).
24. S. Guido, S. Emmanuel, and N. Aristides, *J. Am. Ceram. Soc.*, **78**, 929 (1995).
25. J. A. M. van Roosmalen, P. van Vlaanderen, and E. H. P. Cordfunke, *J. Solid State Chem.*, **114**, 516 (1995).
26. J. A. M. van Roosmalen, J. P. P. Huijsmans, and L. Plom, *Solid State Ionics*, **66**, 279 (1993).
27. R. Hildrum, S. Aasland, and W. Johannessen, *Solid State Ionics*, **66**, 207 (1993).
28. H. Yamada, and H. Nagamoto, in *Proceedings of the 3rd International Symposium on Solid Oxide Fuel Cells*, S. C. Singhal and H. Iwahara, Editors, PV 93-4, p. 213, The Electrochemical Society Proceedings Series, Pennington, NJ (1993).
29. L. A. Chick, L. R. Pederson, G. D. Maupin, J. L. Bates, L. E. Thomas, and G. J. Exarhos, *Mater. Lett.*, **10**, 6 (1990).
30. L. A. Chick, G. D. Maupin, G. L. Graff, L. R. Pederson, D. E. McCready, and J. L. Bates, *Mater. Res. Soc. Symp. Proc.*, **249**, 159 (1992).
31. H. Taguchi, D. Matsuda, and M. Nagao, *J. Am. Ceram. Soc.*, **75**, 201 (1992).
32. A. Chakraborty, P. S. Devi, S. Roy, and H. S. Maiti, *J. Mater. Res.*, **9**, 986 (1994).
33. J. W. Stevenson, P. F. Hallman, T. R. Armstrong, and L. A. Chick, *J. Amer. Ceram. Soc.*, **78**, 505 (1995).
34. J. A. M. van Roosmalen, E. H. P. Cordfunke, and J. P. P. Huijsmans, *Solid State Ionics*, **66**, 285 (1993).
35. F. Zheng and L. R. Pederson, *J. Electrochem. Soc.*, **146**, 2817 (1999).
36. J. Von Sieler and J. Kaiser, *Z. Anorg. Allg. Chem.*, **377**, 316 (1970).
37. M. L. Borlera and F. Abbattista, *J. Less-Common Met.*, **92**, 55 (1983).
38. F. Zheng, M.S. Thesis, Washington State University, TriCities, WA (1996).

## Chemical diffusion in perovskite cathodes of solid oxide fuel cells: the Sr doped $\text{LaMn}_{1-x}\text{M}_x\text{O}_3$ ( $\text{M}=\text{Co, Fe}$ ) systems

S.P.S. Badwal<sup>a,b</sup>, S.P. Jiang<sup>a</sup>, J. Love<sup>b</sup>, J. Nowotny<sup>c,\*</sup>,  
M. Rekas<sup>c</sup>, E.R. Vance<sup>d</sup>

<sup>a</sup>CSIRO, Manufacturing Science and Technology, Private bag 33, Clayton South MDC, Clayton, Victoria 3169, Australia

<sup>b</sup>Ceramic Fuel Cell Limited, 170 Browns Road, Noble Park, Victoria 3174, Australia

<sup>c</sup>Centre for Materials Research in Energy Conversion, School of Materials Science and Engineering, The University of New South Wales, Sydney, NSW 2052, Australia

<sup>d</sup>Australian Nuclear Science and Technology Organisation, Lucas Heights, NSW 2234, Australia

Received 18 May 2000; received in revised form 23 May 2000; accepted 29 August 2000

### Abstract

This paper reports the results of chemical diffusion coefficient measurements for oxygen in  $(\text{La},\text{Sr})(\text{Mn},\text{Co})\text{O}_3$  and  $(\text{La},\text{Sr})(\text{Mn},\text{Fe})\text{O}_3$  using a manometric method in the temperature range of 773 to 1023 K. It was observed that the addition of Fe or Co into  $(\text{La}_{4-x}\text{Sr}_x)_{1-y}\text{MnO}_3$  results in a substantial increase of the chemical diffusion coefficient. In the range 25–100 mol% of Co or Fe substitution at B-site in  $(\text{La},\text{Sr})\text{MnO}_3$ , the chemical diffusion coefficient exhibits much lower activation energy than that in  $(\text{La},\text{Sr})\text{MnO}_3$ . The chemical diffusion data in  $(\text{La},\text{Sr})(\text{Mn},\text{Co})\text{O}_3$  and  $(\text{La},\text{Sr})(\text{Mn},\text{Fe})\text{O}_3$  system determined by the manometric method are generally in agreement with those determined by electrochemical relaxation methods reported in the literature. A comparison of the chemical diffusion data indicates that the oxygen mobility is lowest in  $(\text{La},\text{Sr})\text{MnO}_3$  and highest in  $(\text{La},\text{Sr})\text{CoO}_3$ . © 2001 Elsevier Science Ltd and Techna S.r.l. All rights reserved.

**Keywords:** C. Diffusion; D. Perovskite; SOFC; Sr doped  $\text{LaMn}_{1-x}\text{M}_x\text{O}_3$  ( $\text{M}=\text{Co, Fe}$ )

### 1. Introduction

The studies on the characterisation of cathode materials such as  $(\text{La},\text{Sr})\text{MnO}_3$  (LSM),  $(\text{La},\text{Sr})\text{CoO}_3$  (LSC) and  $(\text{La},\text{Sr})\text{FeO}_3$  (LSF) for solid oxide fuel cells concern mainly with their electrical and ionic conductivity properties [1–14]. These studies aim at the development of an electrode with mixed conduction that would allow efficient transfer of both charge and oxygen species. Specifically, for high performance of the cathode, it is essential that electrons are supplied at the gas/solid interface and that oxygen is transferred at a fast rate through the gas/solid interface and the electrode material. Therefore, it is important that the electrode material exhibits as high as possible both ionic and electronic conduction. On the other hand it is required that the thermal expansion coefficient of the electrode materials

matches with other fuel cell components and the reactivity of the electrode with the solid electrolyte at the temperature of cell operation, which can lead to severe deterioration of its performance, is negligible [1].

LSM is a good electrode material with high electronic conductivity and thermal expansion close to that of other cell components. However, the oxygen-ion conductivity is very low which necessitates that the three phase boundary area between the electrode, electrolyte and the gas phase is maximised for the effective performance of the electrode in fuel cell operating conditions [15]. Replacement of Mn in LSM with Co and Fe results in substantially higher oxygen-ion conduction in comparison with LSM [12,13]. In this respect it would be useful to establish how the oxygen transport kinetics is modified by Co and Fe substitution into LSM at the B-site (or Mn position).

In a previous paper [16], we reported a manometric method for the determination of the chemical diffusion coefficient in oxide electrode materials and compared the chemical diffusion data for LSM with those reported

\* Corresponding author. Tel.: +61-2-9385-6465; fax: +61-2-9385-6459.

E-mail address: j.nowtny@unsw.edu.au (J. Nowotny).

in the literature measured by other techniques such as electrochemical relaxation methods [17]. In this manometric method, the chemical diffusion coefficient can be determined from two different approximate solutions of the Fick's second law, involving the parabolic and the logarithmic equations, which are valid at low and high values of the equilibration degree, respectively [16]. It appears that the diffusion coefficient, which in the case of these materials (LSM, LSC and LSF) is a certain measure of oxygen conduction, is sensitive to the non-stoichiometry of the material. The chemical diffusion coefficient for LSM materials exhibits different values during oxidation and reduction [16]. It also appears that the diffusion data depend on the equilibration degree and, thus the parabolic and the logarithmic equations result in different diffusion data corresponding to the non-stoichiometry range in which the applied kinetic equation is valid. Similar effect was reported for LSC [19].

The purpose of the present paper is to report the measurements of chemical diffusion coefficients in LSC, LSF and their solid solutions with LSM using the manometric method.

## 2. Experimental

The chemical diffusion coefficient of oxygen was measured by a manometric method. In this method the progress of the equilibration is monitored by changes in  $p(O_2)$  as a function of time during oxidation and reduction experiments taking place in quasi-isobaric conditions. The experimental procedure involved evacuation of the reactor at room temperature, heating it under 1 Pa to 1070 K and then changing the temperature to the desired level. The  $p(O_2)$  was isothermally increased (oxidation) or decreased (reduction) step-wise. Each increase of  $p(O_2)$  resulted in a subsequent increase of oxygen consumption by the specimen. This in consequence, led to a slow decrease of  $p(O_2)$  in time,  $\Delta p_t$ , resulting in a new equilibrium at  $\Delta p_\infty$ . The  $p(O_2)$  change due to oxygen consumption served to monitor the equilibration degree ( $\gamma = \Delta p_t / \Delta p_\infty$ ) as a function of time. Similar procedure was applied during the reduction experiments involving successive sudden imposition of a decreased  $p(O_2)$  over an initially equilibrated specimen. Fig. 1 shows an example of the  $p(O_2)$  change corresponding to successive sudden increased  $p(O_2)$  (oxidation experiments) on  $(La_{0.72}Sr_{0.18})(Mn_{0.75}Co_{0.25})O_{3-\delta}$  at 1109 K.

The chemical diffusion coefficient can be determined from approximate solutions of Fick's second law according to Price and Wagner [18]. For long equilibration time, corresponding to large values of the equilibration degree,  $\gamma$ , the logarithmic equation is applicable. For small values of the equilibration degree, the parabolic

equation is applicable. Therefore, based on the equations used, one will have  $D_{\log}$  and  $D_{\text{par}}$ , where the subscripts log and par denote the logarithmic and parabolic equations, respectively. The detailed procedure of the manometric method and the definitions of basic terms applied in considerations of the chemical diffusion coefficient have been described previously [16].

The oxide powders of  $(La, Sr)CoO_3$ ,  $(La, Sr)FeO_3$  and their solid solution with  $(La, Sr)MnO_3$  were prepared by a wet process followed by calcination at 1000°C in air for 24 h. The calcined powders were single phase as indicated by X-ray diffraction spectra. The powder was isopressed into discs with addition of paraffine as binder and the discs were sintered at 1250°C in air for 6 h. The dimension of specimens were ~8 mm in diameter and ~3.8 mm thick. Prior to the measurements, a specimen was slowly heated ( $0.16 \text{ K min}^{-1}$ ) up to 773 K and then slowly cooled ( $0.8 \text{ K min}^{-1}$ ) to room temperature to remove any moist.

In the oxide materials studied in this work, the A-site occupancy was either 100%  $[(La_{0.8}Sr_{0.2})_{10}]$  or 90%  $[(La_{0.8}Sr_{0.2})_9]$  with La/Sr ratio equal to 4 in all cases. Table 1 gives the compositions and the average grain sizes estimated from SEM micrographs of oxide powders. Therefore, all the specimens reported in the present paper can be expressed by a general formula  $(La_{4x}Sr_x)_{1-y}(Mn_{1-z}M_z)O_{3-\delta}$  [Mn = Co, Fe].

## 3. Results and discussion

### 3.1. Effect of sample dimensions

The determination of the chemical diffusion coefficient from the equilibration kinetic for polycrystalline specimens requires knowledge of the mechanism of the equilibration process. Specifically, it is essential to know whether the equilibration is rate controlled by the transport within individual grains or by diffusion through the entire specimen. In order to understand this, the equilibration kinetics for two different thicknesses was determined for the  $(La_{0.8}Sr_{0.2})(Co_{0.75}Mn_{0.25})O_3$  specimen. Fig. 2 shows the rate constant of the equilibration process determined independently according to the parabolic and the logarithmic equations (relevant symbols are defined in Ref. [16]). As seen, in analogy to the effect of specimen thickness already observed for LSM [15], this rate constant is independent of the sample thickness. The same independence of the rate constants on the specimen thickness was also observed for LSF and LSMF materials. This indicates that the equilibration for LSC, LSF and their solid solutions with LSM is rate controlled by the diffusion through individual grains rather than by the transport through the bulk of the specimen. Consequently, a change of  $p(O_2)$  in the gas phase results in

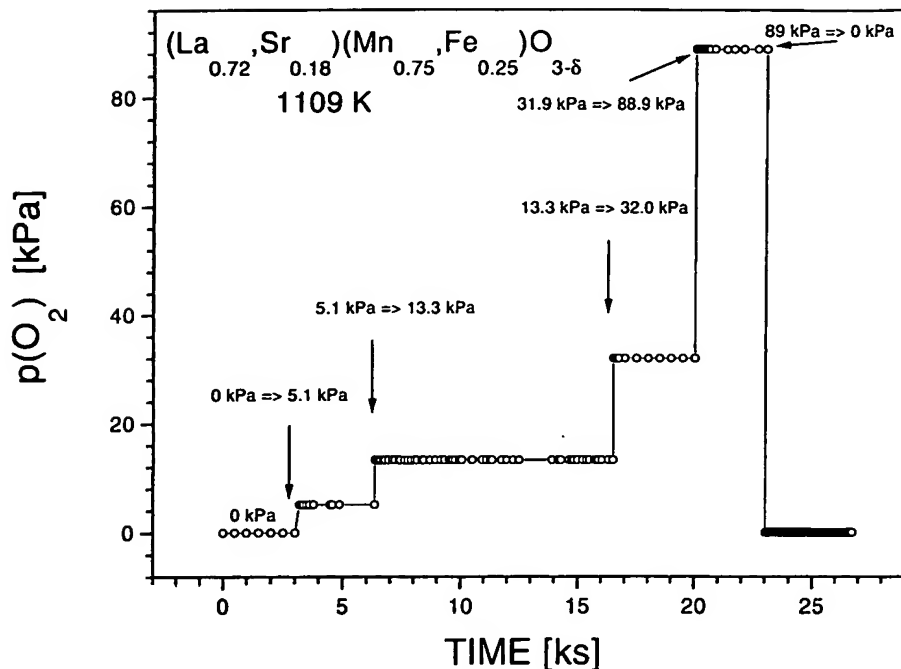


Fig. 1. The change of  $p(O_2)$  corresponding to successive oxidation runs at 1109 K for  $(La_{0.72}Sr_{0.18})(Mn_{0.75}Co_{0.25})O_{3-\delta}$ .

Table I  
Nominal compositions of oxide powders and average grain size of the specimens as measured from SEM micrographs

Specimen	La	Sr	Co	Fe	Mn	O	Grain size (μm)
LSM	0.80	0.20	0	0	1	3	0.6
LSMC10	0.72	0.18	0.10	0	0.90	3	1.0
LSMC25	0.72	0.18	0.25	0	0.75	3	0.6
LSMC50	0.80	0.20	0.50	0	0.50	3	0.8
LSMC75	0.80	0.20	0.75	0	0.25	3	1.0
LSC	0.80	0.20	1	0	0	3	2.0
LSMF25	0.72	0.18	0	0.25	0.75	3	0.6
LSMF50	0.72	0.18	0	0.50	0.50	3	0.6
LSMF75	0.72	0.18	0	0.75	0.25	0	0.6
LSF	0.72	0.18	0	1	0	3	0.5

almost immediate imposition of the same oxygen activity along grain boundaries while equilibration of individual grains is substantially slower.

### 3.2. LSC

The chemical diffusion coefficients for the  $La_{0.8}Sr_{0.2}CoO_{3-\delta}$  (LSC) specimens were determined in the temperature range of 773–1100 K according to the parabolic and logarithmic equations for both oxidation and reduction runs. These data are shown in Fig. 3 along with the data reported in the literature [19,20]. As seen from the chemical diffusion coefficient data obtained in this work cover a wide temperature range (773–1023 K), the upper limit corresponding to normal

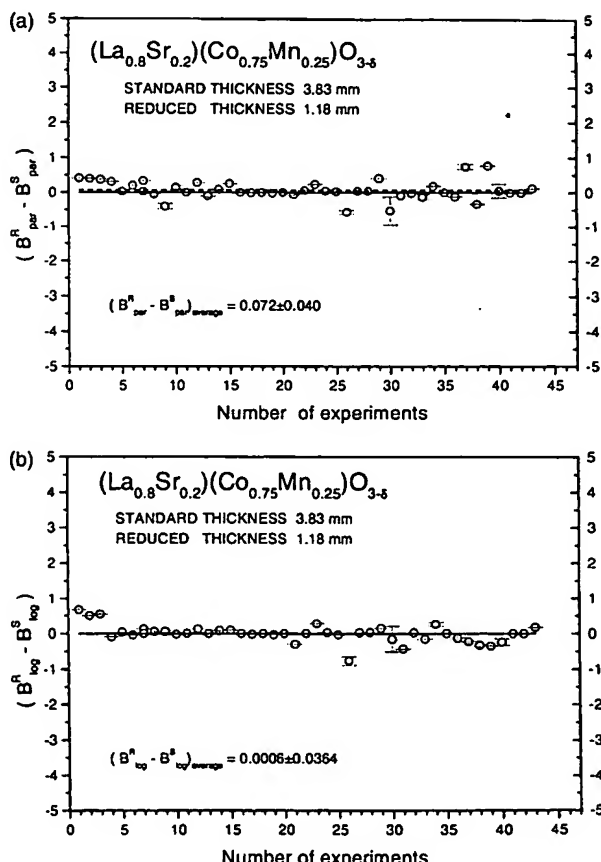


Fig. 2. The difference between the rate constant B of (a) the parabolic equation and (b) the logarithmic equation for the  $(La_{0.8}Sr_{0.2})(Co_{0.75}Mn_{0.25})O_{3-\delta}$  specimens of different thicknesses.

operation temperature of the solid oxide fuel cell with LSC electrodes while most of the literature data [19,20] are reported for temperatures higher than 1100 K.

The diffusion data determined using the parabolic and logarithmic equations corresponds to high and low values of the equilibration degree which, respectively, correspond to the ranges  $0 < \gamma < 0.5$  and  $0.75 < \gamma < 0.98$ . Thus the diffusion coefficient determined from oxidation kinetics using the parabolic and logarithmic equations correspond to the low and the high oxidation state of the specimen, respectively. It appears that the obtained diffusion data are sensitive to the oxidation state and, therefore, exhibit a change with equilibration degree. Similar effect was also observed by Kononchuk et al. [19].

As seen from Fig. 3, the chemical diffusion coefficient for oxidation at 1073 K, determined in this work using the logarithmic equation (high equilibration degree), is higher than that determined from reduction runs by about three orders of magnitude. This discrepancy indicates that the oxygen-ion conduction depends strongly on oxygen nonstoichiometry and the associated defect chemistry. Similar effect has been reported by Kononchuk et al. [19] who observed a strong effect of  $p(O_2)$  on the chemical diffusion coefficient (Fig. 3). Moreover, Kononchuk et al. [19] have shown that the transport kinetics is different at the beginning and at the end of the equilibration process resulting in two different

values of the diffusion coefficient,  $D_{chem-1}$  and  $D_{chem-2}$  (Fig. 3). Similar effect was observed in the present study; the diffusion coefficient determined from the parabolic and logarithmic equations, corresponding to low and high equilibration degree, respectively, assumes different values. It is interesting to note that the activation energy for oxidation is about twice larger than that for reduction (Table 2).

### 3.3. LSM–LSC solid solutions

Fig. 4 shows the effect of Co concentration on the chemical diffusion coefficient for LSC–LSM solid solutions at 550 and 1083 K determined from the parabolic equation for oxidation and reduction runs. Fig. 5 shows the effect of Co concentration on the chemical diffusion coefficient for LSC–LSM solid solutions at 550 and 1083 K determined from the logarithmic equation for oxidation and reduction runs. As seen the replacement of Mn in LSM with Co, resulting ultimately in the formation of LSC, does not lead to marked change in the diffusion coefficient at 1083 K. In contrast, at a lower temperature of 550 K, a substantial increase of the chemical diffusion (by 7–10 orders of magnitude) was observed due to the substitute of Mn by Co at the B-site ( $\gamma=0.25$  or above).

Fig. 6 shows the dependence of the activation energy of the chemical diffusion coefficients on the Co

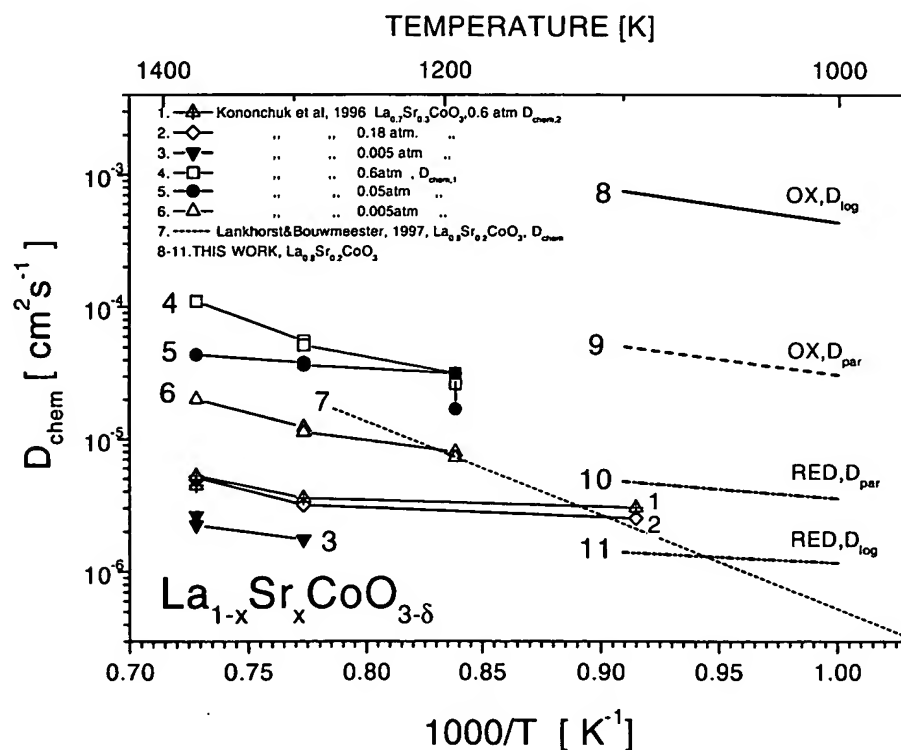


Fig. 3. Comparison of the chemical diffusion coefficient for  $(La_{0.8}Sr_{0.2})CoO_{3-\delta}$  obtained on this work along with the results reported in literature.

concentration for LSC–LSM solid solutions determined from the parabolic equation for oxidation and reduction runs. Fig. 7 shows the similar plots from the logarithmic equation. As seen, addition of Co results in a drop of the activation energy from the level of 100–200

$\text{kJ mol}^{-1}$  to almost a zero at  $y=0.25$  and above. The activation energy values are given in Table 2. This effect indicates that a critical amount of the Co addition, which results in enhancement of oxygen transport kinetics, is 25%. There is little effect of Co on oxygen-ion

**Table 2**  
Activation energy of the chemical diffusion coefficient for LSM–LSC solid solutions

No.	Specimen	Oxidation		Reduction	
		Parabolic (kJ/mol)	Logarithmic (kJ/mol)	Parabolic (kJ/mol)	Logarithmic (kJ/mol)
1	$\text{La}_{0.80}\text{Sr}_{0.20}\text{MnO}_3$	118.92 $\pm$ 22.65	116.63 $\pm$ 27.01	195.73 $\pm$ 1.93	154.84 $\pm$ 14.05
2	$\text{La}_{0.72}\text{Sr}_{0.18}\text{Mn}_{0.90}\text{Co}_{0.10}\text{O}_3$	98.99 $\pm$ 44.53	184.07 $\pm$ 14.36	222.78 $\pm$ 11.37	186.00 $\pm$ 15.81
3	$\text{La}_{0.72}\text{Sr}_{0.18}\text{Mn}_{0.75}\text{Co}_{0.25}\text{O}_3$	14.42 $\pm$ 21.79	0.34 $\pm$ 27.08	31.39 $\pm$ 44.51	28.47 $\pm$ 22.90
4	$\text{La}_{0.80}\text{Sr}_{0.20}\text{Mn}_{0.50}\text{Co}_{0.50}\text{O}_3$	7.51 $\pm$ 2.53	8.99 $\pm$ 6.92	27.44 $\pm$ 6.54	28.83 $\pm$ 8.10
5	$\text{La}_{0.80}\text{Sr}_{0.20}\text{Co}_{0.75}\text{Mn}_{0.25}\text{O}_3$	-10.23 $\pm$ 7.30	-14.65 $\pm$ 7.33	-17.35 $\pm$ 13.08	-28.56 $\pm$ 12.42
6	$\text{La}_{0.80}\text{Sr}_{0.20}\text{CoO}_3$	27.15 $\pm$ 4.27	17.23 $\pm$ 3.53	44.99 $\pm$ 11.45	50.04 $\pm$ 15.30

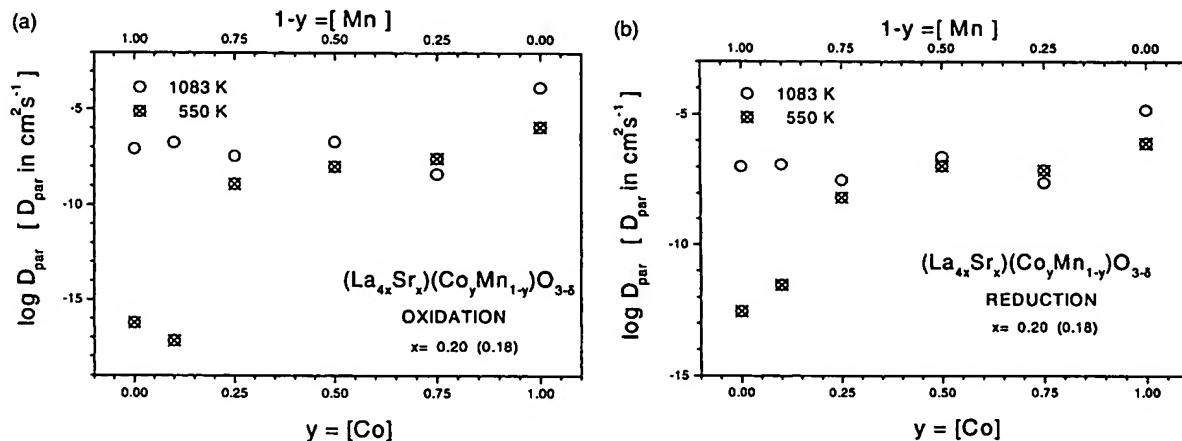


Fig. 4. The chemical diffusion coefficient, determined from the parabolic equation, for  $(\text{La}_{4-x}\text{Sr}_x)(\text{Co}_{1-y}\text{Mn}_{1-y})\text{O}_{3-x}$  as a function of Co concentration at 550 and 1083 K for (a) oxidation and (b) reduction experiments.

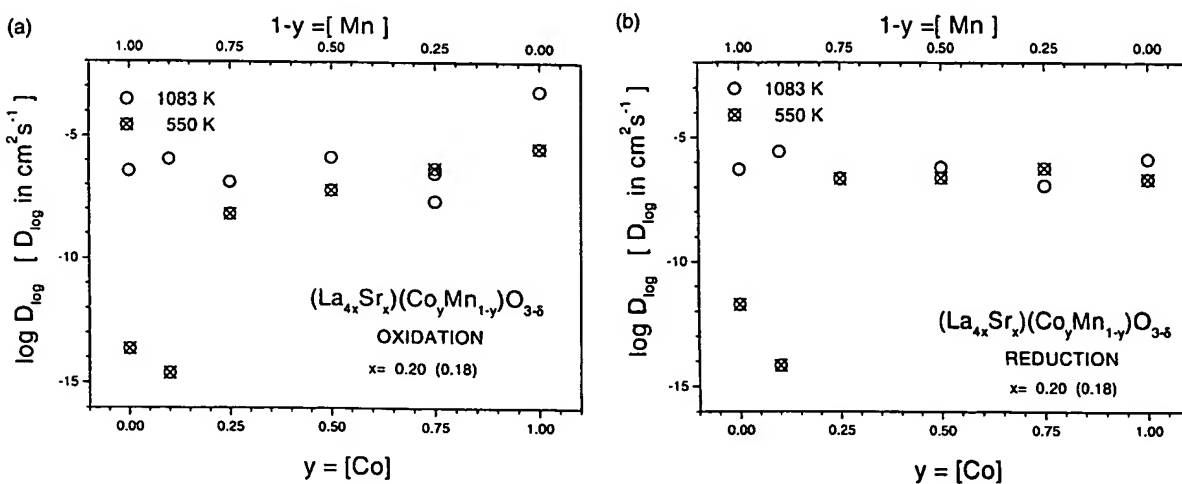


Fig. 5. The chemical diffusion coefficient, determined from the logarithmic equation, for  $(\text{La}_{4-x}\text{Sr}_x)(\text{Co}_{1-y}\text{Mn}_{1-y})\text{O}_{3-x}$  as a function of Co concentration at 550 and 1083 K for (a) oxidation and (b) reduction experiments.

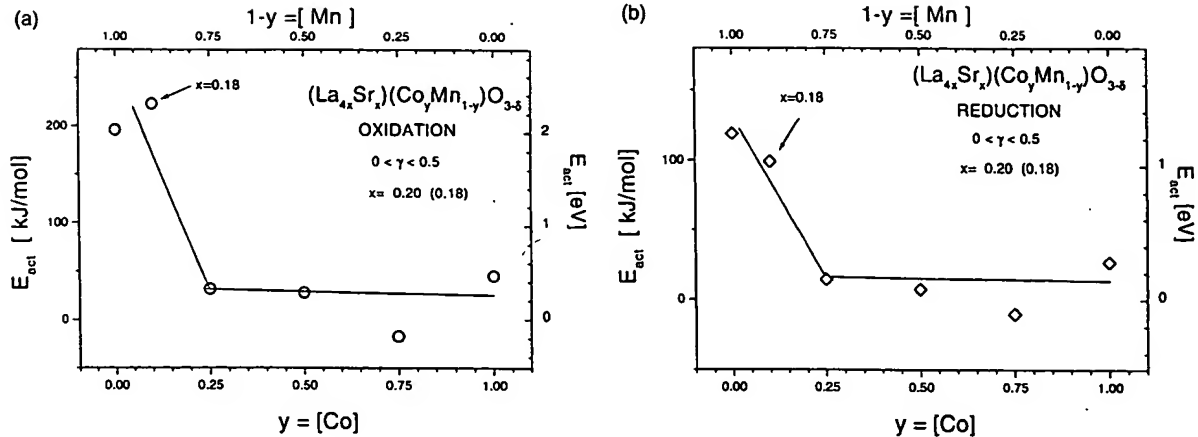


Fig. 6. The activation energy of the chemical diffusion coefficient, determined from the parabolic equation, for  $(La_{4x}Sr_x)(Co_{1-y}Mn_y)O_{3-\delta}$  as a function of Co concentration for (a) oxidation and (b) reduction experiments. The lines show the trend only.

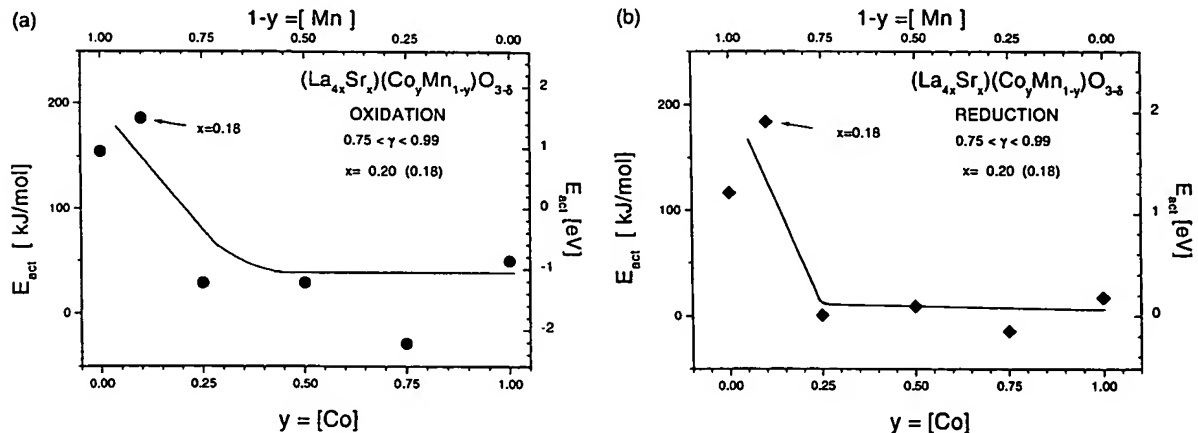


Fig. 7. The activation energy of the chemical diffusion coefficient, determined from the logarithmic equation, for  $(La_{4x}Sr_x)Co_{1-y}Mn_y O_{3-\delta}$  as a function of Co concentration for (a) oxidation and (b) reduction experiments. The lines show the trend only.

conductivity of the Co-doped LSM above this concentration.

It is worth noting that the literature data indicate that substitution of more than 10% Mn at the B-site by Co, significantly reduces the stability of  $(La, Sr)(CoMn)O_3$  electrodes with respect to zirconia electrolytes, thus leading to the formation of  $SrZrO_3$  and  $La_2Zr_7O_7$  at the electrode/electrolyte interface at the fuel cell operating temperatures [1]. The formation of these relatively low conducting phases has a detrimental effect on the long term cell performance.

#### 3.4. LSF

The chemical diffusion coefficient for  $(La_{0.72}Sr_{0.18})FeO_3$  (LSF) was determined in the temperature range of 773 to 1100 K. The chemical diffusion coefficient data determined in the present work was compared with those reported in the literature measured by different

techniques at higher temperatures [5–7,20], as shown in Fig. 8.

The chemical diffusion coefficient for oxidation at 1073 K, determined from the logarithmic equation (high equilibration degree), is higher than that for reduction by about five orders of magnitude. Since oxidation and reduction correspond to different non-stoichiometry, the observed discrepancy indicates that non-stoichiometry has a substantial effect on oxygen conduction. This effect is markedly larger than that observed for LSC (see Fig. 3).

Elshof et al. [7] argue that at  $p(O_2)$  lower than 30 Pa, the oxygen exchange process is rate controlled by a reaction at the gas/solid interface rather than by the bulk diffusion. This is not in agreement with the results obtained in this study indicating that the equilibration kinetics is rate controlled by diffusive lattice transport. However, the effect of the surface may be related to a segregation-induced diffusive resistance within the surface

layer [21]. This effect may be responsible for the difference in the activation energy between oxidation and reduction experiments.

According to this model the equilibration kinetics for reduction is rate controlled by this diffusion resistance while the diffusion data obtained for oxidation seem to correspond to the bulk transport kinetics. Similar effect was observed for LSC specimens. The observed dissim-

ilarity between reduction and oxidation kinetics may well be explained in terms of an effect of oxygen non-stoichiometry on the transport kinetics.

As seen from Fig. 8 the absolute values of the diffusion data reported in Ref. [7] are larger than those reported in this work for reduction. As also seen the diffusion data obtained in this work for LSF during oxidation exhibit exceptionally high values.

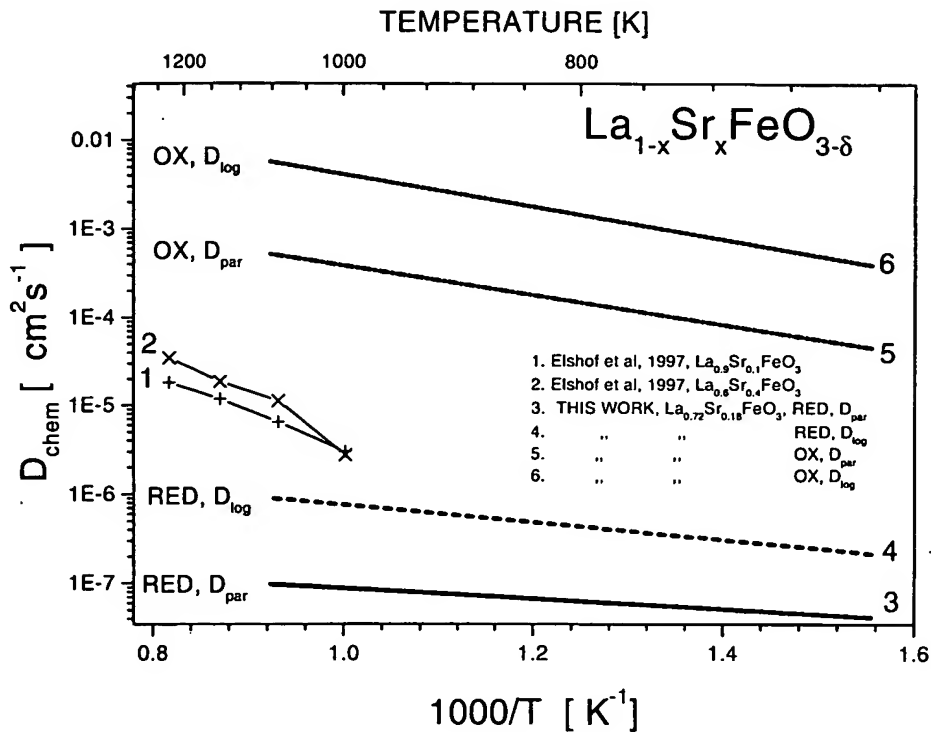


Fig. 8. Comparison of the chemical diffusion coefficient for  $(La_{0.72}Sr_{0.18})FeO_{3-\delta}$  determined according to parabolic and logarithmic equations during both oxidation and reduction experiments with literature data.

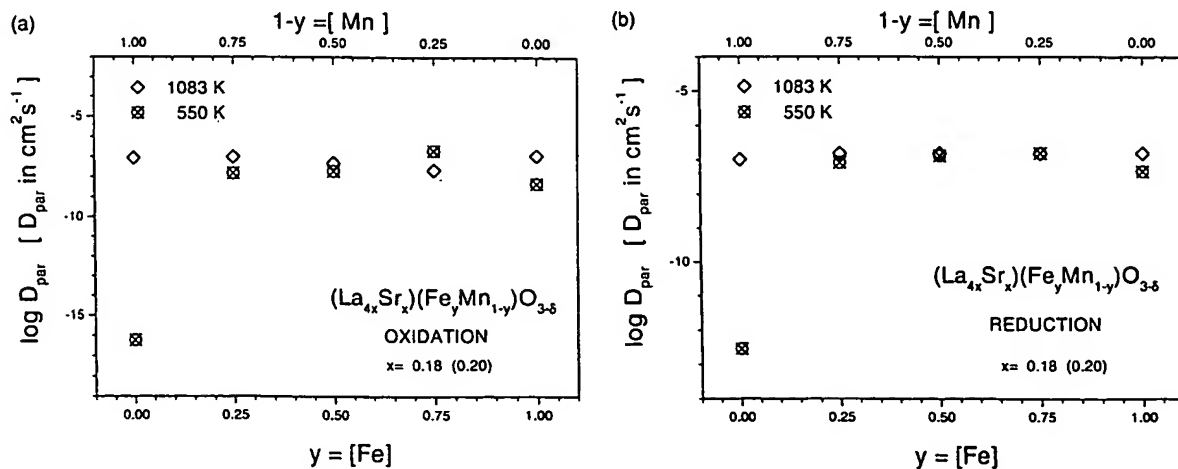


Fig. 9. The chemical diffusion coefficient, determined from the parabolic equation, for  $(La_{4-x}Sr_x)(Fe_{1-y}Mn_y)O_{3-\delta}$  as a function of Fe content at 550 and 1083 K for (a) oxidation and (b) reduction experiments.

### 3.5. LSM–LSF solid solutions

Fig. 9 illustrates the chemical diffusion coefficient for LSM–LSF solid solutions as a function of Fe concentration determined from parabolic equation during reduction and oxidation at 550 and 1083 K. Fig. 10 the data determined from the logarithmic equation. In analogy to the effect of Co substitution in LSM–LSC solid solutions, addition of Fe into  $(\text{La},\text{Sr})\text{MnO}_3$  results in a substantial increase of the chemical diffusion coefficient by about 10 orders of magnitude at 550 K, while at 1083 K the chemical diffusion coefficient becomes almost independent of the Fe content.

The effect of Fe content on the activation energy of chemical diffusion coefficient is also similar to that of Co content in LSM–LSC solid solutions, as shown in Figs. 11 and 12. Addition of Fe results in a drop of the activation energy which assumes a close-to-zero level for

both LSF and Fe-doped LSM. The activation energy values are summarised in Table 3. It is interesting to note that in analogy to the Co-doped LSM, at  $y = 0.75$  of Fe, the chemical diffusion coefficient becomes practically independent of temperature.

As seen, the activation energy for undoped LSF during oxidation ( $E_{\text{par}} 30 \text{ kJ mol}^{-1}$ ,  $E_{\log} 34 \text{ kJ mol}^{-1}$ ) is substantially larger than that for reduction ( $E_{\text{par}} 11 \text{ kJ mol}^{-1}$ ,  $E_{\log} 18 \text{ kJ mol}^{-1}$ ). This difference indicates that the same effects, considered for LSM and LSC, have an application also in this case.

### 3.6. Comparison of LSM, LSC and LSF

Arrhenius plots of the chemical diffusion coefficient for LSM (reported previously [16]), LSC and LSF, determined from parabolic and logarithmic equations during oxidation and reduction at different values of the

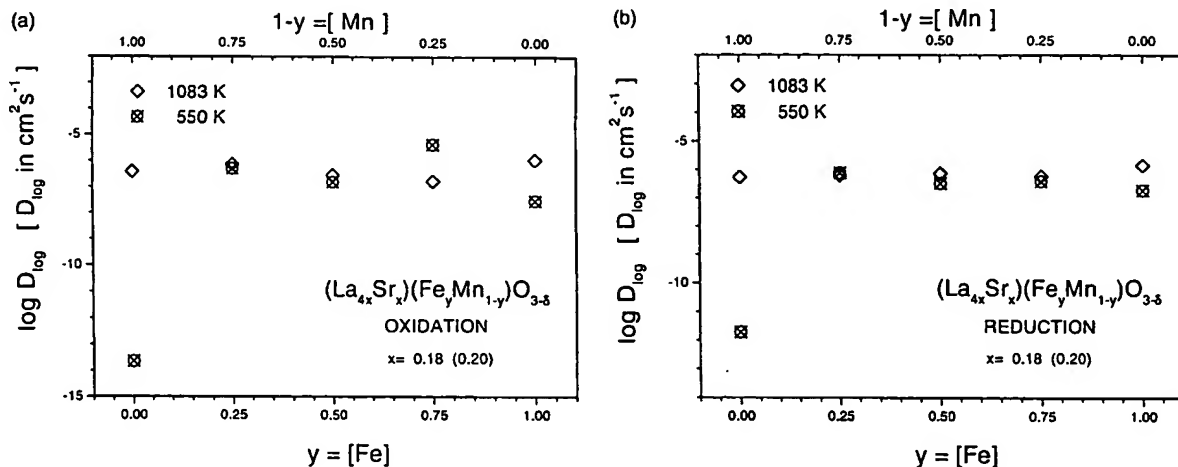


Fig. 10. The chemical diffusion coefficient, determined from the logarithmic equation, for  $(\text{La}_{4-x}\text{Sr}_x)(\text{Fe}_1-y\text{Mn}_y)\text{O}_{3-\delta}$  as a function of Fe content at 550 and 1083 K for (a) oxidation and (b) reduction experiments.

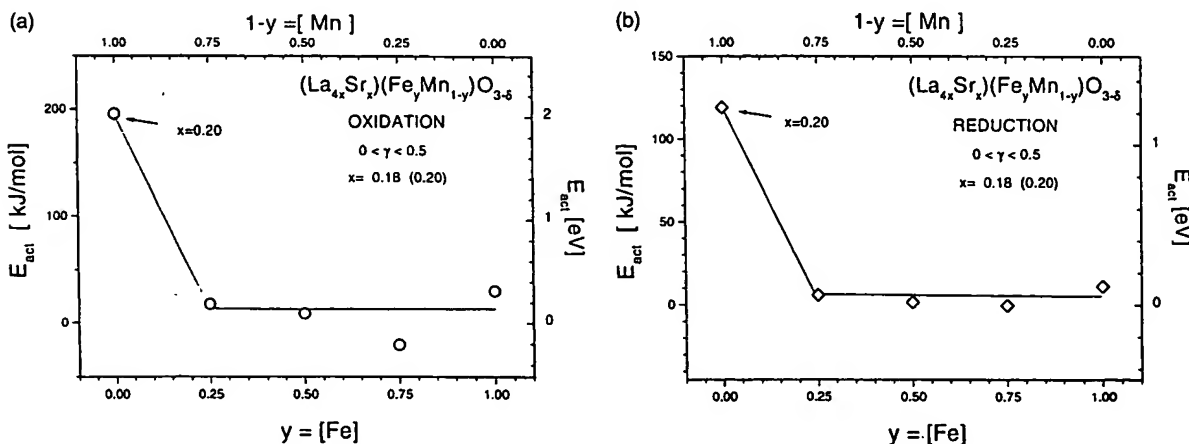


Fig. 11. The activation energy of the chemical diffusion coefficient, determined from the parabolic equation, for  $(\text{La}_{4-x}\text{Sr}_x)(\text{Fe}_1-y\text{Mn}_y)\text{O}_{3-\delta}$  as a function of Fe content for (a) oxidation and (b) reduction experiments. The lines show the trend only.

equilibration degree, are shown in Figs. 13 and 14. Comparison of these diffusion data results in the following general conclusions.

1. The diffusion data obtained during oxidation are always higher than those for reduction. The dissimilarity may be explained in terms of the effect of either (i) oxygen non-stoichiometry on the

kinetics or (ii) segregation-induced diffusive resistance [21].

2. In all cases the chemical diffusion coefficient for LSM is substantially lower than that for LSC and LSF, although the difference is substantially reduced at 1100 K.
3. The transport in LSC is higher than that in LSF by the factor of approximately 10.

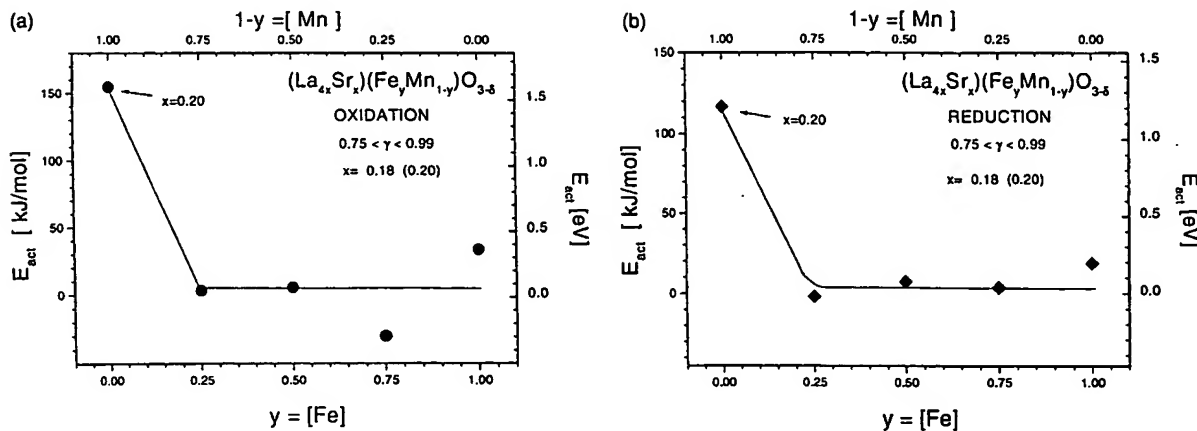


Fig. 12. The activation energy of the chemical diffusion coefficient, determined from the logarithmic equation, for  $(La_{4-x}Sr_x)(Fe_{1-y}Mn_y)O_{3-x}$  as a function of Fe content for (a) oxidation and (b) reduction experiments.

Table 3  
Activation energy of the chemical diffusion coefficient for LSM–LSF solid solutions

No.	Specimen	Reduction		Oxidation	
		Parabolic (kJ/mol)	Logarithmic (kJ/mol)	Parabolic (kJ/mol)	Logarithmic (kJ/mol)
1	$La_{0.80}Sr_{0.20}MnO_3$	$118.92 \pm 22.65$	$116.63 \pm 27.01$	$195.73 \pm 1.93$	$154.84 \pm 14.05$
2	$La_{0.72}Sr_{0.18}Mn_{0.75}Fe_{0.25}O_3$	$5.67 \pm 6.03$	$-1.87 \pm 4.15$	$17.32 \pm 6.83$	$3.38 \pm 6.91$
3	$La_{0.72}Sr_{0.18}Fe_{0.50}Mn_{0.50}O_3$	$1.55 \pm 1.56$	$7.38 \pm 2.01$	$8.47 \pm 7.48$	$5.76 \pm 7.25$
4	$La_{0.72}Sr_{0.18}Fe_{0.75}Mn_{0.25}O_3$	$-0.30 \pm 2.15$	$-3.75 \pm 3.07$	$-20.85 \pm 17.17$	$-30.11 \pm 15.56$
5	$La_{0.72}Sr_{0.18}FeO_3$	$11.24 \pm 6.80$	$18.47 \pm 7.37$	$29.63 \pm 9.34$	$33.74 \pm 9.74$

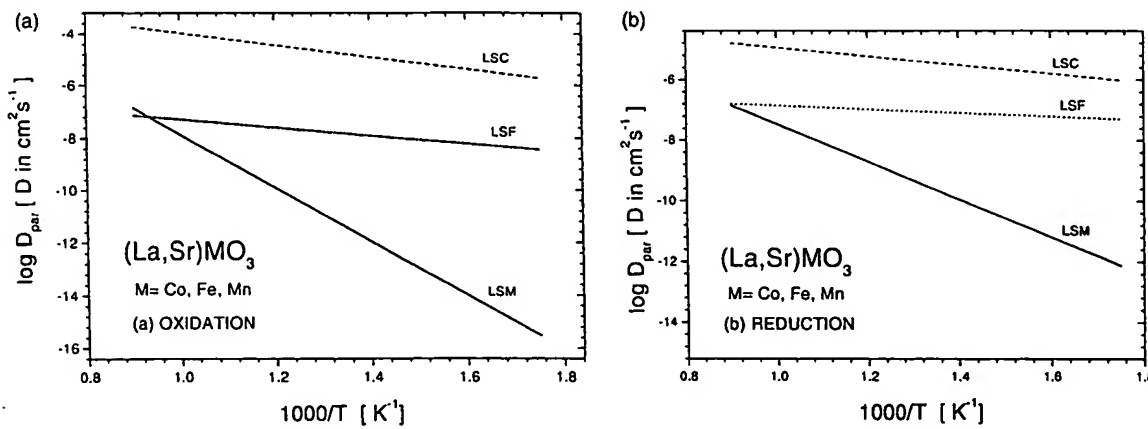


Fig. 13. The chemical diffusion coefficient as a function of reciprocal of temperature, for LSM, LSC and LSF, determined according to the parabolic equation during (a) oxidation and (b) reduction runs.

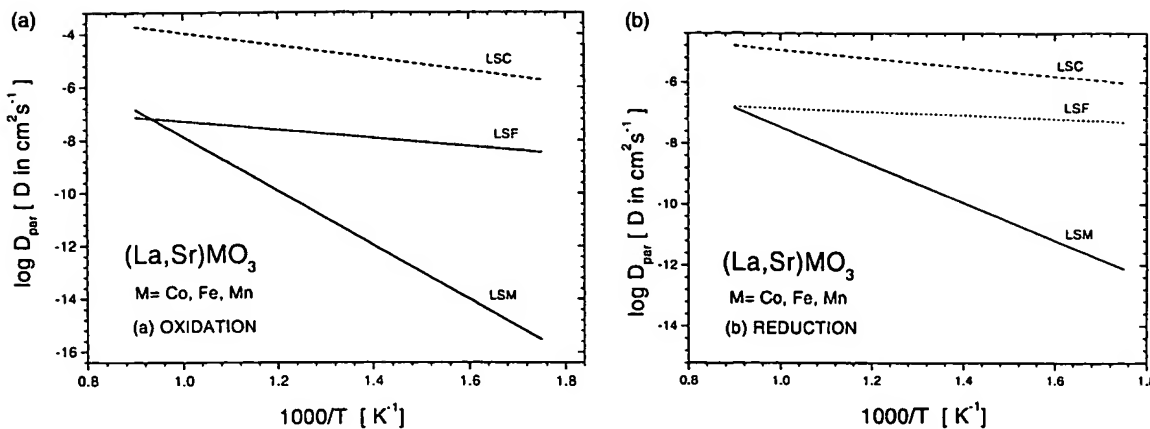


Fig. 14. The chemical diffusion coefficient as a function of reciprocal of temperature, for LSM, LSC and LSF, determined according to the logarithmic equation during (a) oxidation and (b) reduction runs.

The activation energy of the chemical diffusion coefficient assumes comparable values for both LSC and LSF, which remains in the range 10–27 kJ mol<sup>-1</sup> for reduction and 30–50 kJ mol<sup>-1</sup> for oxidation. The activation energy for LSM assumes substantially larger values (115–119 and 155–196 kJ mol<sup>-1</sup> for oxidation and reduction, respectively), than that for LSC and LSF. In other words addition of both Co and Fe into LSM results in a substantial drop of the activation energy of the equilibration process during both reduction and oxidation.

#### 4. Conclusions

Based on the manometric method we have determined the chemical diffusion coefficients in electrode materials LSC, LSF and their solid solutions with LSM. The diffusion coefficients for undoped LSC and LSF are substantially larger than that for LSM. Also the chemical diffusion coefficient for LSC and LSF exhibits markedly lower activation energy than that of LSM. It appears that substitution of Mn with Co or Fe in LSM above 25 mol% results in a substantial increase of oxygen mobility which is independent of temperature.

It has been shown that the equilibration mechanism of LSC and LSF and their solid solutions with LSM involves a very fast transport of oxygen along grain boundaries and substantially slower process of transport through individual grains. Thus it is possible that lowering of the grain size of the electrode materials may result in an increase of oxygen transfer through the materials.

The dissimilar kinetics for oxidation and reduction may be considered in terms of two effects:

1. The effect of oxygen nonstoichiometry, and related defects concentrations, on transport;

2. The effect of segregation-induced diffusive resistance and related electric fields on transport of charged defects [21]. Evaluation of this effect requires studies on segregation and its impact on the local transport within the segregation-induced concentration barriers would be needed to verify the effect of the surface diffusion resistance, if any.

Comparison of the diffusion data for the undoped specimens of LSM, LSC and LSF indicates that LSM is characterised by the low chemical diffusion coefficient and the high value of the activation energy while LSC and LSF exhibits the high diffusion coefficient and the low activation energy. The substantial difference in the chemical diffusion coefficient observed for LSM on one side and for both LSC and LSF on the other side may be considered in terms of the predominant defects that are responsible for ionic conduction. Namely, in the high p(O<sub>2</sub>) regime, which corresponds to the experimental conditions applied in the present study, the predominant defects in LSM are cation vacancies [13] while the transport in both LSC, LSF and their solid solutions predominantly occurs via oxygen vacancies [14] which are much faster than cation vacancies.

#### Acknowledgements

This paper was supported by the Ceramic Fuel Cell Limited. This support is gratefully acknowledged. The oxide powders were prepared by Dr. S. Rajendran.

#### References

- [1] S.P.S. Badwal, K. Fogar, Mater. Forum 21 (1997) 183.
- [2] Y. Matsumoto, S. Yamada, T. Nishida, R. Sato, J. Electroanal. Chem. 127 (1980) 2360–2364.

- [3] T. Ishigaki, S. Yamauchi, J. Mizusaki, K. Fueki, Tracer diffusion coefficient of oxide ions in  $\text{LaCoO}_3$  single crystals, *J. Solid State Chem.* 54 (1984) 100–107.
- [4] L. Qiu, T.H. Lee, L.-M. Liu, Y.L. Young, A.J. Jacobson, Oxygen permeation studies of  $\text{SrCo}_{0.8}\text{Fe}_{0.2}\text{O}_{3-\delta}$ , *Solid State Ionics* 76 (1995) 321–329.
- [5] B. Ma, U. Balachandran, J.-H. Park, C.U. Segre, Determination of the chemical diffusion coefficient of  $\text{SrFeCo}_{0.5}\text{O}_x$  by the conductivity relaxation method, *Solid State Ionics* 83 (1996) 65–71.
- [6] J.E. Elshof, M.H.R. Lankhorst, H.J.M. Bouwmeester, Oxygen exchange and diffusion coefficient of strontium-doped lanthanum ferrites by electrical conductivity relaxation, *J. Electrochem. Soc.* 144 (1997) 1060–1067.
- [7] J.E. Elshof, M.H.R. Lankhorst, H.J.M. Bouwmeester, Chemical diffusion coefficient and oxygen exchange of  $\text{La}_{0.6}\text{Sr}_{0.4}\text{Co}_{0.6}\text{Fe}_{0.4}\text{O}_{3-\delta}$ , *Solid State Ionics* 99 (1997) 15–22.
- [8] S. Guggilla, A. Manthiram, Crystal chemical characterisation of the mixed conductor  $\text{Sr}(\text{Fe},\text{Co})_{1.5}\text{O}_y$  exhibiting unusually high oxygen permeability, *J. Electrochem. Soc.* 144 (1997) L120–L125.
- [9] J. Nowotny, M. Rekas, *J. Am. Ceram. Soc.* 81 (1998).
- [10] T. Bak, J. Nowotny, M. Rekas, C.C. Sorrell, *J. Phys. Chem. Solids*, in press.
- [11] I. Yasuda, K. Ogasawara, M. Hishinuma, T. Kawada, M. Dokiya, *Solid State Ionics* 86–88 (1996) 1197–1201.
- [12] B.C.H. Steele, S. Carter, Kajda, I. Kontoulis, J.A. Kilner, in: F. Grosz, P. Zeglers, C.C. Singhal, O. Yamamoto (Eds), *Proc. 2nd Int. Symp. on SOFC*, 1991, pp. 517–525.
- [13] S. Carter, A. Seluck, R.J. Chater, J. Kajda, J.A. Kilner, B.C.H. Steele, *Solid State Ionics* 53–56 (1992) 597–605.
- [14] J. Wolfenstine, T.R. Armstrong, W.J. Weber, M.A. Bloing-Risser, K.C. Goretta, J.L. Routbord, *J. Mater. Res.* 11 (1996) 657.
- [15] F.H. van Heuveln, H.J.M. Bouwmeester, F.P.F. van Berkel, *J. Electrochem. Soc.* 144 (1997) 126.
- [16] S.P.S. Badwal, S.P. Jiang, J. Love, J. Nowotny, M. Rekas, *J. Austral. Ceram. Soc.* 34 (1998) 154.
- [17] A. Betzner, T.M. Gur, R.A. Huggins, *Solid State Ionics* 57 (1992) 327–337.
- [18] J.B. Price, J.B. Wagner Jr., *Z. Physik. Chem., Neue Folge* 49 (3–4) (1966) 257.
- [19] O.F. Kononchuk, D.P. Sutija, T. Norby, P. Kofstad, in: S.C. Singhal (Ed.), *Proc. 4th Int. Symp. on SOFC*, The Electrochemical Society, Pennington, NJ, 1995, pp. 395–403.
- [20] M.R.H. Lankhorst, H.J.M. Bouwmeester, *J. Electrochem. Soc.* 144 (1997) 1261.
- [21] Z. Adamczyk, J. Nowotny, *J. Phys. Chem. Solids* 47 (1986) 11.



ELSEVIER

Solid State Ionics 126 (1999) 143–151

**SOLID  
STATE  
IONICS**

[www.elsevier.com/locate/ssi](http://www.elsevier.com/locate/ssi)

## Properties of A-site-deficient $\text{La}_{0.6}\text{Sr}_{0.4}\text{Co}_{0.2}\text{Fe}_{0.8}\text{O}_{3-\delta}$ -based perovskite oxides

G.Ch. Kostogloudis\*, Ch. Ftikos

*Laboratory of Inorganic Materials Technology, Department of Chemical Engineering, National Technical University of Athens, 9 Heroon Polytechniou Str., Zografou Campus, GR-157 80 Athens, Greece*

Received 21 April 1999; received in revised form 11 June 1999; accepted 9 July 1999

### Abstract

A-site-deficient  $\text{La}_{0.6}\text{Sr}_{0.4}\text{Co}_{0.2}\text{Fe}_{0.8}\text{O}_{3-\delta}$ -based oxides of the compositions  $\text{La}_{0.6-z}\text{Sr}_{0.4}\text{Co}_{0.2}\text{Fe}_{0.8}\text{O}_{3-\delta}$ ,  $\text{La}_{0.6}\text{Sr}_{0.4-z}\text{Co}_{0.2}\text{Fe}_{0.8}\text{O}_{3-\delta}$  and  $(\text{La}_{0.6}\text{Sr}_{0.4})_{1-z}\text{Co}_{0.2}\text{Fe}_{0.8}\text{O}_{3-\delta}$  ( $0 \leq z \leq 0.2$ ) were prepared and characterized. The crystal structure, electrical conductivity and thermal expansion of these oxides were studied using X-ray diffraction, four-point DC and dilatometry, respectively. All oxides had a rhombohedral perovskite structure. The pseudo-cubic lattice parameter increased with increasing  $z$ . The electrical conductivity increased with temperature up to about 600°C, and then decreased due to the loss of lattice oxygen. The charge compensation mechanism in these A-site-deficient perovskites was probably the formation of oxygen vacancies rather than the oxidation  $\text{B}^{3+} \rightarrow \text{B}^{4+}$ . The conductivity decrease and the activation energy increase became more significant in the order  $\text{La}_{0.6}\text{Sr}_{0.4-z} > (\text{La}_{0.6}\text{Sr}_{0.4})_{1-z} > \text{La}_{0.6-z}\text{Sr}_{0.4}$ . The TEC was generally lower in the A-site-deficient oxides. The lowest TEC values at 700°C were 14.2, 14.1 and  $13.8 \times 10^{-6} \text{ cm (cm}^\circ\text{C)}^{-1}$  for  $\text{La}_{1-z}\text{Sr}_{0.4}\text{Co}_{0.2}\text{Fe}_{0.8}\text{O}_{3-\delta}$ , with  $z = 0.05$ , and  $\text{La}_{0.6}\text{Sr}_{0.4-z}\text{Co}_{0.2}\text{Fe}_{0.8}\text{O}_{3-\delta}$ , with  $z = 0.1$  and 0.2, respectively. © 1999 Elsevier Science B.V. All rights reserved.

**Keywords:** A-site-deficient perovskite oxides; SOFC cathodes; Crystal structure; Electrical conductivity; Thermal expansion

### 1. Introduction

The perovskite oxide  $\text{La}_{0.6}\text{Sr}_{0.4}\text{Co}_{0.2}\text{Fe}_{0.8}\text{O}_{3-\delta}$  has been suggested by many investigators as a cathode material for solid oxide fuel cells (SOFCs) operating at intermediate temperatures (500–700°C) [1–3]. Moreover, it has been successfully employed in SOFCs operating at 700°C, using  $\text{Ce}_{0.9}\text{Gd}_{0.1}\text{O}_{1.95}$  (CGO) solid electrolyte [4–6]. However, problems

regarding the thermal expansion and chemical compatibility of the two materials are of concern. The thermal expansion coefficient (TEC) of  $\text{La}_{0.6}\text{Sr}_{0.4}\text{Co}_{0.2}\text{Fe}_{0.8}\text{O}_{3-\delta}$  is reported to be  $15.3 \times 10^{-6} \text{ cm (cm}^\circ\text{C)}^{-1}$  at 600°C [1]. This value is 22% greater than the TEC value of CGO, which is  $12.5 \times 10^{-6} \text{ cm (cm}^\circ\text{C)}^{-1}$  [7], and problems may arise during heating and cooling cycles of the cell. As an effort to overcome this problem, A-site-deficient compositions based on  $\text{La}_{0.6}\text{Sr}_{0.4}\text{Co}_{0.2}\text{Fe}_{0.8}\text{O}_{3-\delta}$  were prepared and characterized in this study. The oxides synthesized belong to the systems  $\text{La}_{0.6-z}\text{Sr}_{0.4}\text{Co}_{0.2}\text{Fe}_{0.8}\text{O}_{3-\delta}$ ,  $\text{La}_{0.6}\text{Sr}_{0.4-z}\text{Co}_{0.2}\text{Fe}_{0.8}\text{O}_{3-\delta}$

\*Corresponding author. Tel.: +30-1-772-3245; fax: +30-1-772-3244.

E-mail address: [gkostog@central.ntua.gr](mailto:gkostog@central.ntua.gr) (G.C. Kostogloudis)

$_{3-\delta}$  and  $(La_{0.6}Sr_{0.4})_{1-z}Co_{0.2}Fe_{0.8}O_{3-\delta}$ , where  $z = 0, 0.05, 0.1, 0.2$ . The crystal structure, electrical conductivity and thermal expansion of these oxides were studied.

## 2. Experimental

The powders were prepared by citrate synthesis and pyrolysis [8,9]. Calcination of the powders was performed at 1100°C for 15 h in air, followed by wet milling with acetone for 48 h in a satellite-type milling apparatus, using zirconia balls. The milled products were dried, and then compacted in pellets of 25 mm diameter, by uniaxial pressing at 250 MPa. Dense samples were obtained by sintering the compacts at 1300°C for 15 h in air. A slow rate of 1°C/min was used during heating and cooling. Rectangular bars of approximate dimensions 20 × 2 × 1 mm were cut from the sintered pellets. The bulk density of the samples was calculated by measuring the mass ( $\pm 0.0001$  g accuracy) and the dimensions ( $\pm 0.001$  mm accuracy) of the bars.

Densities above 93% of the theoretical values were achieved for all samples.

The crystal structure and lattice parameters were determined at room temperature by X-ray powder diffraction (XRD) on powders of the sintered samples. A Siemens diffractometer was used (Cu K $\alpha$ ), operated at 40 kV and 30 mA. The scanning rate was 1.2°  $2\theta$ /min in the range 10–80°  $2\theta$ . The lattice parameters were determined by a least-squares unit cell refinement computer program (LSUCR).

The electrical conductivity was measured in air by the four-point DC method on the sintered rectangular bars. The measurements were performed from 100 to 1000°C. The voltage ( $V$ ) between the two inner electrodes and the current intensity ( $I$ ) were recorded on changing the voltage applied to the two outer electrodes. The conductivity ( $\sigma$ ) was determined from a set of  $I - V$  values by taking  $\sigma = L/A \times dI/dV$ . The measurements were performed at low  $V$  and  $I$  values to ensure the validity of Ohm's law.

The thermal expansion coefficients of the specimens were measured in the temperature range 20–1000°C in air, using a quartz dilatometer.

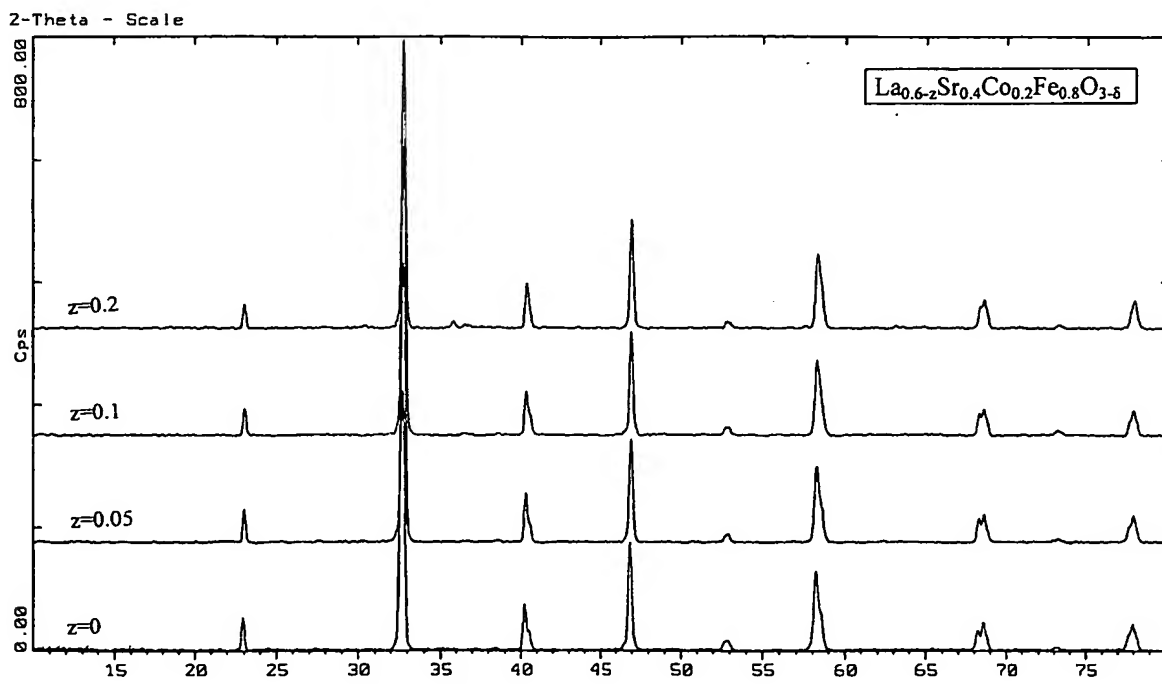


Fig. 1. X-ray diffraction patterns of  $La_{0.6-z}Sr_{0.4}Co_{0.2}Fe_{0.8}O_{3-\delta}$ .

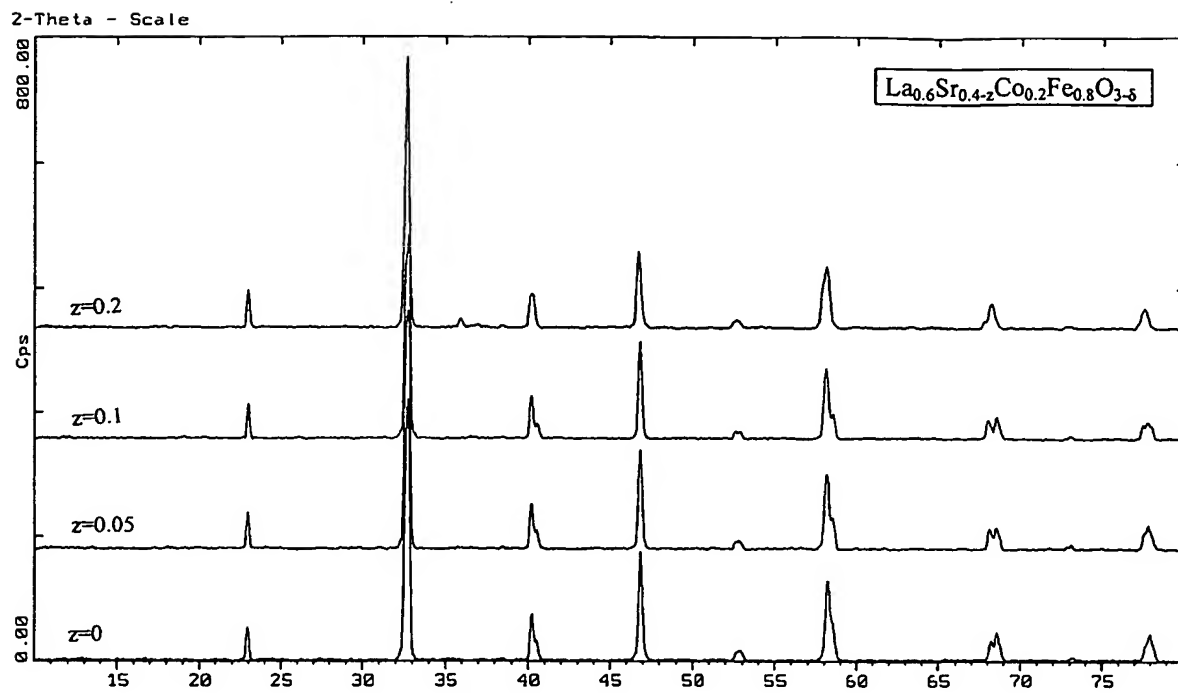
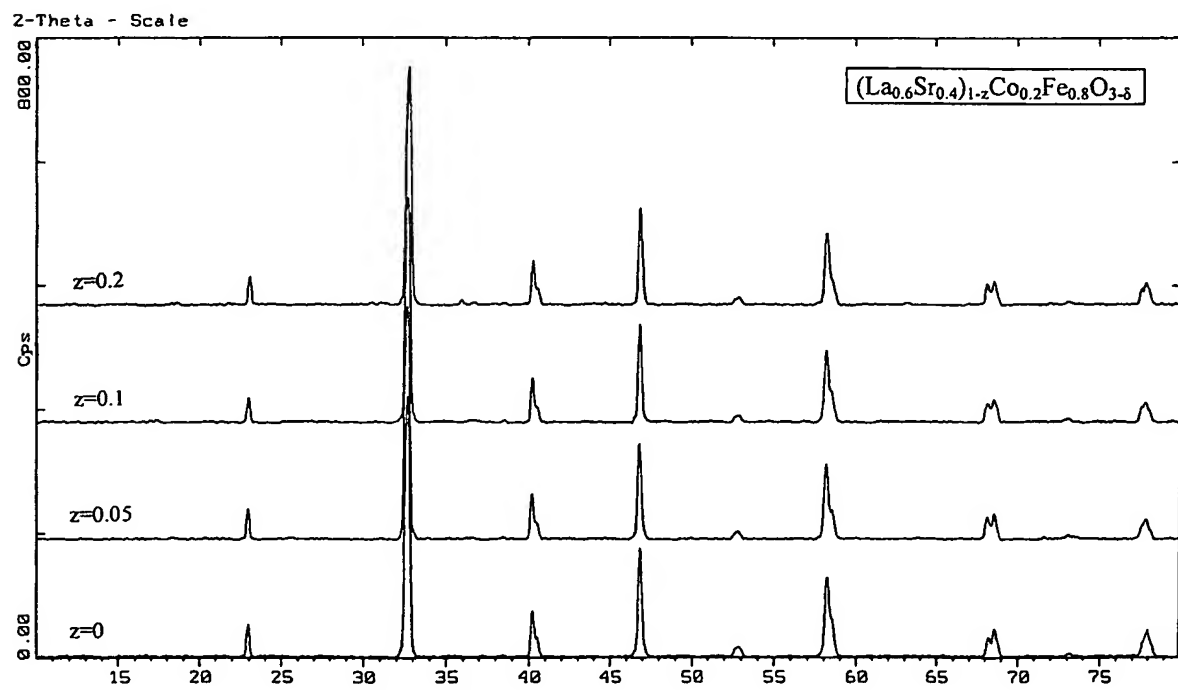
Fig. 2. X-ray diffraction patterns of  $\text{La}_{0.6}\text{Sr}_{0.4-z}\text{Co}_{0.2}\text{Fe}_{0.8}\text{O}_{3-\delta}$ .Fig. 3. X-ray diffraction patterns of  $(\text{La}_{0.6}\text{Sr}_{0.4})_{1-z}\text{Co}_{0.2}\text{Fe}_{0.8}\text{O}_{3-\delta}$ .

Table 1

Composition and crystallographic data for A-site-deficient  $\text{La}_{0.6}\text{Sr}_{0.4}\text{Co}_{0.2}\text{Fe}_{0.8}\text{O}_{3-\delta}$ -based perovskites

Composition	System	$a$ (Å)	$c$ (Å)	$V$ (Å <sup>3</sup> )	$a'$ (Å)
$\text{La}_{0.6}\text{Sr}_{0.4}\text{Co}_{0.2}\text{Fe}_{0.8}\text{O}_{3-\delta}$	Rhombohedral <sup>a</sup>	5.4919	13.364	349.1	3.8748
$\text{La}_{0.6-z}\text{Sr}_{0.4}\text{Co}_{0.2}\text{Fe}_{0.8}\text{O}_{3-\delta}$	Rhombohedral <sup>a</sup>	5.4879	13.384	349.1	3.8748
$z=0.05$	Rhombohedral <sup>a</sup>	5.4908	13.361	348.9	3.8740
$z=0.1$	Rhombohedral <sup>a</sup>	5.4938	13.398	350.2	3.8790
$\text{La}_{0.6}\text{Sr}_{0.4-z}\text{Co}_{0.2}\text{Fe}_{0.8}\text{O}_{3-\delta}$	Rhombohedral <sup>a</sup>	5.5019	13.376	350.7	3.8807
$z=0.05$	Rhombohedral <sup>a</sup>	5.5104	13.375	351.7	3.8846
$z=0.1$	Rhombohedral <sup>a</sup>	5.5043	13.512	354.5	3.8949
$(\text{La}_{0.6}\text{Sr}_{0.4})_{1-z}\text{Co}_{0.2}\text{Fe}_{0.8}\text{O}_{3-\delta}$	Rhombohedral <sup>a</sup>	5.5002	13.382	350.6	3.8805
$z=0.05$	Rhombohedral <sup>a</sup>	5.5062	13.370	351.0	3.8821
$z=0.2$	Rhombohedral <sup>a</sup>	5.4998	13.378	350.5	3.8799

<sup>a</sup> Hexagonal lattice parameters.<sup>b</sup> Pseudo-cubic lattice constant (cube root of unit cell volume per  $\text{ABO}_3$  unit).

### 3. Results and discussion

#### 3.1. Structural study

The XRD patterns of the oxides in the systems  $\text{La}_{0.6-z}\text{Sr}_{0.4}\text{Co}_{0.2}\text{Fe}_{0.8}\text{O}_{3-\delta}$ ,  $\text{La}_{0.6}\text{Sr}_{0.4-z}\text{Co}_{0.2}\text{Fe}_{0.8}\text{O}_{3-\delta}$  and  $(\text{La}_{0.6}\text{Sr}_{0.4})_{1-z}\text{Co}_{0.2}\text{Fe}_{0.8}\text{O}_{3-\delta}$  are shown in Figs. 1–3, respectively. As can be seen, single-phase materials were synthesized in all cases. The patterns were indexed in the rhombohedral perovskite system. However, in the first two systems, the splitting of the peaks located at  $2\theta \approx 40, 58$  and  $68^\circ$  was reduced as the degree of A-site deficiency increased. This denotes that in the systems  $\text{La}_{0.6-z}\text{Sr}_{0.4}\text{Co}_{0.2}\text{Fe}_{0.8}\text{O}_{3-\delta}$  and  $\text{La}_{0.6}\text{Sr}_{0.4-z}\text{Co}_{0.2}\text{Fe}_{0.8}\text{O}_{3-\delta}$  a higher symmetry was achieved with increasing  $z$ . This observation is consistent with the results of Waller et al. [10], who found that, in the system with Sr deficiency, the structure becomes cubic when the Sr content is reduced to 0.15.

The crystallographic data of all compositions are summarized in Table 1. Hexagonal lattice parameters are shown. The pseudo-cubic lattice parameter,  $a'$ , defined as the cube root of the unit cell volume per  $\text{ABO}_3$  unit, is also shown in Table 1 and also in Fig. 4. As can be seen,  $a'$  increased with increasing A-site deficiency. Among the systems studied with different types of A-site deficiency, the increase of  $a'$

was more significant in the order  $\text{La}_{0.6}\text{Sr}_{0.4-z} > (\text{La}_{0.6}\text{Sr}_{0.4})_{1-z} > \text{La}_{0.6-z}\text{Sr}_{0.4}$ .

#### 3.2. Electrical conductivity

The total electrical conductivity measured by the four-point DC method includes an electronic and an ionic conductivity term, due to the holes and oxygen vacancies present, respectively. However, the ionic conductivity, in this type of oxides, is about two

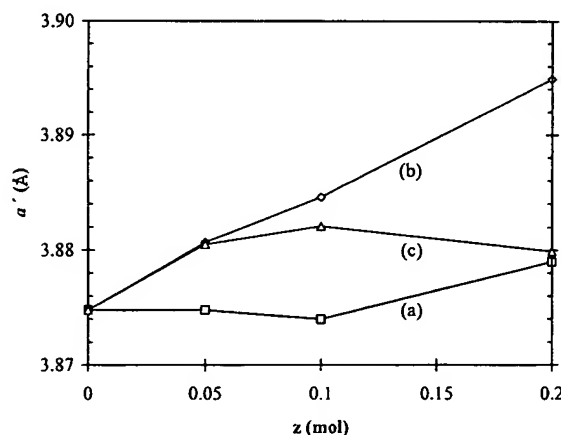


Fig. 4. Pseudo-cubic lattice parameter of (a)  $\text{La}_{0.6-z}\text{Sr}_{0.4}\text{Co}_{0.2}\text{Fe}_{0.8}\text{O}_{3-\delta}$ , (b)  $\text{La}_{0.6}\text{Sr}_{0.4-z}\text{Co}_{0.2}\text{Fe}_{0.8}\text{O}_{3-\delta}$  and (c)  $(\text{La}_{0.6}\text{Sr}_{0.4})_{1-z}\text{Co}_{0.2}\text{Fe}_{0.8}\text{O}_{3-\delta}$  as a function of A-site deficiency ( $z$ ).

orders of magnitude lower than the electronic conductivity and it can be assumed that the measured values refer to the electronic conductivity alone [11].

The logarithm of electrical conductivity versus reciprocal temperature of the oxides in the systems  $\text{La}_{0.6-z}\text{Sr}_{0.4}\text{Co}_{0.2}\text{Fe}_{0.8}\text{O}_{3-\delta}$ ,  $\text{La}_{0.6}\text{Sr}_{0.4-z}\text{Co}_{0.2}\text{Fe}_{0.8}\text{O}_{3-\delta}$  and  $(\text{La}_{0.6}\text{Sr}_{0.4})_{1-z}\text{Co}_{0.2}\text{Fe}_{0.8}\text{O}_{3-\delta}$  are shown in Figs. 5–7, respectively. The electrical conductivity of all compounds increased with temperature up to about 600°C. At higher temperatures a steep con-

ductivity decrease was observed. The conductivity decrease above 600°C is attributed to the loss of lattice oxygen and it is in agreement with the thermal expansion measurements, discussed in the next section.

The electrical conductivity decreased as  $z$  increased for all three series of oxides. This means that the charge compensation mechanism in these A-site-deficient perovskite oxides is probably not the oxidation of  $\text{B}^{3+}$  cations to the tetravalent state, but rather

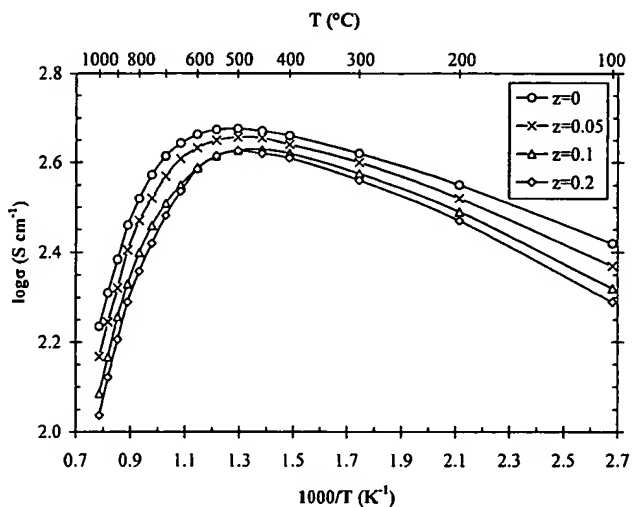


Fig. 5. Logarithm of electrical conductivity versus reciprocal temperature for  $\text{La}_{0.6-z}\text{Sr}_{0.4}\text{Co}_{0.2}\text{Fe}_{0.8}\text{O}_{3-\delta}$  in air.

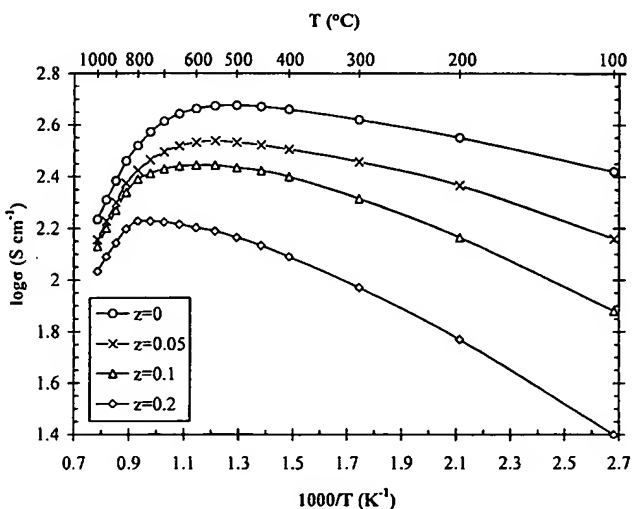


Fig. 6. Logarithm of electrical conductivity versus reciprocal temperature for  $\text{La}_{0.6}\text{Sr}_{0.4-z}\text{Co}_{0.2}\text{Fe}_{0.8}\text{O}_{3-\delta}$  in air.

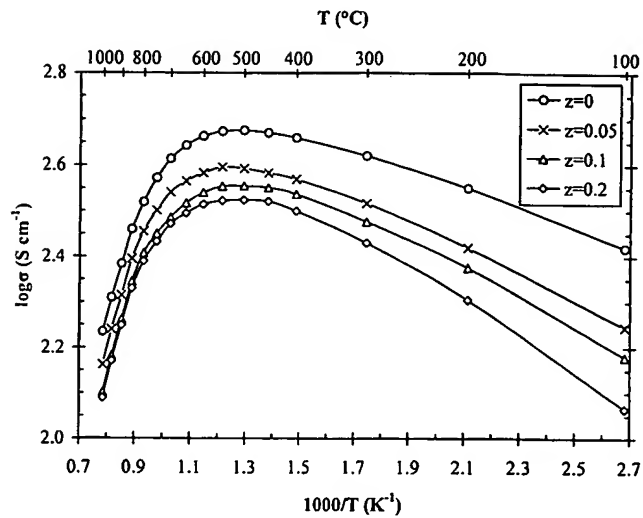


Fig. 7. Logarithm of electrical conductivity versus reciprocal temperature for  $(La_{0.6}Sr_{0.4})_{1-z}Co_{0.2}Fe_{0.8}O_{3-z}$  in air.

the formation of oxygen vacancies. A decrease of the areal resistance of electrodes prepared from A-site-deficient perovskites has been reported [12], and it was also attributed to the preferential formation of oxygen vacancies.

Fig. 8 shows the conductivity at 700°C vs. A-site deficiency. The conductivity decrease was more

intense in the order  $La_{0.6}Sr_{0.4-z} > (La_{0.6}Sr_{0.4})_{1-z} > La_{0.6-z}Sr_{0.4}$ . However, the conductivity values lay at acceptable levels for all oxides, considering the requirements for application in SOFC cathodes [13].

The electronic conductivity of the oxides of this study can be described by the small polaron hopping conductivity model [14]. The charge transfer is thermally activated and its temperature dependence is given by the equation:

$$\sigma = \frac{A}{T} \exp(-E_a/kT) \quad (1)$$

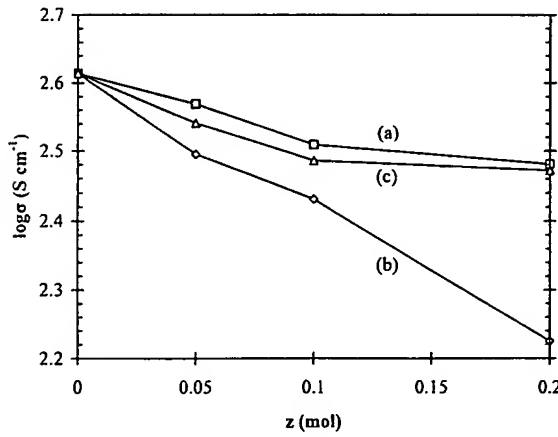


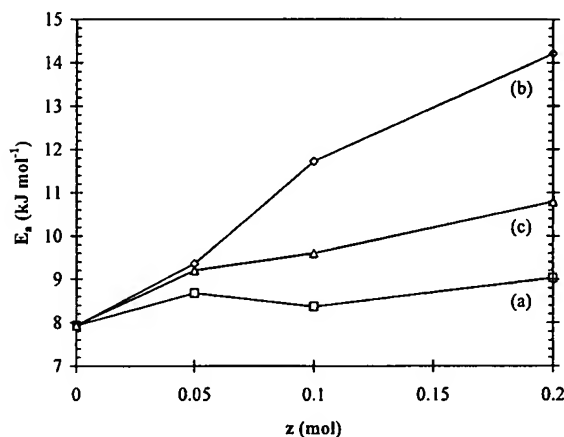
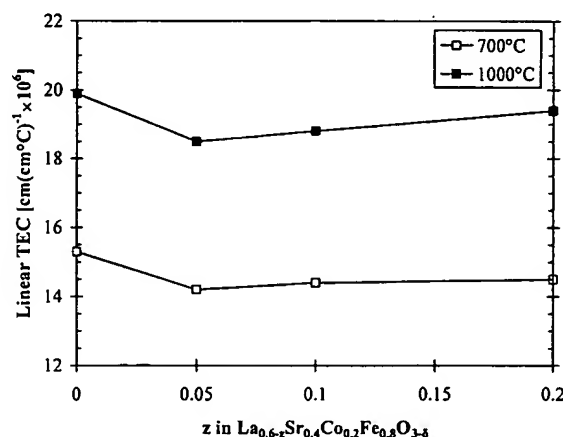
Fig. 8. Electrical conductivity at 700°C for (a)  $La_{0.6-z}Sr_{0.4}Co_{0.2}Fe_{0.8}O_{3-z}$ , (b)  $La_{0.6}Sr_{0.4-z}Co_{0.2}Fe_{0.8}O_{3-z}$  and (c)  $(La_{0.6}Sr_{0.4})_{1-z}Co_{0.2}Fe_{0.8}O_{3-z}$  as a function of A-site deficiency (z).

where  $E_a$  is the activation energy for hopping. Plots of  $\log \sigma T$  versus  $1/T$  were constructed for the temperature ranges where the conductivity increased with temperature. These plots were linear, and from their slopes the activation energies ( $E_a$ ) were calculated. The  $E_a$  values and the temperature ranges at which they are valid are listed in Table 2.  $E_a$  is also drawn in Fig. 9 as a function of  $z$ . As can be seen,  $E_a$  increased as the A-site deficiency increased. The magnitude of the increase of activation energy was more significant in the order  $La_{0.6}Sr_{0.4-z} > (La_{0.6}Sr_{0.4})_{1-z} > La_{0.6-z}Sr_{0.4}$ . By comparing Figs. 8 and 9, it can be concluded that the increase of  $E_a$  follows the same order as the decrease of conductivity.

Table 2

Activation energies for the electrical conductivity of A-site-deficient  $\text{La}_{0.6}\text{Sr}_{0.4}\text{Co}_{0.2}\text{Fe}_{0.8}\text{O}_{3-\delta}$ -based perovskites

Composition	Temperature range (°C)	$E_a$ (kJ mol <sup>-1</sup> )
$\text{La}_{0.6}\text{Sr}_{0.4}\text{Co}_{0.2}\text{Fe}_{0.8}\text{O}_{3-\delta}$	100–500	7.9
$\text{La}_{0.6-z}\text{Sr}_{0.4}\text{Co}_{0.2}\text{Fe}_{0.8}\text{O}_{3-\delta}$		
$z=0.05$	100–500	8.7
$z=0.1$	100–500	8.4
$z=0.2$	100–500	9.0
$\text{La}_{0.6}\text{Sr}_{0.4-z}\text{Co}_{0.2}\text{Fe}_{0.8}\text{O}_{3-\delta}$		
$z=0.05$	100–550	9.4
$z=0.1$	100–600	11.7
$z=0.2$	100–750	14.2
$(\text{La}_{0.6}\text{Sr}_{0.4})_{1-z}\text{Co}_{0.2}\text{Fe}_{0.8}\text{O}_{3-\delta}$		
$z=0.05$	100–500	9.2
$z=0.1$	100–500	9.6
$z=0.2$	100–500	10.8

Fig. 9. Activation energy versus A-site deficiency ( $z$ ) for (a)  $\text{La}_{0.6-z}\text{Sr}_{0.4}\text{Co}_{0.2}\text{Fe}_{0.8}\text{O}_{3-\delta}$ , (b)  $\text{La}_{0.6}\text{Sr}_{0.4-z}\text{Co}_{0.2}\text{Fe}_{0.8}\text{O}_{3-\delta}$  and (c)  $(\text{La}_{0.6}\text{Sr}_{0.4})_{1-z}\text{Co}_{0.2}\text{Fe}_{0.8}\text{O}_{3-\delta}$ .Fig. 10. Linear thermal expansion coefficient of  $\text{La}_{0.6-z}\text{Sr}_{0.4}\text{Co}_{0.2}\text{Fe}_{0.8}\text{O}_{3-\delta}$  at 700 and 1000°C as a function of A-site deficiency ( $z$ ).

### 3.3. Thermal expansion

In Figs. 10–12, the linear thermal expansion coefficient (TEC) for 700 and 1000°C is shown, for the oxides in the systems  $\text{La}_{0.6-z}\text{Sr}_{0.4}\text{Co}_{0.2}\text{Fe}_{0.8}\text{O}_{3-\delta}$ ,  $\text{La}_{0.6}\text{Sr}_{0.4-z}\text{Co}_{0.2}\text{Fe}_{0.8}\text{O}_{3-\delta}$  and  $(\text{La}_{0.6}\text{Sr}_{0.4})_{1-z}\text{Co}_{0.2}\text{Fe}_{0.8}\text{O}_{3-\delta}$ , respectively. The recorded expansion curves were linear, but they became steeper at high temperatures, as a result of

the loss of lattice oxygen and the formation of oxygen vacancies [15]. Thus, the TEC values of Figs. 10–12 were always higher at 1000 than at 700°C.

A comparative diagram of the TEC values of the three systems at 700°C is given in Fig. 13. The TEC of the oxides in the system  $\text{La}_{0.6-z}\text{Sr}_{0.4}\text{Co}_{0.2}\text{Fe}_{0.8}\text{O}_{3-\delta}$  decreased for  $z=0.05$ , and then increased slightly with increasing  $z$ . In the system  $\text{La}_{0.6}\text{Sr}_{0.4-z}\text{Co}_{0.2}\text{Fe}_{0.8}\text{O}_{3-\delta}$ , the TEC de-

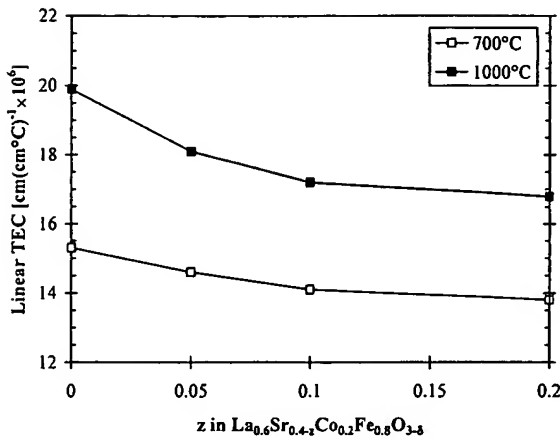


Fig. 11. Linear thermal expansion coefficient of  $\text{La}_{0.6}\text{Sr}_{0.4-z}\text{Co}_{0.2}\text{Fe}_{0.8}\text{O}_{3-\delta}$  at 700 and 1000°C as a function of A-site deficiency ( $z$ ).

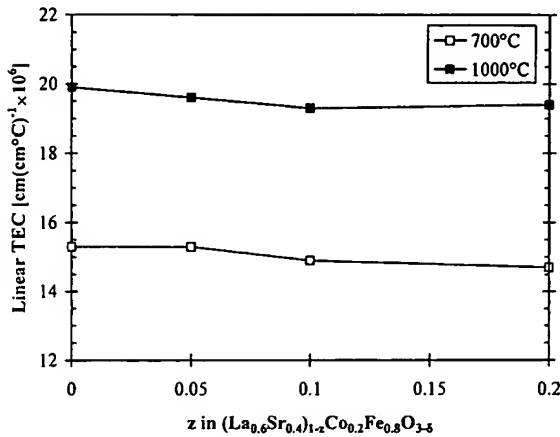


Fig. 12. Linear thermal expansion coefficient of  $(\text{La}_{0.6}\text{Sr}_{0.4})_{1-z}\text{Co}_{0.2}\text{Fe}_{0.8}\text{O}_{3-\delta}$  at 700 and 1000°C as a function of A-site deficiency ( $z$ ).

creased significantly as  $z$  increased. For  $(\text{La}_{0.6}\text{Sr}_{0.4})_{1-z}\text{Co}_{0.2}\text{Fe}_{0.8}\text{O}_{3-\delta}$ , the TEC exhibited a small decrease above  $z=0.05$ .

The compositions with the lowest TEC values were  $\text{La}_{1-z}\text{Sr}_{0.4}\text{Co}_{0.2}\text{Fe}_{0.8}\text{O}_{3-\delta}$ , with  $z=0.05$ , and  $\text{La}_{0.6}\text{Sr}_{0.4-z}\text{Co}_{0.2}\text{Fe}_{0.8}\text{O}_{3-\delta}$ , with  $z=0.1$  and 0.2. Their TEC values at 700°C were  $14.2$ ,  $14.1$  and  $13.8 \times 10^{-6} \text{ cm (cm}^\circ\text{C})^{-1}$ , respectively. These values are considered compatible with the TEC of CGO solid electrolyte [ $12.5 \times 10^{-6} \text{ cm (cm}^\circ\text{C})^{-1}$ ], since they are within the required  $\pm 20\%$  range.

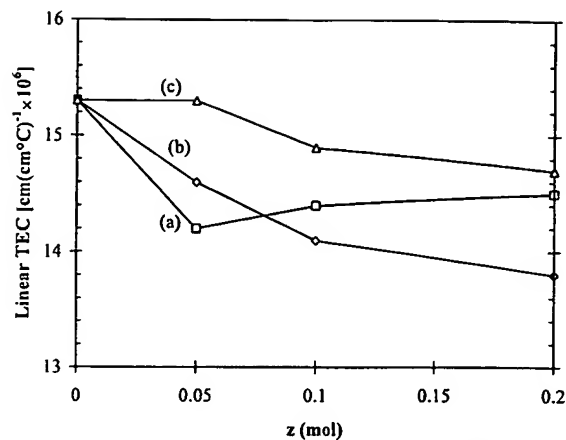


Fig. 13. Linear thermal expansion coefficient at 700°C for (a)  $\text{La}_{0.6}\text{Sr}_{0.4}\text{Co}_{0.2}\text{Fe}_{0.8}\text{O}_{3-\delta}$ , (b)  $\text{La}_{0.6}\text{Sr}_{0.4-z}\text{Co}_{0.2}\text{Fe}_{0.8}\text{O}_{3-\delta}$  and (c)  $(\text{La}_{0.6}\text{Sr}_{0.4})_{1-z}\text{Co}_{0.2}\text{Fe}_{0.8}\text{O}_{3-\delta}$  as a function of A-site deficiency ( $z$ ).

#### 4. Conclusions

A-site-deficient  $\text{La}_{0.6}\text{Sr}_{0.4}\text{Co}_{0.2}\text{Fe}_{0.8}\text{O}_{3-\delta}$ -based oxides of compositions  $\text{La}_{0.6-z}\text{Sr}_{0.4}\text{Co}_{0.2}\text{Fe}_{0.8}\text{O}_{3-\delta}$ ,  $\text{La}_{0.6}\text{Sr}_{0.4-z}\text{Co}_{0.2}\text{Fe}_{0.8}\text{O}_{3-\delta}$  and  $(\text{La}_{0.6}\text{Sr}_{0.4})_{1-z}\text{Co}_{0.2}\text{Fe}_{0.8}\text{O}_{3-\delta}$  ( $0 \leq z \leq 0.2$ ) had a rhombohedral perovskite structure. However, a higher symmetry was achieved when the degree of A-site deficiency increased. The pseudo-cubic lattice parameter increased with increasing  $z$ . The increase was more significant in the order  $\text{La}_{0.6}\text{Sr}_{0.4-z} > (\text{La}_{0.6}\text{Sr}_{0.4})_{1-z} > \text{La}_{0.6-z}\text{Sr}_{0.4}$ .

The electrical conductivity increased with temperature up to about 600°C, and then decreased due to the loss of lattice oxygen. The charge compensation mechanism in these A-site-deficient perovskites is the formation of oxygen vacancies rather than the oxidation  $\text{B}^{3+} \rightarrow \text{B}^{4+}$ . The conductivity decrease and the activation energy increase became more significant in the order  $\text{La}_{0.6}\text{Sr}_{0.4-z} > (\text{La}_{0.6}\text{Sr}_{0.4})_{1-z} > \text{La}_{0.6-z}\text{Sr}_{0.4}$ . For all oxides, the conductivity values at 700°C were at an acceptable level for application in SOFC cathodes.

The TEC was generally lower in the A-site-deficient oxides. The lowest TEC values at 700°C were  $14.2$ ,  $14.1$  and  $13.8 \times 10^{-6} \text{ cm (cm}^\circ\text{C})^{-1}$  for  $\text{La}_{1-z}\text{Sr}_{0.4}\text{Co}_{0.2}\text{Fe}_{0.8}\text{O}_{3-\delta}$ , with  $z=0.05$ , and  $\text{La}_{0.6}\text{Sr}_{0.4-z}\text{Co}_{0.2}\text{Fe}_{0.8}\text{O}_{3-\delta}$ , with  $z=0.1$  and 0.2, respectively.

## References

- [1] L.-W. Tai, M.M. Nasrallah, H.U. Anderson, D.M. Sparlin, S.R. Sehlin, *Solid State Ionics* 76 (1995) 273.
- [2] J.W. Stevenson, T.R. Armstrong, R.D. Carneim, L.R. Pederson, W.J. Weber, *J. Electrochem. Soc.* 143 (1996) 2722.
- [3] B.C.H. Steele, *J. Power Sources* 49 (1994) 1.
- [4] F.P.F. van Berkel, G.M. Christie, F.H. van Heuveln, J.P.P. Huijsmans, in: M. Dokya, O. Yamamoto, H. Tagawa, S.C. Singhal (Eds.), *Proc. 4th Int. Symp. SOFC's*, vol. 95-1, The Electrochem. Soc., 1995, p. 1062.
- [5] M. Sahibzada, B.C.H. Steele, K. Zheng, R.A. Rudkin, J.M. Bae, N. Kiratzis, D. Waller, I.S. Metcalfe, in: B. Thorstnsen, U. Bossel (Eds.), *Proc. of the 2nd European Solid Oxide Fuel Cell Forum*, Switzerland, 1996, p. 687.
- [6] B.C.H. Steele, K. Zheng, R.A. Rudkin, N. Kiratzis, M. Christie, in: M. Dokya, O. Yamamoto, H. Tagawa, S.C. Singhal (Eds.), *Proc. 4th Intern. Symp. SOFC's*, vol. 95-1, The Electrochem. Soc., 1995, p. 1028.
- [7] B.C.H. Steele, *Solid State Ionics* 75 (1995) 157.
- [8] D.H.A. Blank, H. Kruidhof, J. Flokstra, *J. Phys. D* 21 (1988) 226.
- [9] G.Ch. Kostogloudis, N. Vasilakos, Ch. Ftikos, *J. Eur. Ceram. Soc.* 17 (1997) 1513.
- [10] D. Waller, J.A. Lane, J.A. Kilner, B.C.H. Steele, *Solid State Ionics* 27 (1996) 225.
- [11] S. Carter, A. Selcuk, R.J. Chater, J. Kajda, J.A. Kilner, B.C.H. Steele, *Solid State Ionics* 53–56 (1992) 597.
- [12] D. Waller, J.A. Lane, J.A. Kilner, B.C.H. Steele, *Solid State Ionics* 86–88 (1996) 767.
- [13] A. Hammou, in: H. Gerischer, C.W. Tobias (Eds.), *Advances in Electrochemical Science and Engineering*, Vol. vol. 2, VCH, Weinheim, 1992, p. 87.
- [14] P.A. Cox, in: *The Electronic Structure and Chemistry of Solids*, Oxford University Press, Oxford, 1987.
- [15] L.-W. Tai, M.M. Nasrallah, H.U. Anderson, D.M. Sparlin, S.R. Sehlin, *Solid State Ionics* 76 (1995) 259.

## Development of Solid-Oxide Fuel Cells That Operate at 500°C

Rajiv Doshi,<sup>a,\*</sup> Von L. Richards,<sup>b</sup> J. D. Carter,<sup>a</sup> Xiaoping Wang,<sup>a,\*\*</sup> and Michael Krumpelt<sup>a,\*</sup>

<sup>a</sup>Electrochemical Technology Program, Argonne National Laboratory, Argonne, Illinois 60439, USA

<sup>b</sup>Department of Mechanical and Aerospace Engineering, Tri-State University, Angola, Indiana, USA

Solid-oxide fuel cells based on doped ceria electrolytes and operating at 500°C are shown to be feasible. The operating regime of doped ceria electrolytes is discussed. It is shown that the ionic conductivity of ceria-based fuel cells is sufficiently high for operation with hydrogen fuel at low temperatures. The major challenges of fabricating a thin electrolyte by a conventional method and the development of high-performance cathodes capable of operating at 500–600°C are addressed. Cells based on thin-film ceria electrolytes also exhibited good open-circuit voltages between 0.97 and 1 V. Cathode materials with high performance have been developed from pyrochlores, perovskites, and cermets of silver and doped bismuth oxide. The advantages and disadvantages of different cathode materials are discussed. The maximum power density obtained at 500°C was 140 mW/cm<sup>2</sup>.

© 1999 The Electrochemical Society. S0013-4651(98)04-033-6. All rights reserved.

Manuscript submitted April 13, 1998; revised manuscript received December 30, 1998.

Fuel cells are a leading candidate to replace internal combustion engines in vehicles. The combination of fuel cells with batteries as a prime power source in transportation may be a solution to the challenge of providing low or zero emission technology while increasing system efficiency.

The preferred fuel cell technology for transportation applications is the polymer-electrolyte type. It offers high power density and ambient-temperature startup but is very sensitive to carbon monoxide poisoning. In contrast, solid-oxide fuel cells (SOFCs) are not adversely affected by CO. However, the relatively high operating temperature (800–1000°C) of current designs would require more time and energy for startup. By reducing the operating temperature to 500°C, these problems become manageable.

This paper presents approaches to overcoming the problems associated with reducing the operating temperature of SOFCs, mainly, of electrolyte conductivity and cathode polarization. Using the outlined approaches, good fuel cell performance at temperatures as low as 500°C is obtained and potential ways of increasing it further are outlined.

For significantly reduced operating temperatures (500°C), electrolytes with higher ionic conductivity than yttria-stabilized zirconia (YSZ) are needed. This need has led to the development of lanthanum gallate electrolytes by Feng and Goodenough<sup>1</sup> and Ishihara et al.,<sup>2</sup> and to a reevaluation of doped ceria by Steele,<sup>3</sup> and Argonne National Laboratory (ANL).<sup>4</sup> Calculations by Steele and subsequent conductivity measurements at ANL of doped ceria in air and hydrogen show that it becomes an ionic conductor at low temperatures. Figure 1 shows the total conductivity measured by a four-probe method on  $\text{Ce}_{0.8}\text{Gd}_{0.2}\text{O}_{1.9}$  (CGO) in air and in humidified 6% H<sub>2</sub>. The ionic conductivity of YSZ is shown for comparison. At high temperature (800–1000°C) in a hydrogen atmosphere, the conductivity of CGO is significantly higher than in air, indicating mixed ionic and electronic conductivity. As the temperature is reduced, however, it becomes a predominantly ionic conductor even in a reducing environment, as evidenced by the two intersecting lines in Fig. 1. At 450°C the lines merge, showing that the total conductivity below 450°C is purely ionic in the fuel atmosphere. Above 450°C the ionic domain of CGO is a function of the operating conditions of the cell. In a fuel cell, the presence of mixed conductivity is abated because the cathode side of the fuel cell is at a higher oxygen partial pressure than the fuel side. However, when mixed conductivity is present, any electronic leakage current increases as the electrolyte thickness is decreased.<sup>5</sup>

To reduce the operating temperature of SOFCs from 800 to 500°C, two major problems must be solved: (i) reduction of the high

ohmic resistance without decreasing electrolyte thickness below 5 μm and (ii) development of high-performance cathodes compatible with the electrolyte material. CGO satisfies the first requirement at 500°C. This is illustrated by the right axis in Fig. 1. The electrolyte thickness was calculated assuming a minimum performance requirement of 0.2 Ω cm<sup>2</sup> for the electrolyte. From the figure, at a temperature of 500°C the thickness of CGO required is about 10 μm.

The second problem is the rapid increase in cathode polarization at the low operating temperatures. For instance, a single-phase  $\text{La}_{0.9}\text{Sr}_{0.1}\text{MnO}_3$  (LSM) cathode exhibits a cathodic polarization resistance ( $R_c$ ) of less than 1 Ω cm<sup>2</sup> at 1000°C, but it increases to above 2000 Ω cm<sup>2</sup> at 500°C. The cathodic overpotential due to this  $R_c$  is about 500 mV at a current density less than 0.2 mA/cm<sup>2</sup>. Significantly better cathode materials and microstructures are required for low-temperature operation.

Considerable improvements in cathode and fuel-cell performance have been engineered in YSZ-based SOFCs by several research groups, including Virkar et al.,<sup>6</sup> Visco et al.,<sup>7</sup> Minh et al.,<sup>8</sup> and Barnett and Tsai.<sup>9</sup> These have been accomplished together with a reduction in operating temperature from 800 to 600°C by use of dual-phase LSM-YSZ cathodes, by improving the cathode microstructure,<sup>6–8</sup> and by reducing the thickness of the YSZ electrolyte. Barnett and Tsai

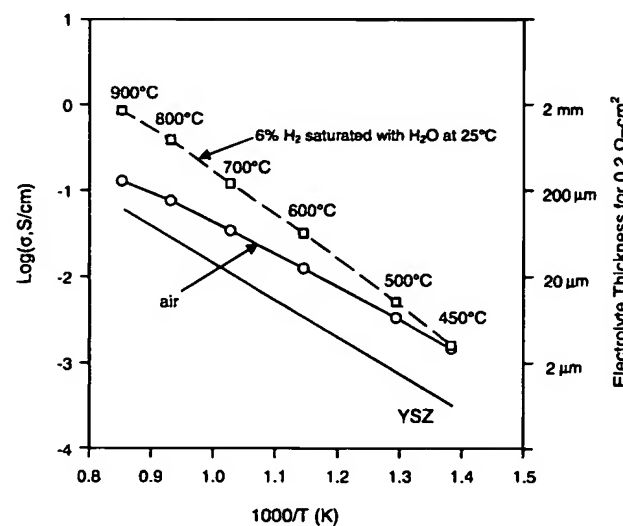


Figure 1. Conductivity ( $\sigma$ ) of  $\text{Ce}_{0.8}\text{Gd}_{0.2}\text{O}_{1.9}$  in air and humidified 6% H<sub>2</sub>. The required electrolyte thickness to achieve an area-specific resistance of 0.2 Ω cm<sup>2</sup> is plotted and values for YSZ shown for comparison.

\* Electrochemical Society Active Member.

\*\* Electrochemical Society Student Member.

further reduced the YSZ thickness from 10 to 1  $\mu\text{m}$  by developing a YSZ + ceria two-layer composite.<sup>9</sup>

Improvements in the LSM + YSZ cathode have been remarkable considering the low oxide ion diffusion in LSM (Fig. 2). It is several orders of magnitude lower than YSZ and some other perovskite oxides.<sup>10,11</sup> However, the surface exchange coefficient for LSM is only one order of magnitude lower than the other perovskites, such as  $\text{La}_{0.6}\text{Ca}_{0.4}\text{Fe}_{0.8}\text{Co}_{0.2}\text{O}_3$  (Fig. 3).<sup>12,13</sup> In fact, the activation enthalpy for bulk diffusion in  $\text{La}_{0.8}\text{Sr}_{0.2}\text{MnO}_{3-\delta}$  is 301 kJ/mol, compared to an activation enthalpy of 139 kJ/mol for surface exchange.<sup>14</sup>

Dual-phase LSM-YSZ cathodes have provided the relatively high effective oxygen fluxes required due to a combination of the high surface exchange in the LSM component and superior oxygen diffusivities in the YSZ component. In addition, the cathode microstructure has been improved by optimizing the connectivity and size distribution between particles of each solid phase to yield a larger three-phase (cathode-electrolyte-gas) contact area that is accessible for oxygen reduction. These improvements have been so large that further improvements are likely to be incremental.

The limitation in performance is now the thickness of the YSZ electrolyte layer. Currently the electrolyte thickness employed is about 10  $\mu\text{m}$ . Further reductions in electrolyte thickness are likely to lead to reliability problems with electrolyte integrity. Therefore, significant improvements in fuel-cell performance require the applica-

tion of higher conductivity electrolytes and higher performance electrodes to SOFCs.

This paper describes the development of a thin, supported ceria electrolyte,  $\text{Ce}_{1-x}\text{Gd}_x\text{O}_{2-\delta}$  (CGO) with  $x = 0.1-0.2$ , combined with the development of high performance cathodes and incorporating both developments to fabricate and test fuel cells at 500°C with high performance.

## Experimental

**Powder synthesis and characterization.**—Electrolyte powder for initial conductivity measurements was synthesized by the Pechini method<sup>15</sup> at ANL. Electrolyte powders were also purchased from two sources: Praxair Specialty Ceramics and Rhone-Poulenc Chimie. There was no significant difference in the conductivity or surface areas (33-35  $\text{m}^2/\text{g}$ ) of the two commercial powders.

Perovskite-type cathode materials were made at ANL by the Pechini method and calcined at 800°C for 4 h. Some commercial powders from Praxair Specialty Ceramics were also tested.  $\text{Pb}_2\text{Ru}_2\text{O}_7$ , pyrochlore was made by an ambient-temperature technique. Chloride salts of lead and ruthenium in the desired ratio were titrated by slow dripping into a concentrated KOH solution while stirring at room temperature. The precipitate was oxidized by bubbling an oxygen stream through the solution and precipitating at 80°C. The oxidized precipitate was then filtered and washed until pH 7 to ensure the removal of chloride and potassium ions. 25 mol % yttria-doped bismuth oxide (YDB) was made by the Pechini method followed by repeated steps of calcination, grinding, and pressing into pellets. These steps were repeated three times until single-phase YDB was obtained. The surface area of the final ground powder was measured at 3  $\text{m}^2/\text{g}$ . Silver powder of -325 mesh was obtained from Johnson Matthey. Before fabricating cathodes, all cathode materials were examined by X-ray diffraction to ensure that they were single phase.

**Fabrication of components.**—For cathode screening tests, 1.6 cm diam pellets were fabricated by uniaxial pressing at a load of 1100  $\text{kg}/\text{cm}^2$ . For the fuel-cell tests, self-supported CGO electrolytes of 2.5 cm diameter were made by uniaxial pressing at a load of 1100  $\text{kg}/\text{cm}^2$  with 1.2 mm thickness. Self-supported CGO electrolytes of 250  $\mu\text{m}$  thickness and anode-supported bilayers with electrolyte thickness of 30  $\mu\text{m}$  (total thickness 250  $\mu\text{m}$ ) were made by a proprietary single- and multilayer tape casting process. The pressed electrolyte disks were sintered at 1500°C for 2 h in air, whereas self-supported electrolyte and anode-supported bilayer tapes were sintered at 1450°C for 30 min.

Single-phase cathodes were applied by either slurry painting or screen printing and two-component cathodes by screen printing. The cathode firing temperature was specific to each composition with  $\text{Pb}_2\text{Ru}_2\text{O}_7$ , Ag-YDB compositions, and one (La, Sr) (Co, Fe)  $\text{O}_3$  (LSCF) composition being fired in situ. Anodes of Ni-CGO cermet were made by screen printing on self-supported electrolyte and were fired at 1250°C for 1 h.

**Testing procedure.**—Both cathode screening and fuel-cell tests were performed with four electrodes (one reference electrode each for anode and cathode), except for fuel cells containing the anode-supported thin-film electrolyte wherein only the cathode side had a reference electrode. When thin electrolytes are used, reference electrode arrangements can introduce significant errors in trying to measure absolute electrode resistivities. However, the results can still be used to provide a comparison of cathode resistivities. The electrode arrangement and the setup for the fuel-cell tests are shown in Fig. 4. Platinum current collectors for the electrodes were spring loaded onto each electrode. The only difference between the cathode screening and fuel-cell tests was the cement seal and anode fuel gas used with fuel-cell tests. Initial fuel-cell tests with 1.2 mm thick pressed electrolytes were performed with a direct liquid feed of reagent-grade methanol solution with water (1:1 mole ratio) and then with a feed of hydrogen gas.

Impedance spectroscopy was used to measure ohmic and polarization resistances with the reference electrodes. These measure-

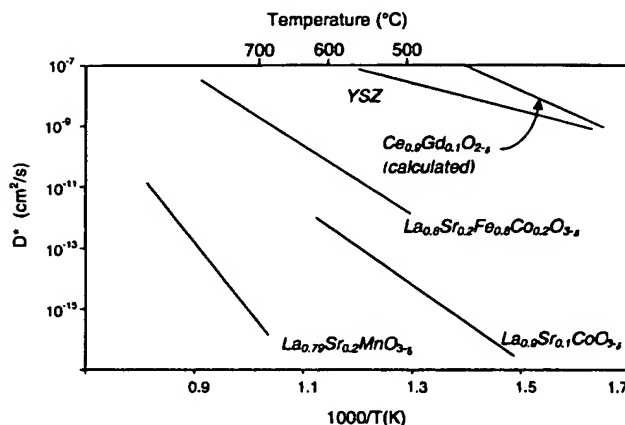


Figure 2. Diffusion coefficient ( $D^*$ ) of various cathode materials compared to a calculated value for CGO ( $\text{La}_{0.79}\text{Sr}_{0.2}\text{MnO}_{3-\delta}$  Ref. 10;  $\text{La}_{0.9}\text{Sr}_{0.1}\text{CoO}_{3-\delta}$  and  $\text{La}_{0.8}\text{Sr}_{0.2}\text{Fe}_{0.8}\text{Co}_{0.2}\text{O}_{3-\delta}$  our data; and YSZ Ref. 11).

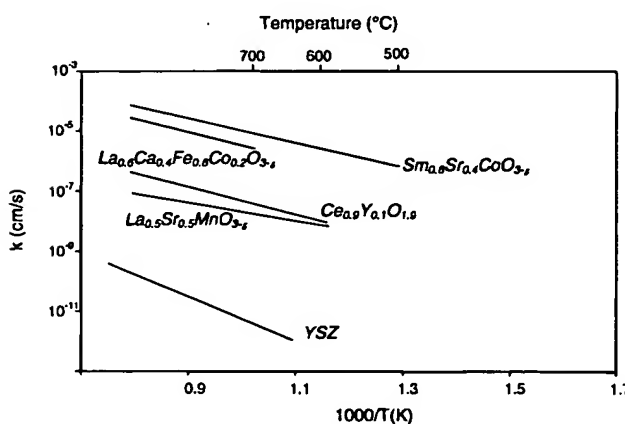


Figure 3. Surface exchange coefficient ( $k$ ) for various materials (YSZ,  $\text{La}_{0.5}\text{Sr}_{0.5}\text{MnO}_{3-\delta}$ ,  $\text{Ce}_{0.9}\text{Y}_{0.1}\text{O}_{1.95}$ , and  $\text{La}_{0.6}\text{Ca}_{0.4}\text{Fe}_{0.8}\text{Co}_{0.2}\text{O}_{3-\delta}$  Ref. 12;  $\text{Sm}_{0.6}\text{Sr}_{0.4}\text{CoO}_{3-\delta}$  Ref. 13).

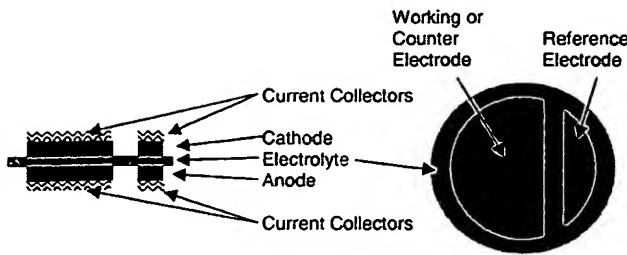


Figure 4. Arrangement of electrodes for cathode and fuel-cell tests using reference electrodes.

ments were performed with working electrodes at open circuit as well as under applied current, and dc polarization was used to measure the resulting overpotential as a function of load.

### Results and Discussion

Initial test results were obtained on SOFCs with 1.2 mm thick electrolytes operating at 500–700°C (Fig. 5). The electrodes were a single phase  $\text{La}_{0.6}\text{Sr}_{0.4}\text{Co}_{0.2}\text{Fe}_{0.8}\text{O}_3$  (LSCF) cathode and a Ni-CGO cermet anode. LSCF has a higher ionic and electronic conductivity than other perovskites except for the pure cobaltites. Its thermal expansion coefficient ( $14 \times 10^{-6} \text{ cm/cm/K}$ ) is also similar to the CGO electrolyte ( $13.5 \times 10^{-6} \text{ cm/cm/K}$ ).

The performance of these fuel cells in methanol was found to be comparable to that in hydrogen at temperatures of 500–700°C (Fig. 5) and has been reported earlier.<sup>16</sup> At 500°C the ohmic drop was high ( $\sim 20 \Omega \text{ cm}^2$ ) through the dense self-supported, thick electrolyte.<sup>16</sup> With thin electrolytes it was thought that the open-circuit voltage (OCV) could be reduced significantly due to increased leakage flux from electronic conductivity. The LSCF cathode exhibited high polarization resistance ( $R_c$ ) as well with a value of  $7 \Omega \text{ cm}^2$  at 500°C.<sup>16</sup> For efficient fuel-cell operation, a value of  $R_c < 1 \Omega \text{ cm}^2$  is desired. As expected at 600 and 700°C, the OCV was low at 0.93 and 0.87 V, respectively, but at 500°C it was 1 V. These results indicated the presence of significant electronic conductivity at 600°C and above and a much smaller electronic conductivity at 500°C, since the measured OCV is less than the theoretical OCV of over 1.1 V. Tests with a thinner electrolyte (250  $\mu\text{m}$ ), Ni-CGO anode, and LSCF cathode

show that this small amount of electronic conductivity decreases further when the cell is loaded. Figure 6 shows a comparison of the expected electrolyte ohmic resistance (calculated from the value at 700°C for air in Fig. 1) and the measured electrolyte ohmic drop as a function of load (current density) with air on one side and humidified hydrogen on the other. At open circuit the measured resistance is midpoint between the electrolyte resistance in air and that in hydrogen. As the load increases the resistance increases and approaches the calculated resistance in air (ionic) for the electrolyte material. This is presumably due to the expansion of the purely ionic region starting at the cathode and extending toward the anode. It is believed to be caused by the infusion of oxide ions that fill vacancies and deplete the electrons when the SOFC is under load.

This is an important result. It shows that doped ceria electrolyte is better than previous knowledge would indicate. It is essentially an ionic conductor when a ceria-based SOFC is operated under load at high current densities, even at 700°C. The electronic conductivity causes leakage current only when the cell is operated at open circuit or at low current densities at temperatures above 500°C.

**Cathodes.**—Whereas the ohmic resistance can be decreased to less than  $1 \Omega \text{ cm}^2$  by fabricating a thin film electrolyte, the cathode polarization resistance requires the development of new materials or microstructures with high performance at 500°C. In the case of LSM, the low ionic conductivity is the main contributor to high polarization resistance when it is used as a porous cathode on the CGO electrolyte (Fig. 7). New materials with higher ionic and electronic conductivities were therefore developed and tried. They include pyrochlores, two-phase materials consisting of Ag and Y<sub>2</sub>O<sub>3</sub>, and perovskite-type oxides.

**Pyrochlores.**—A  $\text{Pb}_2\text{Ru}_2\text{O}_7$  pyrochlore made by an ambient-temperature precipitation method exhibited high polarization resistance ( $6 \Omega \text{ cm}^2$ ) initially, but upon application of load, its  $R_c$  decreased to  $0.6 \Omega \text{ cm}^2$ . The performance was promising under load but the material was found to be unstable when the total cathode overpotential exceeded 250 mV. It is believed to decompose into molten lead and ruthenium or ruthenium oxide at 500°C. Lead was found to penetrate the electrolyte either through the pores (less than 5%) or through grain boundaries and carry the ruthenium phase along with it, possibly suggesting the formation of molten lead. This was evidenced by scanning electron microscopy (SEM) observation

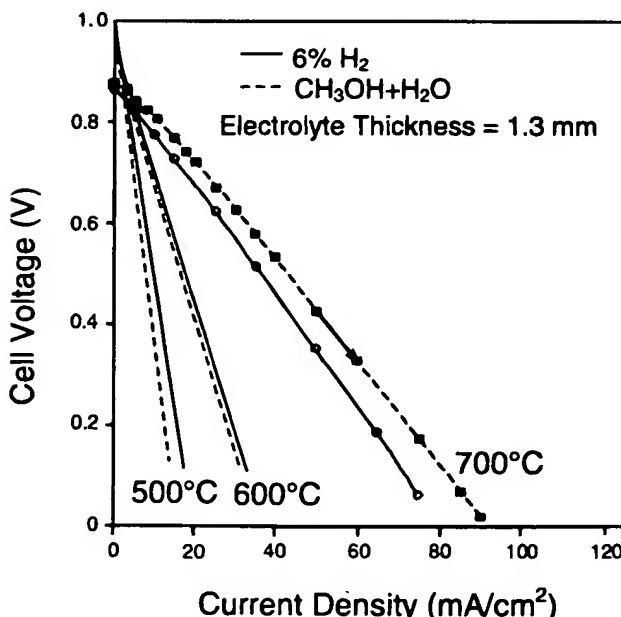


Figure 5. Initial fuel-cell performance with a LSCF cathode and a Ni-ceria anode in methanol and hydrogen.

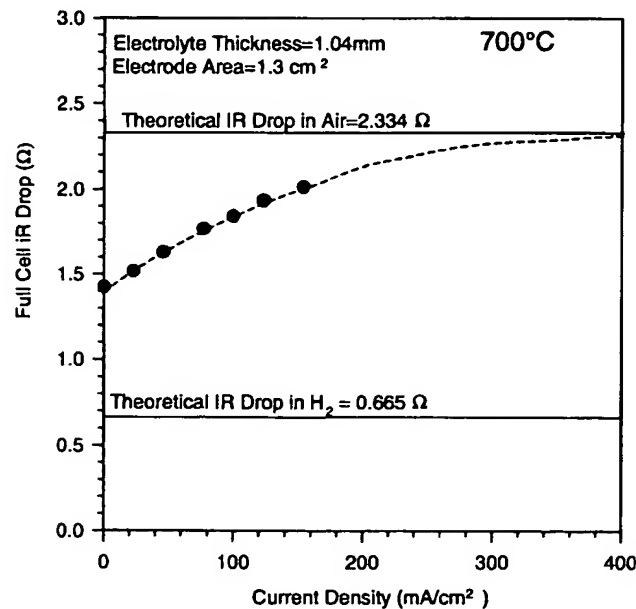


Figure 6. The electrolyte resistance in a fuel-cell operating at 700°C on air/hydrogen as a function of current density.

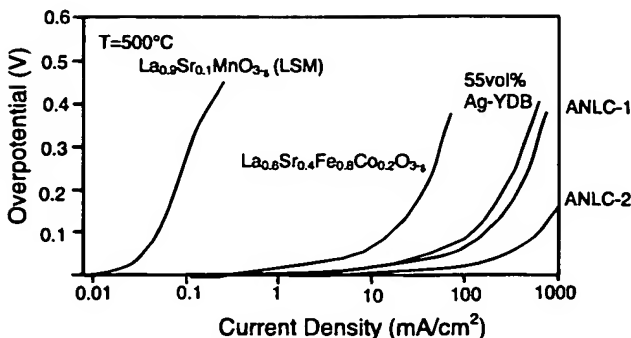


Figure 7. Overpotential of cathode materials at 500°C in air determined by cathode-screening tests.

of lead deposits of about 100  $\mu\text{m}$  in the electrolyte and by a decrease in the measured ohmic resistance of the electrolyte. Similar to the lead ruthenate,  $\text{Bi}_2\text{Ru}_2\text{O}_7$  could be another candidate for the cathode. However, both materials are unlikely to be stable when the polarization on the cathode exceeds 200 mV based on the free energy of formation of lead and bismuth oxides.

**Ag-YDB.**—A range of two-phase cathode microstructures with high performance at 500–600°C were developed. These consisted of different ratios of a YDB for ionic conduction and silver, an electrocatalyst, and an electronic conductor. The cathodes were applied in the form of screen printing inks to the electrolyte and fired *in situ* during cell tests. The cathodes were sintered at 750–800°C and then cooled to the operating temperature of 500–600°C for measurements. At a firing temperature of 800°C, there was about a 10  $\mu\text{m}$  interaction layer between the electrolyte and the YDB in the cathode. The interaction layer could be reduced by decreasing the firing temperature to 750°C with some loss in performance. These efforts led to the development of new cathodes with  $R_c$  significantly reduced from 7  $\Omega\text{ cm}^2$  for LSCF to less than 1  $\Omega\text{ cm}^2$  with the new materials, depending upon the distribution of the two phases. The polarization resistance for the porous Ag-YDB cathode as a function of vol % Ag was evaluated and found to exhibit a minima between 45 and 55 vol % (Fig. 8). Fuel-cell tests were conducted with several Ag-YDB cathodes. These results are discussed later and compared with fuel cells incorporating other electrode materials.

**Perovskites.**—While initial cathode screening and fuel-cell tests indicated high polarization resistance in LSCF, a more detailed study indicated improved performance with decreasing sintering temperature of the LSCF cathode after it is applied to the electrolyte surface.

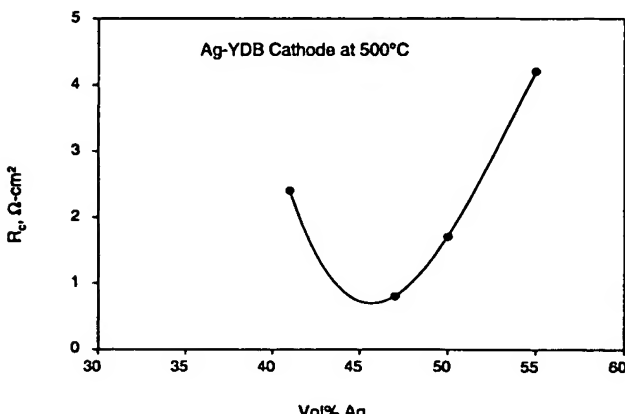


Figure 8. Polarization resistance for the two-phase Ag-YDB porous cathode as a function of silver content.

Such electrodes consistently exhibited high performance initially followed by a gradual increase in  $R_c$  to above 5  $\Omega\text{ cm}^2$ . This was the case both with stoichiometric and A-site deficient materials. One of the best electrode performances to date was obtained with A-site deficient cobalt-ferrite,  $(\text{La}_{0.6}\text{Sr}_{0.4})_{0.95}\text{Fe}_{0.8}\text{Co}_{0.2}\text{O}_{3-\delta}$ , which was applied and tested at 500°C without a separate firing step. This was possible due to a spring-loaded setup that held a platinum current collector screen in place during the test. The initial  $R_c$  was only 0.1  $\Omega\text{ cm}^2$  at 500°C, but with time held at 500°C (24 h) it increased to above 10  $\Omega\text{ cm}^2$ . Post-test X-ray diffraction of the cathode indicated that the  $R_c$  increase was due to the formation of a spinel-phase  $\text{CoFe}_2\text{O}_4$ . For stoichiometric LSCF, formation of a spinel or any other phases over time was not detected yet their  $R_c$  increased with time just as with A-site-deficient LSCF.

It is believed that when unsintered stoichiometric LSCF electrodes with high performance are sintered, the LSCF particles form bridges which decrease the actual contact area between the CGO electrolyte and the cathode. This causes the polarization resistance to increase. The performance of a LSCF cathode would be high if the real area of contact could be maintained high. This condition could be accomplished by depositing a thin, reasonably dense film of LSCF on the electrolyte followed by a thick current-collection layer on top. Steele et al.<sup>17</sup> have deposited a thin, dense LSCF layer (1  $\mu\text{m}$ ) on top of an anode-supported ceria electrolyte (10  $\mu\text{m}$ ) followed by deposition of a porous LSCF layer (30  $\mu\text{m}$ ) for current collection. Both the 10  $\mu\text{m}$  CGO and 1  $\mu\text{m}$  LSCF films were made by electrostatic spray pyrolysis.<sup>18</sup> A second and perhaps better solution for large-scale fabrication is to make a two-component porous cathode of LSCF + CGO that is analogous to the LSM + YSZ electrode for YSZ and similar to Visco's  $(\text{La}, \text{Sr})(\text{Co}, \text{Ni})\text{O}_3$  cathode.<sup>7</sup>

New electrode microstructures were developed to prevent the effect of sintering of electrode particles on performance. The two electrodes shown in Fig. 7 with the new microstructures are ANLC-1 and ANLC-2. Both these electrodes exhibited stable performance with time over several days.

**Fabrication of electrolyte thin films.**—As mentioned earlier, high ohmic drop was evident in earlier fuel-cell tests of Fig. 1 when thick electrolytes were employed. The resistance of the SOFC electrolyte was therefore reduced by fabricating an anode-supported electrolyte bilayer with an electrolyte thickness of 30  $\mu\text{m}$  and anode thickness of about 250  $\mu\text{m}$ . The bilayers were fabricated by a multilayer tape-casting technique. Dried bilayer tapes were cut into 2.5 cm diam disks and fired. Larger samples of 10  $\times$  10 cm were also fabricated to study shrinkage behavior. The organic compositions were matched to cause equal shrinkage between the two layers of the bilayer. The technique was optimized to yield flat bilayer plates of up to 10  $\times$  10 cm size. Figure 9 shows the microstructure of such a

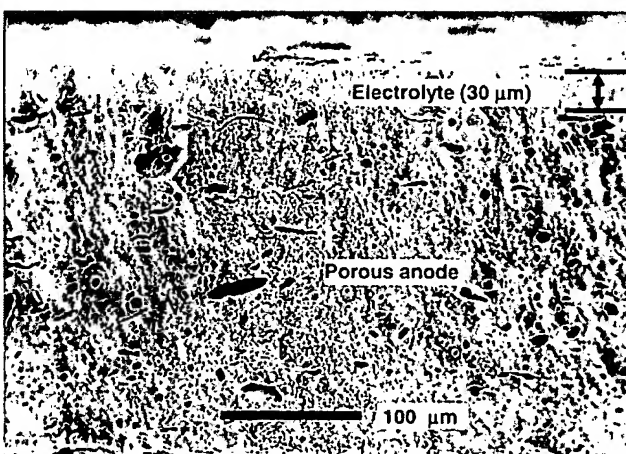


Figure 9. Microstructure of the anode-supported electrolyte bilayer.

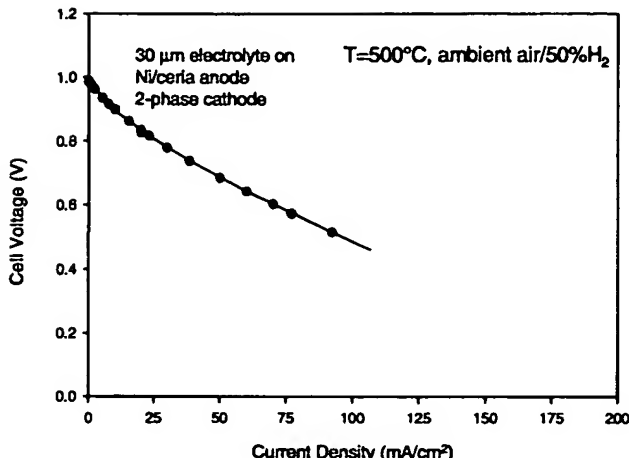


Figure 10. Performance of the SOFC with the anode-supported ceria-based electrolyte and Ag-YDB cathode in 50%  $\text{H}_2$  and air at 500°C.

bilayer with nickel in an oxidized state. The microstructure shows good bonding between the anode and electrolyte layers.

The advantage of using a tape-casting technique for bilayer fabrication is that it is widely used by industry and is more easily scaleable than the slurry-deposition techniques currently used. It also presumably requires less capital equipment than sputtering.

The anode of the bilayer performed with negligible polarization losses. This made it feasible to achieve high performance at 500°C using high-performance cathodes, such as the two-phase cathode or ANLC-1. The incorporation of thin electrolytes caused the ohmic drop through the cells to be reduced to  $0.7 \Omega \text{ cm}^2$ .

**Fuel-cell tests.**—Fuel-cell tests were performed on 2.5 cm diam disks. Figure 10 gives the performance of a fuel cell with an anode/electrolyte bilayer and the two-phase Ag-YDB cathode at 500°C in 50%  $\text{H}_2$  and ambient pressure air. A fuel gas composition of 50%  $\text{H}_2$  (balance He) was chosen to simulate reformate gas from typical hydrocarbon reformers. It was believed that for an electrolyte with some electronic conductivity, the OCV would decrease as a function of thickness due to an increased leakage current and the resulting increased oxygen flux. While this is certainly possible, we did not observe this behavior, as evidenced by an OCV of almost 1 V, which is the same as for the 1.2 mm thick electrolyte from Fig. 5. The overall performance was significantly improved over that in Fig. 5 due to both decreased electrolyte thickness and higher cathode performance.

Figure 11 shows the performance of another cell at 500°C with the ANLC-1 cathode on a bilayer under the same conditions of temperature and reactants. The total cell resistance, including electrode polarization for both electrodes, was  $1.3 \Omega \text{ cm}^2$ :  $0.7 \Omega \text{ cm}^2$  from the electrolyte, nearly  $0.6 \Omega \text{ cm}^2$  from the cathode, and negligible loss coming from the anode. The maximum power density obtained was  $140 \text{ mW/cm}^2$ .

The power density may be improved further upon incorporating ANLC-2. This electrode, which has a different microstructure and is more difficult to fabricate, had an  $R_c$  value (determined from cathode screening tests) of less than  $0.2 \Omega \text{ cm}^2$ . An improvement in electrode resistance from  $0.6$  to  $0.2 \Omega \text{ cm}^2$  combined with a decrease in electrolyte thickness to  $15 \mu\text{m}$  should yield a cell with less than  $0.6 \Omega \text{ cm}^2$  total resistance. This would give a power density of  $300$ – $400 \text{ mW/cm}^2$ , assuming the OCV does not change substantially.

### Conclusions

We have shown that doped ceria is a feasible electrolyte for operation at 500°C with fuels such as liquid methanol or hydrogen-containing gases. Operation at such a low temperature should ease the requirements on both the seals and interconnects for an SOFC stack. New cathode materials and microstructures were found to exhibit

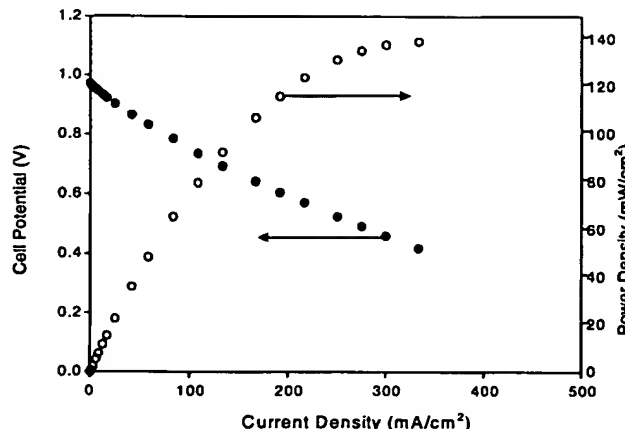


Figure 11. Performance of the SOFC with the anode-supported ceria-based electrolyte and ANLC-1 cathode in 50%  $\text{H}_2$  and air at 500°C.

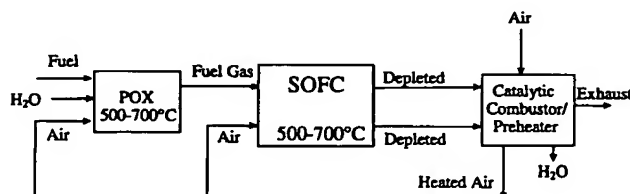


Figure 12. Fuel-cell system with ceria-based SOFC coupled to a partial oxidation reactor both operating between 500 and 700°C.

good performance at low operating temperature. Cathodes made from LSCF have inherently high performance, but the microstructure must be stabilized to achieve a stable area of contact at the electrode/electrolyte interface. Other new cathodes, when combined with a bilayer of a thin-film electrolyte and a thick anode, exhibited good performance at 500°C in 50%  $\text{H}_2$  and air. The maximum power density obtained under these conditions was  $140 \text{ mW/cm}^2$ . Further performance improvements that could increase the power density to  $300 \text{ mW/cm}^2$  are well within reach.

Using this low-temperature SOFC technology, a potentially simple propulsion system can be realized if the 500°C SOFC is operated directly on methanol or coupled to a partial oxidation reformer (POX) for heavier hydrocarbon fuels such as gasoline (Fig. 12). For gasoline-based systems, the advantage is that the operating temperatures for both the fuel cell and reformer are in the same temperature range of 500–700°C. In addition, the reformate gas from the POX can be fed directly to the anode feed of the fuel cell stack without CO reduction.

### Acknowledgment

This work was supported by the Department of Energy's Office of Transportation Technologies for Argonne National Laboratory, managed by the University of Chicago for the U.S. Department of Energy under Contract no. W-31-109-ENG-38.

Argonne National Laboratory assisted in meeting the publication costs of this article.

### References

1. M. Feng and J. B. Goodenough, *Eur. J. Solid State Inorg. Chem.*, **31**, 663 (1994).
2. T. Ishihara, H. Matsuda, and Y. Takita, *J. Am. Ceram. Soc.*, **116**, 3801 (1994).
3. B. C. H. Steele, *J. Power Sources*, **49**, 1 (1994).
4. K. M. Myles, R. Doshi, R. Kumar, and M. Krumpelt, in *Proceedings of the 1st European SOFC Forum*, European Fuel Cell Group, Ltd., pp. 983–992, Lucerne, Switzerland, Oct 3–7 (1994).
5. M. Gödickemeier, D. Schneider, and L. J. Gauckler, in *Proceedings of the Fifth International Symposium on SOFCs*, European Fuel Cell Group, Ltd., p. 1011 Lucerne, Switzerland, Oct 3–7 (1997).

6. A. V. Virkar, J.-W. Kim, and K. Mehta, Fuel Cells '97 Review Meeting, Morgantown, WV, Aug 26-28, 1997.
7. S. J. Visco, C. P. Jacobson, and L. C. De Jonghe, Fuel Cells '97 Review Meeting, Morgantown, WV, Aug 26-28, 1997.
8. N. Q. Minh, B. Chung, and K. Montgomery, Fuel Cells '97 Review Meeting, Morgantown, WV, Aug 26-28, 1997.
9. S. Barnett and T. Tsai, Fuel Cells '97 Review Meeting, Morgantown, WV, Aug 26-28, 1997.
10. A. Belsner, T. Gür, and R. Huggins, *Solid State Ionics*, 57, 327 (1992).
11. H. Inaba and H. Tagawa, *Solid State Ionics*, 83, 1 (1996).
12. B. C. H. Steele, *Solid State Ionics*, 75, 157 (1995).
13. B. C. H. Steele, *Solid State Ionics*, 86-88, 1223 (1996).
14. J. A. Kilner, R. A. De Souza, and I. C. Fullerton, *Solid State Ionics*, 86-88, 703 (1996).
15. M. Pechini, U.S. Pat. 3,330,697 (1967).
16. R. Doshi and M. Krumpelt, Abstract 491, Extended Abstracts, Vol. 95-1, p. 757, The Electrochemical Society, Reno, NV, May 21-26, 1995.
17. M. Sahibzada, R. A. Rudkin, B. C. H. Steele, I. S. Metcalfe, and J. A. Kilner, in *Proceedings of the Fifth International Symposium on SOFCs*, p. 244 (1997).
18. K.-L. Choy, W. Bai, and B. C. H. Steele, in *Proceedings of the Fifth International Symposium on SOFCs*, p. 1177 (1997).



ELSEVIER

Solid State Ionics 89 (1996) 215-220

**SOLID  
STATE  
IONICS**

# Chemical compatibility of the $\text{LaFeO}_3$ base perovskites $(\text{La}_{0.6}\text{Sr}_{0.4})_z\text{Fe}_{0.8}\text{M}_{0.2}\text{O}_{3-\delta}$ ( $z = 1, 0.9$ ; $\text{M} = \text{Cr, Mn, Co, Ni}$ ) with yttria stabilized zirconia

L. Kindermann, D. Das<sup>1</sup>, H. Nickel, K. Hilpert\*

*Institute for Materials in Energy Systems Research Centre Jülich (KFA), 52425 Jülich, Germany*

Received 31 January 1996; accepted 19 February 1996

## Abstract

Physicochemical compatibilities of the series of  $\text{LaFeO}_3$  base perovskites  $\text{La}_{0.6}\text{Sr}_{0.4}\text{Fe}_{0.8}\text{M}_{0.2}\text{O}_{3-\delta}$  and  $(\text{La}_{0.6}\text{Sr}_{0.4})_z\text{Fe}_{0.8}\text{M}_{0.2}\text{O}_{3-\delta}$  ( $\text{M} = \text{Cr, Mn, Co, Ni}$ ) with the solid electrolyte yttria stabilized (8 mol%  $\text{Y}_2\text{O}_3$ ) cubic zirconia, 8YSZ, were investigated. Powder mixtures of the perovskites with 8YSZ were annealed at 1000°C for time periods up to 1300 h. The quenched samples were analyzed by XRD and SEM/EDX for identifying the reaction products. The results provide a working hypothesis for the development of improved compositions of cathode materials in solid oxide fuel cells.

**Keywords:** Solid oxide fuel cell; Yttria stabilized zirconia; Perovskite

## 1. Introduction

Strontium substituted lanthanum ferrites,  $\text{La}_{1-x}\text{Sr}_x\text{FeO}_{3-\delta}$ , are known [1,2] for their good electrical conductivities and electrocatalytic activities useful for application as cathode material in high temperature solid oxide fuel cells (SOFC). However, only little information is available regarding their chemical compatibility with solid electrolytes such as 8YSZ (cubic  $\text{ZrO}_2$  stabilized with 8 mol%  $\text{Y}_2\text{O}_3$ ).

The perovskite with 30% Sr on A-site,  $\text{La}_{0.7}\text{Sr}_{0.3}\text{FeO}_{3-\delta}$ , reacts with 8YSZ at 1100°C forming a strontium zirconate phase [1]. Partial substitution of Fe atoms by Co atoms results in enhancement of the reactivity for the composition  $\text{La}_{0.6}\text{Sr}_{0.4}\text{Fe}_{0.8}\text{Co}_{0.2}\text{O}_{3-\delta}$  [3]. In this work, we report our investigations in establishing the trend of reactivities of 8YSZ with lanthanum strontium ferrites of compositions  $\text{La}_{0.6}\text{Sr}_{0.4}\text{Fe}_{0.8}\text{M}_{0.2}\text{O}_{3-\delta}$  and  $(\text{La}_{0.6}\text{Sr}_{0.4})_z\text{Fe}_{0.8}\text{M}_{0.2}\text{O}_{3-\delta}$  ( $\text{M} = \text{Cr, Mn, Co, Ni}$ ) due to the partial substitution of Fe atoms by other 3d metals and the substoichiometry on A-sites. This work is part of our systematic investigations on the chemical compatibility between 8YSZ and  $\text{LaFeO}_3$ .

\*Corresponding author.

<sup>1</sup>On leave from Bhabha Atomic Research Centre, Bombay 400 085, India.

base perovskites doped with Ca [4] or Sr [5] on A-site and various transition metals on B-site.

## 2. Experimental

Perovskites of the compositions  $\text{La}_{0.6}\text{Sr}_{0.4}\text{Fe}_{0.8}\text{M}_{0.2}\text{O}_{3-\delta}$  and  $(\text{La}_{0.6}\text{Sr}_{0.4})_{0.9}\text{Fe}_{0.8}\text{M}_{0.2}\text{O}_{3-\delta}$  ( $\text{M} = \text{Cr}, \text{Mn}, \text{Co}, \text{Ni}$ ) were prepared and characterized [6] by A/S, Haldor-Topsoe S/A, Copenhagen, Denmark. The results of the characterization of these eight samples are listed in Table 1. All samples were calcined a second time at 900°C for 48 h in our laboratory in order to dissolve the small amounts of additional phases present in some of the as received samples. The calcined samples were again analyzed by XRD and the results are also given in Table 1. Obviously, the calcination process improves to some extent the phase homogeneity. After the calcination, each of the compositions was intimately mixed in an

agate mortar with an equimolar amount of 8YSZ in ethanol. The mixtures were dried in an oven and the resulting finely divided powder mixtures were pressed in small cylindrical pellets (diameter 5 mm, height 0.5 mm). The pellets were then sintered in a furnace at 1000°C under ambient atmosphere. For each sample the pellets were sintered over different time periods (5 min up to 1300 h). The annealed samples were analyzed by XRD using a high speed camera (Stoe diffractometer with monochromatic Co  $\text{K}\alpha_1$  radiation). In addition, for some of the samples SEM/EDX analyzes (Cam Scan Scanning Electron Microscope with Tracor Northern Micro Scan) were carried out to determine the approximate chemical composition of the different phases present therein. The amount of the  $\text{SrZrO}_3$  phase formed in the annealed pellets was estimated from the XRD pattern by the preparation of 8YSZ/ $\text{SrZrO}_3$  powder mixtures. The  $\text{SrZrO}_3$  in these mixtures was supplied by CERAC INC., Milwaukee, USA. The areas of the

Table 1

Phase compositions of the prepared perovskite materials as received from Haldor Topsoe S/A, Denmark, and after additional calcination at 900°C for 48 h. (The results of the as received materials are from Haldor Topsoe S/A)

No.	Perovskite materials	Structure and phase composition (as received)	Structure and phase composition (after additional calcination)
1.	$\text{La}_{0.6}\text{Sr}_{0.4}\text{Fe}_{0.8}\text{Cr}_{0.2}\text{O}_{3-\delta}$	Orthorhombic: $a = 5.525 \text{ \AA}$ $b = 7.924 \text{ \AA}$ $c = 5.514 \text{ \AA}$ Extra phase: <1% unknown phase	Orthorhombic no extra phase
2.	$\text{La}_{0.6}\text{Sr}_{0.4}\text{Fe}_{0.8}\text{Mn}_{0.2}\text{O}_{3-\delta}$	Rhombohedral: $a_h = 5.510 \text{ \AA}$ $c_b = 13.48 \text{ \AA}$ (Pseudocubic: $a = 3.895 \text{ \AA}$ ) Extra phase: very small amounts of unknown phase	Rhombohedral no extra phase
3.	$\text{La}_{0.6}\text{Sr}_{0.4}\text{Fe}_{0.8}\text{Co}_{0.2}\text{O}_{3-\delta}$	Pseudocubic: $a = 3.887 \text{ \AA}$ Extra phase: small amounts of $\text{La}_2\text{CoO}_4$ and $\text{Fe}_3\text{O}_4$	Pseudocubic no extra phase
4.	$\text{La}_{0.6}\text{Sr}_{0.4}\text{Fe}_{0.8}\text{Ni}_{0.2}\text{O}_{3-\delta}$	Pseudocubic: $a = 3.895 \text{ \AA}$ Extra phase: small amounts of $\text{La}_2\text{NiO}_4$ and $\text{Fe}_3\text{O}_4$	Pseudocubic no extra phase
5.	$(\text{La}_{0.6}\text{Sr}_{0.4})_{0.9}\text{Fe}_{0.8}\text{Cr}_{0.2}\text{O}_{3-\delta}$	Pseudocubic: $a = 3.912 \text{ \AA}$ Extra phase: very small amounts of unknown phase	Pseudocubic no extra phase
6.	$(\text{La}_{0.6}\text{Sr}_{0.4})_{0.9}\text{Fe}_{0.8}\text{Mn}_{0.2}\text{O}_{3-\delta}$	Pseudocubic: $a = 3.903 \text{ \AA}$ Extra phase: no extra phase	Pseudocubic no extra phase
7.	$(\text{La}_{0.6}\text{Sr}_{0.4})_{0.9}\text{Fe}_{0.8}\text{Co}_{0.2}\text{O}_{3-\delta}$	Pseudocubic: $a = 3.888 \text{ \AA}$ Extra phase: small amounts of $\text{La}_2\text{CoO}_4$ , very small amounts of $\text{Fe}_3\text{O}_4$	Pseudocubic very small amounts of $\text{La}_2\text{CoO}_4$
8.	$(\text{La}_{0.6}\text{Sr}_{0.4})_{0.9}\text{Fe}_{0.8}\text{Ni}_{0.2}\text{O}_{3-\delta}$	Pseudocubic: $a = 3.893 \text{ \AA}$ Extra phase: small amounts of $\text{NiO}$ , very small amounts of $\text{Fe}_3\text{O}_4$	Pseudocubic very small amounts of $\text{Fe}_3\text{O}_4$

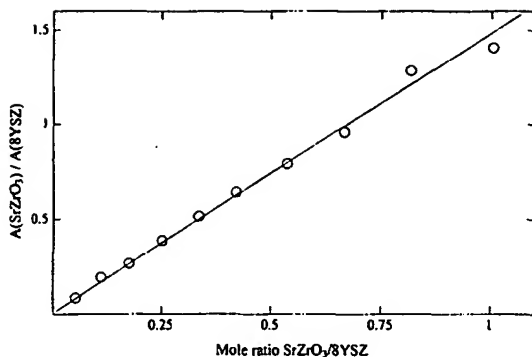


Fig. 1. Ratio of areas of the major XRD peaks of  $\text{SrZrO}_3$  and 8YSZ,  $A(\text{SrZrO}_3)/A(8\text{YSZ})$ , for different compositions of the  $\text{SrZrO}_3/8\text{YSZ}$  powder mixtures.

major peak in the XRD pattern for the 8YSZ, as well as the  $\text{SrZrO}_3$ , were determined and the ratio of these areas was used for the evaluation. Fig. 1 shows the calibration curve for the determination of the amount of the  $\text{SrZrO}_3$  phase.

### 3. Results

The XRD results show that all the eight compositions react with 8YSZ forming  $\text{SrZrO}_3$ . The extent of the product formation is, however, different. The progress of the reaction for the  $\text{La}_{0.6}\text{Sr}_{0.4}\text{Fe}_{0.8}\text{M}_{0.2}\text{O}_{3-\delta}/8\text{YSZ}$  pellets ( $\text{M} = \text{Cr, Mn, Co, Ni}$ ) is shown Fig. 2. The amount of the  $\text{SrZrO}_3$  phase is given as a function of  $t^{1/2}$  in order to indicate the diffusion controlled linear region of these solid state reactions. The formation of  $\text{SrZrO}_3$ , before attaining the linear region, follows S-shaped

curves. This behaviour can be explained [7–9] by the formation of nuclei for the zirconate phase and the fast growing of these nuclei at their initial stage. After a short time, the inflection point is reached and the curve approaches a straight line with a small slope. Slow diffusion processes control the reaction kinetics in this linear region. The open and closed circles in Fig. 2 indicate the samples prepared as described in Section 2, the crosses resulted by crushing and mixing these samples in an agate mortar after 50 h of annealing at 1000°C. The mixing was carried out to help speed up the equilibration process. Fig. 3 shows similar S-shaped curves for the reaction of the  $(\text{La}_{0.6}\text{Sr}_{0.4})_{0.9}\text{Fe}_{0.8}\text{M}_{0.2}\text{O}_{3-\delta}/8\text{YSZ}$  pellets ( $\text{M} = \text{Cr, Mn, Co, Ni}$ ).

The fact that the  $\text{SrZrO}_3$  generation curves, shown in Figs. 2 and 3, have not reached a saturation value suggests that the reactions are not complete within 50 h of annealing at 1000°C. The annealing period of the mixtures was, therefore, prolonged up to 1300 h. These results are indicated in Figs. 2 and 3.

The phases identified after 50 h and 1300 h of annealing differ to some extent as shown for the  $\text{La}_{0.6}\text{Sr}_{0.4}\text{Fe}_{0.8}\text{Mn}_{0.2}\text{O}_{3-\delta}/8\text{YSZ}$  and  $\text{La}_{0.6}\text{Sr}_{0.4}\text{Fe}_{0.8}\text{Co}_{0.2}\text{O}_{3-\delta}/8\text{YSZ}$  pellets in Figs. 4 and 5 as an example. The long annealing period has not only increased the amount of reaction products, but also resulted in the formation of some additional phases. The phases identified with XRD and corroborated by SEM/EDX analysis are given in Table 2. This table also includes the approximate chemical composition of the phases present in some of the annealed samples. The compositions revealed that all phases contain dissolved materials. A significant

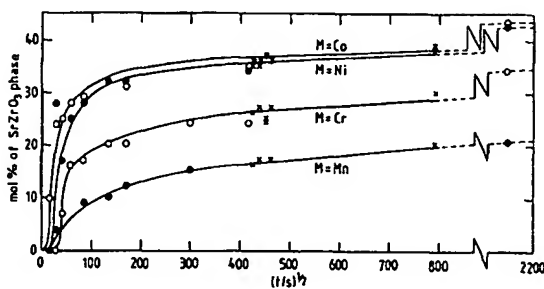


Fig. 2. Fraction of  $\text{SrZrO}_3$  in  $\text{La}_{0.6}\text{Sr}_{0.4}\text{Fe}_{0.8}\text{M}_{0.2}\text{O}_{3-\delta}/8\text{YSZ}$  powder mixtures formed after different time periods at 1000°C ( $\text{M} = \text{Cr, Mn, Co, Ni}$ ).

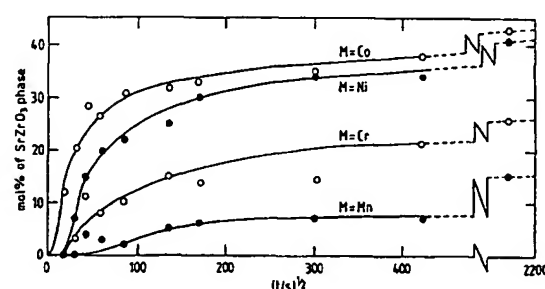


Fig. 3. Fraction of  $\text{SrZrO}_3$  in  $(\text{La}_{0.6}\text{Sr}_{0.4})_{0.9}\text{Fe}_{0.8}\text{M}_{0.2}\text{O}_{3-\delta}/8\text{YSZ}$  powder mixtures formed after different time periods at 1000°C ( $\text{M} = \text{Cr, Mn, Co, Ni}$ ).

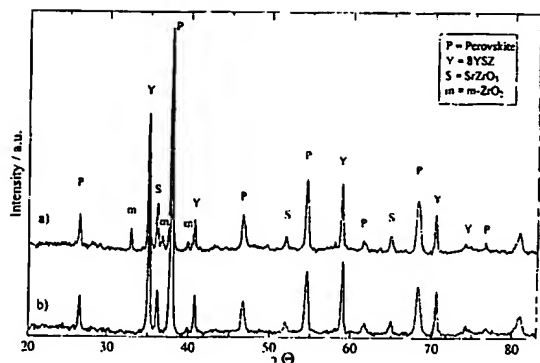


Fig. 4. XRD patterns of La<sub>0.6</sub>Sr<sub>0.4</sub>Fe<sub>0.8</sub>Mn<sub>0.2</sub>O<sub>3-δ</sub>/8YSZ powder mixtures after annealing at 1000°C for (a) 1300 h and (b) 50 h.

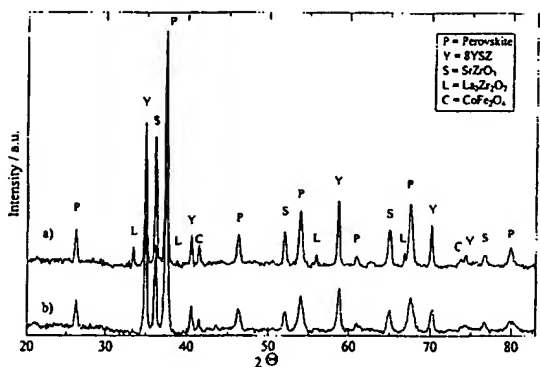


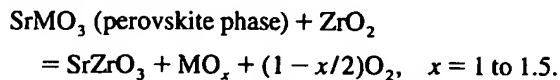
Fig. 5. XRD patterns of La<sub>0.6</sub>Sr<sub>0.4</sub>Fe<sub>0.8</sub>Co<sub>0.2</sub>O<sub>3-δ</sub>/8YSZ powder mixtures after annealing at 1000°C for (a) 1300 h and (b) 50 h.

amount of Zr is, for example, present in the perovskite phase. The dissolution of materials is reflected by the observed shift of the characteristic XRD peaks of the various phases. The SEM/EDX results also revealed that the Sr/La ratio has decreased, as compared to the original value. The extent of the decrease depends on the B-site substituent.

#### 4. Discussion

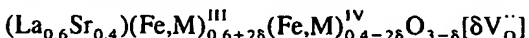
A systematic effect of the B-site substitution on the reactivities of the perovskites is evident. The compatibility experiments revealed that the trend of reactivities of the perovskites La<sub>1-x</sub>Sr<sub>x</sub>Fe<sub>1-y</sub>M<sub>y</sub>O<sub>3-δ</sub> (M = Cr, Mn, Co, Ni) with 8YSZ follows the order Co > Ni > Cr > Mn. The same order of reactivities is valid for the four perovskites with substoichiometry

on A-site. The order of reactivities can be explained by considering the relative stabilities of the compounds SrMO<sub>3</sub> (M = Cr, Mn, Fe, Co, Ni). The perovskites La<sub>1-x</sub>Sr<sub>x</sub>Fe<sub>1-y</sub>M<sub>y</sub>O<sub>3-δ</sub> can be considered as solid solutions of LaMO<sub>3</sub> and SrMO<sub>3</sub>. The chemical components SrMO<sub>3</sub> in the perovskite phase undergo with the ZrO<sub>2</sub> from 8YSZ the following reaction:

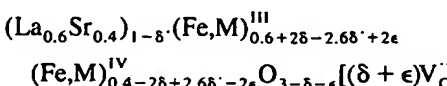


The lower the stability of the dioxide MO<sub>2</sub> relative to the corresponding lower valent oxide MO<sub>x</sub>, the more is the tendency of the dioxide MO<sub>2</sub> in SrMO<sub>3</sub> to form MO<sub>x</sub> by the above reaction, and as a result, the higher is the reactivity of the corresponding perovskite. The observed order of reactivities thus follows the reported [10] trend in stabilities of the tetravalent oxides relative to the lower valent oxides.

The effect of A-site substoichiometry on the reactivity of perovskites follows different trends for the various substituents. The substoichiometry yields reduced reactivities for the Cr or Mn containing perovskites. For the perovskites with Co or Ni, the reactivities do, however, not change significantly. This is in contradiction to the expectation that lowering the Sr content on A-site reduces the activity of Sr, thereby always decreasing the reactivity for the SrZrO<sub>3</sub> formation. This contrasting behaviour of the perovskites containing Co or Ni against those containing Cr or Mn can be explained again by the relative stabilities of the tetravalent oxides of these metals. The perovskites with stoichiometry on A-site can be represented as



and those with substoichiometry as



The substoichiometry ( $\delta'$ ) on A-site leads obviously to a higher fraction of tetravalent atoms on B-site and to some extent to an increase ( $\epsilon$ ) of the oxygen vacancies  $\text{V}_\text{O}^{\text{--}}$ .

Charge compensation is obtained in this way. The increase of the tetravalent B-atoms is responsible for

Table 2

Phases identified by XRD and SEM/EDX in perovskite/8YSZ mixtures annealed at 1000°C for 1300 h

No.	Perovskites	Phases identified and remarks		
		XRD	SEM/EDX	Remarks
1.	$\text{La}_{0.6}\text{Sr}_{0.4}\text{Fe}_{0.8}\text{Cr}_{0.2}\text{O}_{3-\delta}$	8YSZ; perovskite; $\text{SrZrO}_3$ ; monoclinic $\text{ZrO}_2$ ,	8YSZ; perovskite; $\text{SrZrO}_3$ ; iron oxide	1. Occupation at A-site: Sr~32%, Y~2%; Occupation at B-site: Zr~18% 2. Iron oxide peaks in XRD interfered by others
2.	$\text{La}_{0.6}\text{Sr}_{0.4}\text{Fe}_{0.8}\text{Mn}_{0.2}\text{O}_{3-\delta}$	8YSZ; perovskite; $\text{SrZrO}_3$ ; monoclinic $\text{ZrO}_2$ ,	8YSZ; perovskite; $\text{SrZrO}_3$ ; iron oxide	1. Occupation at A-site: Sr~35%, Y~8%; Occupation at B-site: Zr~20% 2. Iron oxide peaks in XRD interfered by others 3. See Fig. 4
3.	$\text{La}_{0.6}\text{Sr}_{0.4}\text{Fe}_{0.8}\text{Co}_{0.2}\text{O}_{3-\delta}$	8YSZ; perovskite; $\text{SrZrO}_3$ ; spinel; $\text{La}_2\text{Zr}_2\text{O}_7$ ,	8YSZ; perovskite; spinel	1. Occupation at A-site Sr~25%, Y~20%; Occupation at B-site Zr~20%, Co~5% 2. Zirconate phases are not clearly identifiable in EDX 3. See Fig. 5
4.	$\text{La}_{0.6}\text{Sr}_{0.4}\text{Fe}_{0.8}\text{Ni}_{0.2}\text{O}_{3-\delta}$	8YSZ; perovskite; $\text{SrZrO}_3$ ; spinel; $\text{La}_2\text{Zr}_2\text{O}_7$ ,	—	—
5.	$(\text{La}_{0.6}\text{Sr}_{0.4})_{0.9}\text{Fe}_{0.8}\text{Cr}_{0.2}\text{O}_{3-\delta}$	8YSZ; perovskite; $\text{SrZrO}_3$ ; monoclinic $\text{ZrO}_2$ ,	—	1. Amount of $\text{SrZrO}_3$ phase smaller than in sample 1 2. Amount of $m\text{-ZrO}_2$ higher than in sample 1
6.	$(\text{La}_{0.6}\text{Sr}_{0.4})_{0.9}\text{Fe}_{0.8}\text{Mn}_{0.2}\text{O}_{3-\delta}$	8YSZ; perovskite; $\text{SrZrO}_3$ ; monoclinic $\text{ZrO}_2$ ,	—	1. Amount of $\text{SrZrO}_3$ phase smaller than in sample 2 2. Amount of $m\text{-ZrO}_2$ slightly higher than in sample 2
7.	$(\text{La}_{0.6}\text{Sr}_{0.4})_{0.9}\text{Fe}_{0.8}\text{Co}_{0.2}\text{O}_{3-\delta}$	8YSZ; perovskite; $\text{SrZrO}_3$ ; spinel; $\text{La}_2\text{Zr}_2\text{O}_7$ ,	—	1. Amount of $\text{La}_2\text{Zr}_2\text{O}_7$ phase higher than in sample 3 2. Amount of $\text{SrZrO}_3$ slightly smaller than in sample 3
8.	$(\text{La}_{0.6}\text{Sr}_{0.4})_{0.9}\text{Fe}_{0.8}\text{Ni}_{0.2}\text{O}_{3-\delta}$	8YSZ; perovskite; $\text{SrZrO}_3$ ; spinel	—	1. No formation of a $\text{La}_2\text{Zr}_2\text{O}_7$ phase (see sample 4) 2. Amount of $\text{SrZrO}_3$ phase slightly smaller than in sample 4

the unchanged reactivity of the Co or Ni containing substoichiometric perovskites, as compared to the corresponding stoichiometric perovskites. The reactivity of the samples containing Cr or Mn remains unaffected by this increase. The increase in tetravalent B-atoms obviously leads to a compensation of the reduced reactivity for the Co or Ni containing perovskites, which is caused by the substoichiometry on A-site.

The reactions of all the samples indicate that the chosen high ratio of  $\text{Sr/La}=4/6$  leads to a precipitation of the  $\text{SrZrO}_3$  phase. The lowering of the strontium content in the perovskite phase by annealing depends on the kind of the B-site substituent. For Co containing samples, it is reduced significantly. Cr or Mn containing perovskites, particularly the substoichiometric samples, have suffered small changes in the Sr content by the formation of  $\text{SrZrO}_3$ .

The perovskites shed off their B-site metals with the loss of Sr from A-site. For Co or Ni containing perovskites, the XRD results indicate the formation of the spinel phases  $MFe_2O_4$ . Cr or Mn containing perovskites, on the other hand, showed no strong XRD lines of  $Fe_2O_3$  or  $Fe_3O_4$  phase in their reaction products, although their SEM/EDX data do indicate the presence of these oxide phases. This low tendency for the release of B-site metals from the Cr or Mn containing samples can be explained as follows: The compositional imbalance due to the loss of Sr from these perovskites is not high and as a result they retain a perovskite phase with A-site substoichiometry. However, in the presence of the diffusion of yttrium atoms from the 8YSZ phase in its neighbourhood, this substoichiometry does not last long. Prolonged annealing of the reaction mixtures forms the monoclinic zirconia phase. The formation of monoclinic  $ZrO_2$  is not observed in Co or Ni containing samples. Following the loss of strontium in significant amounts from these samples, La rich compositions are formed which react further with zirconia, forming  $La_2Zr_2O_7$ . This is evident in the XRD results of their reaction products after prolonged annealing.

The results obtained in this work on the chemical reactions between 8YSZ and the perovskites  $(La_{0.6}Sr_{0.4})_zFe_{0.8}M_{0.2}O_3$  ( $z = 1, 0.9$ ; M=Cr, Mn, Co, Ni) lead to the development of La-Sr-Fe-M-O base perovskites with high chemical compatibility with 8YSZ [5].

### Acknowledgments

The authors thank Dr. Freiburg and Dr. Wallura for their support in the XRD and SEM/EDX analy-

sis. Moreover, they want to acknowledge financial support by the commission of the European Communities (Joule 2 Programme, contract JOU2-CT92-0063).

### References

- [1] O. Yamamoto, Y. Takeda, R. Kanno and M. Noda, *Solid State Ionics* 22 (1987) 241.
- [2] L.-W. Tai, M.M. Nasrallah and H.U. Anderson, in: *Solid Oxide Fuel Cells*, eds. S.C. Singhal and H. Iwahara, PV 93-4 (The Electrochemical Society Softbound Proceedings Series, Pennington, NJ, 1993) p. 241.
- [3] C.C. Chen, M.M. Nasrallah, H.U. Anderson, in: *Solid Oxide Fuel Cells*, eds. S.C. Singhal and H. Iwahara, PV 93-4 (The Electrochemical Society Softbound Proceedings Series, Pennington, NJ, 1993). p. 598.
- [4] L. Kindermann, D. Das, H. Nickel and K. Hilpert, in: *Solid Oxide Fuel Cells IV*, eds. M. Dokiya, O. Yamamoto, H. Tagawa and S.C. Singhal, PV 95-1 (The Electrochemical Society Inc., Pennington, NJ, 1995). p. 985.
- [5] L. Kindermann, D. Das, D. Bahadur, R. Weiss, H. Nickel and K. Hilpert, submitted.
- [6] P. Gordes and N. Christiansen, in: *Proceedings of the 1st European Solid Oxide Fuel Cell Forum*, Luzern, Switzerland, ed. U. Bossel (Baden, Switzerland, 1994) p. 567.
- [7] A.K. Galwey, *Thermochim. Acta* 96 (1985) 259.
- [8] A.K. Galwey, *Chemistry of Solids* (Chapman and Hall, London, 1967) p. 163.
- [9] E.S. Machlin, *Thermodynamics and Kinetics*, (Giro Press, Croton-on-Hudson, NY, 1991) p. 190.
- [10] H. Yokokawa, N. Sakai, T. Kawada and M. Dokiya, *Denki-kagaku-oyobi-kogyo-suri-kagaku* 57 (1989) 821.



## Redox behavior and transport properties of $\text{La}_{0.5-x}\text{Sr}_{0.5-x}\text{Fe}_{0.4}\text{Ti}_{0.6}\text{O}_{3-\delta}$ ( $0 < x < 0.1$ ) validated by Mössbauer spectroscopy

D.P. Fagg <sup>a,\*</sup>, J.C. Waerenborgh <sup>b</sup>, V.V. Kharton <sup>a,c</sup>, J.R. Frade <sup>a</sup>

<sup>a</sup>Department of Ceramics and Glass Engineering, UIMC, University of Aveiro, 3810-193 Aveiro, Portugal

<sup>b</sup>Chemistry Department, Instituto Tecnológico e Nuclear, Estrada Nacional 10, P-2686-953 Sacavém, Portugal

<sup>c</sup>Institute of Physicochemical Problems, Belarus State University, 14 Leningradskaya Str., 220080 Minsk, Belarus

Received 25 June 2001; accepted 1 October 2001

### Abstract

The range of perovskite-type solid solution formation in the system  $\text{La}_{0.5-x}\text{Sr}_{0.5-x}\text{Ti}_{0.6}\text{Fe}_{0.4}\text{O}_{3-\delta}$  in oxidizing conditions is determined from X-ray diffraction and Mössbauer spectroscopy data to correspond to approximately 0–10% of the A-site concentration, similar to other numerous perovskite systems. Reduction and subsequent reoxidation of the oxides leads to a narrowing of this range and the segregation of the hematite phase at  $x = 0.05$ . Increasing A-site deficiency results in the formation of oxygen vacancies and decreasing stability in reducing environments. The total conductivity of  $\text{La}_{0.5-x}\text{Sr}_{0.5-x}\text{Ti}_{0.6}\text{Fe}_{0.4}\text{O}_{3-\delta}$  ( $x = 0.02–0.10$ ) ceramics is essentially independent of composition in air and increases with increasing  $x$  in reducing atmospheres, due to increasing concentrations of n-type charge carriers and the formation of metallic iron. Partial decomposition of the perovskite phase in hydrogen, resulting in metal Fe formation, was found to be reversible when the A-site deficiency is small ( $x < 0.05$ ). Mössbauer spectroscopic data showed that, contrary to other perovskite-type titanates–ferrites, the concentration of  $\text{Fe}^{4+}$  cations in the perovskite lattice of oxidized  $\text{La}_{0.5-x}\text{Sr}_{0.5-x}\text{Ti}_{0.6}\text{Fe}_{0.4}\text{O}_{3-\delta}$  is negligible. © 2002 Elsevier Science B.V. All rights reserved.

**Keywords:** Perovskite; Titanate–ferrite; Mössbauer spectroscopy; Electrical conductivity; Reduction

### 1. Introduction

The dependence of conductivity of the perovskites  $\text{SrTi}_{1-x}\text{Fe}_x\text{O}_{3-\delta}$  on oxygen partial pressure indicated that the ionic conductivity might attain values of about 0.2 S/cm at 1000 °C, with major electronic

contributions in oxidizing conditions (p-type), or for sufficiently reducing conditions (n-type) [1–3]. The significant ionic conductivity of these materials has been confirmed by electrochemical permeability measurements [4,5]. The high level of mixed conductivity exhibited by these materials may suggest a range of possible applications including oxygen sensors, electrochemical membranes and electrode materials for solid oxide fuel cells (SOFCs). Unfortunately, these attractive properties are accompanied by excessively high thermal expansion coefficients (TECs), poor

\* Corresponding author. Tel.: +351-234-370263; fax: +351-234-425300.

E-mail address: [duncan@cv.ua.pt](mailto:duncan@cv.ua.pt) (D.P. Fagg).

stability both in highly reducing conditions ( $p(O_2) < 10^{-12}$  Pa), and also reactivity with substrate materials such as yttria-stabilized zirconia (YSZ) at elevated temperatures [4–6]. Previous work has shown that improvements in stability could be obtained by the replacement of some Sr on the A sites of the  $ABO_3$  perovskite lattice by lanthanum [6,7]. For the series  $La_xSr_{1-x}Ti_{0.6}Fe_{0.4}O_{3-\delta}$ , stabilization against both reduction and reaction with YSZ was obtained for compositions containing greater than 40% La ( $x \geq 0.4$ ) [6]. The substitution of La was also shown to reduce thermal expansion offering compositions, which exhibited similar TECs to that of YSZ [7]. The potentially beneficial effects of La substitution were, sadly, offset by the fact that the presence of La led to the detrimental effects both on ionic conductivity and on total conductivity in air [6,7]. Total conductivity in reducing conditions was also low in these materials, for example, maximum conductivity in reducing conditions for the system  $La_xSr_{0.9-x}Ti_{0.6}Fe_{0.4}O_{3-\delta}$  was less than 1 S/cm at 800 °C [7]. However, the observation that compositions that possessed A-site deficiency exhibited the presence of metallic Fe in reducing conditions leads to this study. For use as SOFC anodes, the presence of metallic iron as a secondary phase in reducing conditions might offer benefits, not only with respect to the levels of total conductivity, but also with respect to the electro-catalytic activity for the anode reaction. In this work, the effect of A-site deficiency on the total conductivity and oxidation state of iron is studied, utilizing Mössbauer spectroscopy as a powerful technique to reveal the state and coordination of iron cations in the lattice [8–10]. Particular attention was given to the formation of metallic iron under reducing conditions, which might be important for the applications in SOFC anodes and hydrocarbon oxidation membranes.

## 2. Experimental

Powders of  $La_{0.5-x}Sr_{0.5-x}Ti_{0.6}Fe_{0.4}O_{3-\delta}$  ( $x = 0.02, 0.05$ , and  $0.10$ ) were obtained by the solid state reaction of high-purity  $TiO_2$ ,  $Fe_2O_3$ ,  $La_2O_3$  and  $SrCO_3$ . Calcination at 1300 °C for 12 h was followed by milling to destroy agglomerates and preparation of dense pellets by uniaxial pressing and sintering for 5 h at 1600 °C. X-ray powder diffraction (XRD) data

were collected using a Rigaku Geigerflex diffractometer; the refinement was performed using Fullprof program [11]. Impedance spectra were obtained on bar-shaped specimens by a four-electrode ac method using a frequency response analyser HP428A; an oxygen sensor was utilized to record oxygen activity in the gas phase. Weight losses in reducing conditions was assessed by thermogravimetry. More detailed description of the experimental procedures and equipment used for the materials' characterization can be found elsewhere (Refs. [4–7] and references therein).

Mössbauer spectroscopy was performed in air on samples taken from the same batch of each composition annealed in two different conditions. Samples (A) were annealed in air for 12 h at 1000 °C and slowly cooled, whereas samples (B) were annealed for 12 h at 1000 °C in a dry  $H_2-N_2$  gas mixture flow (10 vol.%  $H_2$ ) and quenched. Finally, samples (C) were obtained by reoxidizing samples (B) at 1000 °C for 12 h in air. Spectra were measured in transmission mode using a conventional constant-acceleration spectrometer and a 25 m Ci  $^{57}Co$  source in an Rh matrix. The velocity scale was calibrated using an  $\alpha$ -Fe foil at room temperature. Absorbers were obtained by pressing the sample powder (5 mg of natural  $Fe/cm^2$ ) into a perspex holder. Mössbauer spectra were fitted to lorentzian lines using a nonlinear least-squares computer method [8]. Isomer shifts are given relative to metallic  $\alpha$ -Fe at room temperature. Relative areas and line widths of each peak in a quadrupole doublet as well as the widths ( $\Gamma_{1,6}$ ,  $\Gamma_{2,5}$ ,  $\Gamma_{3,4}$ ) and the relative areas ( $I_{1,6}$ ,  $I_{2,5}$ ,  $I_{3,4}$ ) of peaks (1–6), (2–5) and (3–4) in each magnetic sextet were always kept equal during refinement.

## 3. Results and discussion

XRD results showed the formation of the perovskite phase with the orthorhombic distortion (S.G. Pnma) for all synthesized  $La_{0.5-x}Sr_{0.5-x}Ti_{0.6}Fe_{0.4}O_{3-\delta}$  ( $x = 0.02–0.10$ ). In the case of  $La_{0.4}Sr_{0.4}Ti_{0.6}Fe_{0.4}O_{3-\delta}$ , trace amounts of secondary phase,  $Fe_2O_3$ , were observed in the XRD patterns. Lattice parameters and unit cell volumes of the perovskite phases as prepared in air are listed in Table 1. Increasing the A-site deficiency leads to an increase in the cell volume, probably due to the increasing anion repulsion in the lattice. In all cases,

Table 1  
Perovskite unit cell parameter of  $\text{La}_{0.5-x}\text{Sr}_{0.5-x}\text{Ti}_{0.6}\text{Fe}_{0.4}\text{O}_{3-\delta}$ , as prepared in air

Composition	$a$ (Å)	$b$ (Å)	$c$ (Å)	Unit cell volume (Å <sup>3</sup> )
0.02	5.514	7.829	5.532	238.82
0.05	5.519	7.832	5.530	238.99
0.10	5.525	7.832	5.528	239.21

reduction in a dry 10%  $\text{H}_2$ –90%  $\text{N}_2$  mixture at 1000 °C resulted in the formation of metallic iron. As an example, Fig. 1 presents the XRD patterns  $\text{La}_{0.4}\text{Sr}_{0.4}\text{Fe}_{0.6}\text{Ti}_{0.4}\text{O}_{3-\delta}$  after synthesis and after reduction during 12 h; other compositions tested show similar results.

The Mössbauer spectra of samples of the A and B series are shown in Figs. 2 and 3. The spectra of samples (C) are similar to those of samples (A). The differences observed are on the relative amounts of the secondary hematite phase, which was observed for  $x=0.10$  in the case of series A, and for  $x=0.05$  and 0.10 for series C (Table 2), in agreement with XRD results.

For the oxidized samples, the spectra which consisted of a single doublet included those of the  $x=0.05$  (A) and  $x=0.02$  (A and C). The isomer shifts, IS, and quadrupole splittings, QS, of these doublets (Table 2) are similar to those reported for  $\text{Fe}^{3+}$  in octahedral coordination in  $\text{CaFe}_x\text{Ti}_{1-x}\text{O}_{3-\delta}$  and  $\text{SrFe}_x\text{Ti}_{1-x}\text{O}_{3-\delta}$  [8]. In the  $\text{La}_{0.48}\text{Sr}_{0.48}\text{Fe}_{0.6}\text{O}_{3-\delta}$  phases of A and C series, no anion vacancies are expected in oxidizing conditions. For  $x=0.05$  (A), the value of  $\delta=0.075$  could be expected assuming that all iron cations are

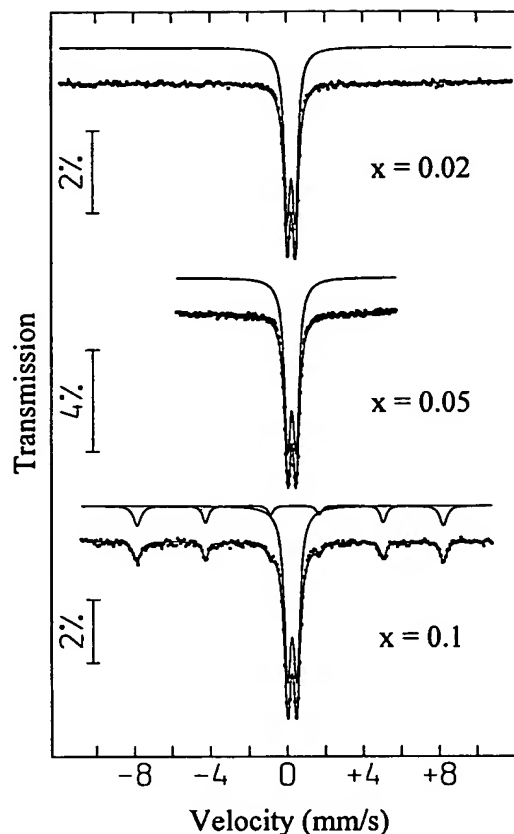


Fig. 2. Mössbauer spectra of as-prepared  $\text{La}_{0.5-x}\text{Sr}_{0.5-x}\text{Fe}_{0.4}\text{Ti}_{0.6}\text{O}_{3-\delta}$  (series A) at room temperature. The total function calculated is represented on the experimental points. Quadrupole doublets due to  $\text{Fe}^{3+}$  in the perovskite structure and the magnetic sextet assigned to  $\alpha\text{Fe}_2\text{O}_3$  are shown slightly shifted, for clarity.

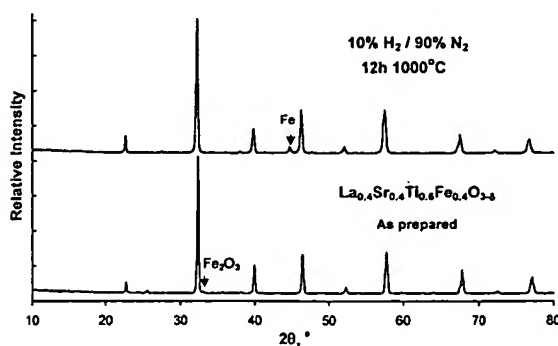


Fig. 1. XRD patterns of as-prepared and reduced  $\text{La}_{0.4}\text{Sr}_{0.4}\text{Fe}_{0.6}\text{Ti}_{0.4}\text{O}_{3-\delta}$ .

trivalent. Although this oxygen vacancy concentration is low, the presence of  $\text{Fe}^{3+}$  coordinated by less than six anions cannot be excluded a priori. However, the shapes of the two-peak spectra (Fig. 2) do not justify the fitting of a second quadrupole doublet. Therefore, if pentacoordinated  $\text{Fe}^{3+}$  is present in these materials in significant amounts, it is not as easy to detect as in  $\text{CaFe}_x\text{Ti}_{1-x}\text{O}_{3-y}$  perovskites [8]. On the other hand, considering that doublets with the very large QS and the small IS characteristic of tetracoordinated  $\text{Fe}^{3+}$  in the Ca-containing perovskite phases [8] are clearly absent, no local ordering of the anion vacancies seems to occur as in the case of  $\text{SrFeO}_{3-\delta}$ -based perovskites [8–10].

Table 2

Parameters estimated from room temperature Mössbauer spectra of  $\text{La}_{0.5-x}\text{Sr}_{0.5-x}\text{Fe}_{0.4}\text{Ti}_{0.6}\text{O}_3-\delta$  samples annealed in air at 1000 °C (A), in dry 10%  $\text{H}_2$ –90%  $\text{N}_2$  mixture at 1000 °C (B) and reoxidized in air at 1000 °C (C)

$x$	Series	Iron state	IS (mm/s)	QS (mm/s)	$B_{hf}$ (T)	$\Gamma$ (mm/s)	$I$ (%)
0.02	(A)	$\text{Fe}^{3+}$	0.36	0.43	–	0.37	100
	(B)	$\text{Fe}^{3+}$	0.39	0.42	–	0.46	74
		$\text{Fe}^{2+}$	0.94	1.26	–	0.61	21
		$\alpha\text{-Fe}$	–0.01	0.00	33.3	0.29	5
	(C)	$\text{Fe}^{3+}$	0.36	0.43	–	0.37	100
		$\text{Fe}^{3+}$	0.36	0.44	–	0.38	100
0.05	(A)	$\text{Fe}^{3+}$	0.39	0.43	–	0.48	52
		$\text{Fe}^{2+}$	0.96	1.39	–	0.64	31
		$\alpha\text{-Fe}$	0.00	0.01	33.3	0.29	17
	(C)	$\text{Fe}^{3+}$	0.37	0.45	–	0.37	85
		$\alpha\text{Fe}_2\text{O}_3$	0.40	–0.24	50.2	0.35	15
		$\text{Fe}^{3+}$	0.36	0.47	–	0.41	78
0.10	(A)	$\text{Fe}^{3+}$	0.39	–0.22	49.8	0.32	22
		$\alpha\text{Fe}_2\text{O}_3$	0.32	0.53	–	0.54	60
		$\text{Fe}^{2+}$	0.98	1.57	–	0.63	39
		$\alpha\text{-Fe}$	0.00	0.01	33.2	0.27	37
	(C)	$\text{Fe}^{3+}$	0.37	0.45	–	0.42	71
		$\alpha\text{Fe}_2\text{O}_3$	0.37	–0.21	51.8	0.32	29

IS is the isomer shift relative to metallic  $\alpha\text{-Fe}$  at 295 K. QS is the quadrupole splitting measured for doublets or  $(e^2V_{ZZ}Q/4)(3\cos^2\theta-1)$  quadrupole shift calculated from  $(\phi_1+\phi_6-\phi_2-\phi_5)/2$ , where  $\phi_n$  is the shift of the  $n$ th line of the sextet due to quadrupole coupling.

$B_{hf}$ ,  $\Gamma$  and  $I$  are the magnetic hyperfine field, full width at half maximum and the relative areas, respectively.

Estimated standard deviations are <2% for  $I$ , <0.2 T for  $B_{hf}$  and <0.02 mm/s for the other parameters.

Besides the  $\text{Fe}^{3+}$  doublet, the spectra of  $x=0.05$  (C) and both  $x=0.10$  (A) and (C) samples show a magnetic sextet typical of hematite (Fig. 2 and Table 2), in agreement with XRD data. Considering, as a first approximation, that the recoil-less fractions of Fe in the different phases are similar, the relative areas of the doublets and sextets are proportional to the amount of Fe present in each phase, which makes it possible to estimate the chemical composition of the perovskites. The tentative unit formulas normalized for one B-site cation per formula unit (f.u.) are summarized in Table 3.

It should be mentioned that no presence of  $\text{Fe}^{4+}$  was observed in  $\text{La}_{0.5-x}\text{Sr}_{0.5-x}\text{Ti}_{0.6}\text{Fe}_{0.4}\text{O}_3-\delta$  under any conditions, within the sensitivity limits of the Mössbauer spectroscopy method (1–2%). This contrasts with the results found for similar perovskite-like

titanate–ferrites such as  $\text{CaTi}_{1-x}\text{Fe}_x\text{O}_3-\delta$  [8],  $\text{La}_{1-x}\text{Ca}_x\text{FeO}_3-\delta$  [12,13], or  $\text{SrTi}_{1-x}\text{Fe}_x\text{O}_3-\delta$  [8], where considerable fractions of iron cations exist in air in the tetravalent state. The presence of a large amount of  $\text{La}^{3+}$  replacing  $\text{Sr}^{2+}$  compensates the substitution of  $\text{Ti}^{4+}$  by  $\text{Fe}^{3+}$ ; even with no  $\text{Fe}^{4+}$  present, the oxygen nonstoichiometry of the materials of A and C series is lower than 0.08 (Table 3). These concentrations of anion vacancies are low when compared to the oxygen nonstoichiometry characteristic of  $\text{CaFe}_x\text{Ti}_{1-x}\text{O}_3-\delta$  and  $\text{SrFe}_x\text{Ti}_{1-x}\text{O}_3-\delta$  [8] and perhaps offer a lower driving force for  $\text{Fe}^{4+}$  formation.

In addition to the  $\text{Fe}^{3+}$  doublet, the reduced samples (series B) show a second doublet with higher IS and QS, typical of high-spin  $\text{Fe}^{2+}$ , and a sextet with hyperfine parameters characteristic of  $\alpha\text{-Fe}$  metal (Fig. 3 and Table 2). The relative areas of the  $\text{Fe}^{2+}$  and  $\alpha\text{-Fe}$  components increase with  $x$ , i.e. as the concentrations of La and Sr decrease. This corresponds to a progressively higher oxygen loss during reduction for increasing  $x$ , which agrees with the weight reduction on annealing  $\text{La}_{0.5-x}\text{Sr}_{0.5-x}\text{Ti}_{0.6}\text{Fe}_{0.4}\text{O}_3-\delta$  in 10%  $\text{H}_2$ –90%  $\text{N}_2$  gas mixture (Fig. 4).

There are two possibilities when considering  $\text{Fe}^{2+}$  formation: either (i)  $\text{Fe}^{2+}$  exists in the perovskite structure, or (ii) it forms in an additional phase such as wustite. A major part of the divalent iron is likely to be incorporated in the perovskite phase as in case (i) due to the following reasons. Firstly, this would be consistent with the fact that no additional phases besides  $\alpha\text{-Fe}$  metal were detected by XRD in the samples of B series. Secondly, previous work [6,7]

Table 3  
Formula unit of the perovskite phases, deduced from the Mössbauer data on  $\text{La}_{0.5-x}\text{Sr}_{0.5-x}\text{Fe}_{0.4}\text{Ti}_{0.6}\text{O}_3-\delta$

$x$	Series	Formula	$\delta$
0.02	(A)	$\text{La}_{0.48}\text{Sr}_{0.48}\text{Fe}_{0.4}\text{Ti}_{0.6}\text{O}_3$	0.00
	(B)	$\text{La}_{0.49}\text{Sr}_{0.49}\text{Fe}^{3+}_{0.302}\text{Fe}^{2+}_{0.086}\text{Ti}_{0.61}\text{O}_{2.99}^a$	0.01
	(C)	$\text{La}_{0.48}\text{Sr}_{0.48}\text{Fe}_{0.4}\text{Ti}_{0.6}\text{O}_3$	0.00
0.05	(A)	$\text{La}_{0.45}\text{Sr}_{0.45}\text{Fe}_{0.4}\text{Ti}_{0.6}\text{O}_{2.925}$	0.075
	(B)	$\text{La}_{0.48}\text{Sr}_{0.48}\text{Fe}^{3+}_{0.22}\text{Fe}^{2+}_{0.13}\text{Ti}_{0.65}\text{O}_{2.96}^a$	0.04
	(C)	$\text{La}_{0.48}\text{Sr}_{0.48}\text{Fe}^{3+}_{0.36}\text{Ti}_{0.64}\text{O}_{3.02}$	0.00
0.10	(A)	$\text{La}_{0.44}\text{Sr}_{0.44}\text{Fe}^{3+}_{0.34}\text{Ti}_{0.66}\text{O}_{2.93}$	0.07
	(B)	$\text{La}_{0.47}\text{Sr}_{0.47}\text{Fe}^{3+}_{0.11}\text{Fe}^{2+}_{0.18}\text{Ti}_{0.70}\text{O}_{2.87}^a$	0.13
	(C)	$\text{La}_{0.45}\text{Sr}_{0.45}\text{Fe}^{3+}_{0.32}\text{Ti}_{0.68}\text{O}_{2.98}$	0.02

<sup>a</sup> Estimations performed under the assumption that all  $\text{Fe}^{2+}$  cations are present in the perovskite phase.

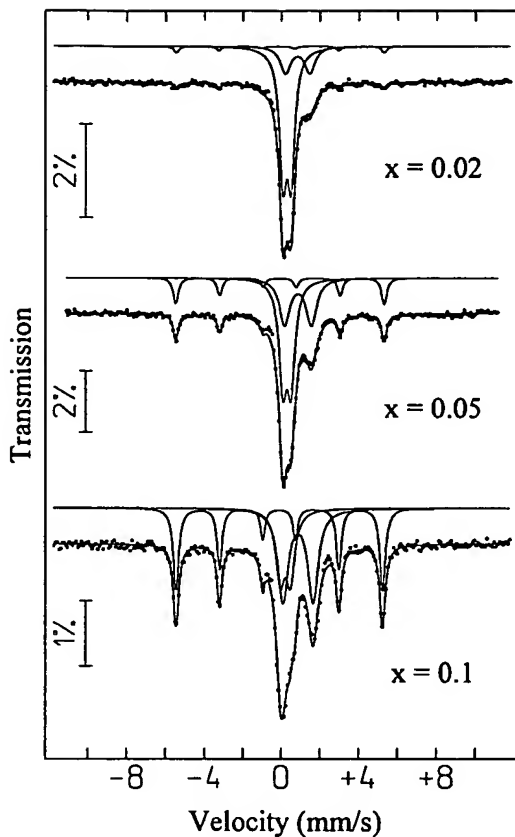


Fig. 3. Mössbauer spectra of reduced  $\text{La}_{0.5-x}\text{Sr}_{0.5-x}\text{Fe}_{0.4}\text{Ti}_{0.6}\text{O}_{3-\delta}$  (series B) at room temperature. The total function calculated is represented on the experimental points. Quadrupole doublets attributed to  $\text{Fe}^{3+}$  and  $\text{Fe}^{2+}$  (larger splitting) in the perovskite structure as well as the magnetic sextet assigned to metallic  $\alpha\text{-Fe}$  are shown slightly shifted, for clarity.

showed the reduction of La-free  $\text{SrTi}_{1-x}\text{Fe}_x\text{O}_{3-\delta}$  compositions under similar conditions occurs through the formation of a Ruddlesden–Popper  $\text{A}_4\text{B}_3\text{O}_{10}$  phase and metallic iron. Similar behavior is also typical for the reduction of other perovskite phases, e.g. cobaltites and nickelates (for example, Ref. [14]). Although the compositions studied in this work do not reveal such dramatic changes in the perovskite structure after reduction, it is prudent to expect that similar formation of  $\text{Fe}^{2+}$ , probably associated with oxygen vacancies in localized domains, would occur in the lattice. Considering again the similar recoil-less fractions for Fe in the different phases and oxidation states, the formula units of the perovskites present in

each sample for the case (i) were deduced from the estimated relative areas (Table 3).

The data presented in Table 2 reveal that for the  $x=0.02$  and  $0.05$  samples metallic Fe formed in reducing conditions results from perovskite decomposition. For  $\text{La}_{0.4}\text{Sr}_{0.4}\text{Ti}_{0.6}\text{Fe}_{0.4}\text{O}_{3-\delta}$ , more metallic iron is formed than that possible from solely the reduction of the  $\text{Fe}_2\text{O}_3$  secondary phase solely. The large amount of metallic iron formed might be accommodated by the formation of Ruddlesden–Popper phases, in agreement with previous results [6,7] and numerous literature data [14], but at a level not resolvable by XRD. Interestingly, on reoxidation of the  $x=0.02$  sample at  $1000^\circ\text{C}$  for 12 h, the Fe content of the perovskite phase is recovered suggesting the above referred, Fe loss is reversible. Perovskite compositions with higher A-site vacancy concentrations are less stable. In the case of  $\text{La}_{0.45}\text{Sr}_{0.45}\text{Ti}_{0.6}\text{Fe}_{0.4}\text{O}_{3-\delta}$ , reoxidation is unable to restore the single perovskite phase originally synthesized, probably due to kinetic reasons. About 15% of iron remains segregated into the secondary  $\alpha\text{-Fe}_2\text{O}_3$  phase. Finally,  $\text{La}_{0.4}\text{Sr}_{0.4}\text{Fe}_{0.4}\text{Ti}_{0.6}\text{O}_{3-\delta}$  could not be prepared single-phase and for this composition, the redox cycle further increased the amount of Fe segregated from the perovskite phase.

Thus, the perovskite solid solution formation range in the A-site-deficient  $\text{La}_{0.5-x}\text{Sr}_{0.5-x}\text{Ti}_{0.6}\text{Fe}_{0.4}\text{O}_{3-\delta}$

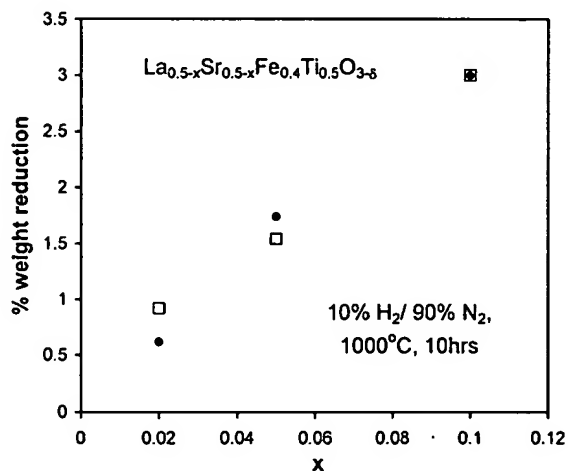


Fig. 4. Weight reduction of  $\text{La}_{0.5-x}\text{Sr}_{0.5-x}\text{Ti}_{0.6}\text{Fe}_{0.4}\text{O}_{3-\delta}$  on annealing in a dry 10%  $\text{H}_2$ –90%  $\text{N}_2$  flow at  $1000^\circ\text{C}$  for 10 h. Two data sets are shown to indicate reproducibility.

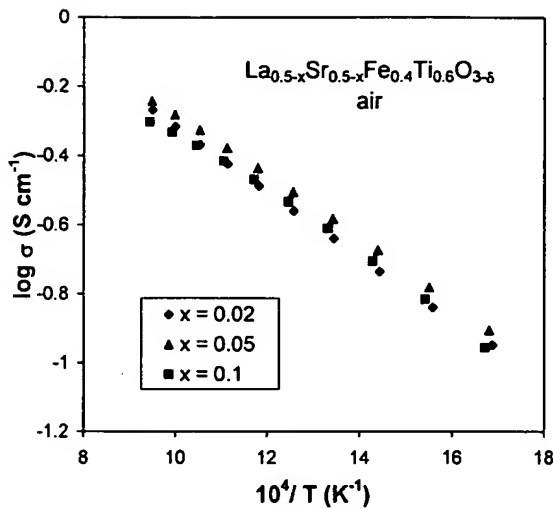


Fig. 5. Temperature dependence of the total electrical conductivity of  $\text{La}_{0.5-x}\text{Sr}_{0.5-x}\text{Ti}_{0.6}\text{Fe}_{0.4}\text{O}_{3-\delta}$  ceramics in atmospheric air.

system corresponds to approximately 0–10% of the A-site concentration, similar to other known perovskite-type systems such as  $(\text{La}, \text{Sr})\text{CoO}_{3-\delta}$  cobaltites [14,15]. Reduction and reoxidation of the materials lead to a narrowing of this range, which may be associated with kinetic limitations at intermediate temperatures where cation diffusion coefficients are low.

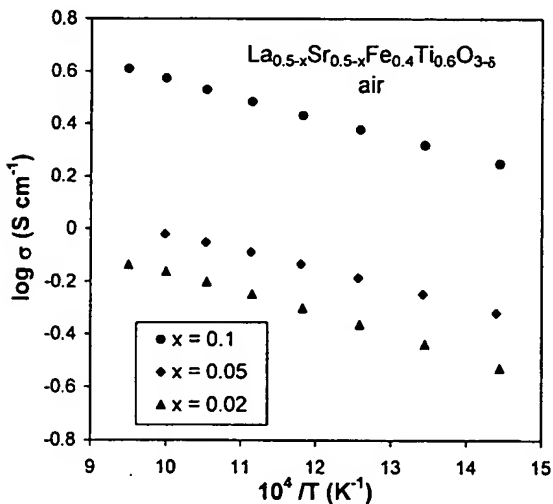


Fig. 6. Temperature dependence of the total electrical conductivity of  $\text{La}_{0.5-x}\text{Sr}_{0.5-x}\text{Ti}_{0.6}\text{Fe}_{0.4}\text{O}_{3-\delta}$  ceramics in a dry 10%  $\text{H}_2$ –90%  $\text{N}_2$  flow.

The temperature dependence of the total conductivity of  $\text{La}_{0.5-x}\text{Sr}_{0.5-x}\text{Ti}_{0.6}\text{Fe}_{0.4}\text{O}_{3-\delta}$  ceramics in air is shown in Fig. 5. The level of total conductivity in air is observed to be similar for all compositions in this system. The introduction of A-site vacancies can be compensated by the formation of oxygen vacancies and/or changes in the electron-hole concentration ( $\text{Fe}^{4+}$  cations) [1,2]. As conductivity is observed to be similar for each composition, the former charge compensation mechanism is probably predominant in air. This is in agreement with the Mössbauer spectroscopy data showing no formation of tetravalent iron (Fig. 2), as discussed above. Similar behaviour is characteristic of  $(\text{La}, \text{Sr})\text{CoO}_{3-\delta}$  perovskites [14,15].

In reducing conditions, the conductivity of  $\text{La}_{0.5-x}\text{Sr}_{0.5-x}\text{Ti}_{0.6}\text{Fe}_{0.4}\text{O}_{3-\delta}$  increases with increasing A-site deficiency (Fig. 6). This trend can be explained by reference to Table 2 and Fig. 4, which, respectively, show increases in  $\text{Fe}^{2+}$  and  $\alpha\text{-Fe}$  formation and increases in the percentage weight reduction of these compositions on increasing  $x$ . The compositions that exhibit the higher weight loss are also those which show the higher concentrations of  $\text{Fe}^{2+}$  and  $\alpha\text{-Fe}$  and the higher conductivity. The activation energy values for the total conductivity in reducing conditions, summarized in Table 4, are in the range typical for the small polaron mechanism of electronic conduction [14,16]. In this case, the electronic transport in the perovskite phases can be suggested to occur via the charge transfer between  $\text{Fe}^{2+}$  and  $\text{Fe}^{3+}$  [16]. The higher the level of A-site deficiency the higher the concentration of  $\text{Fe}^{2+}$  charge carriers (Table 3) and subsequently the higher the level of total conductivity recorded in reducing conditions. The percolation threshold for conduction due to the presence of metallic Fe does not appear to have been reached.

Table 4  
Parameters of the Arrhenius regression model  $\sigma T = A_0 \exp(-E_a/RT)$  for the temperature dependence of the electrical conductivity of  $\text{La}_{0.5-x}\text{Sr}_{0.5-x}\text{Ti}_{0.6}\text{Fe}_{0.4}\text{O}_{3-\delta}$  ceramics

x	Air		10% $\text{H}_2$ –90% $\text{N}_2$	
	$E_a$ (kJ/mol)	$A_0 \times 10^4$ (SK/cm)	$E_a$ (kJ/mol)	$A_0 \times 10^5$ (SK/cm)
0.02	23.6	1.2	22.8	1.1
0.05	23.8	0.9	22.1	1.3
0.10	25.6	0.8	20.6	4.4

The maximum conductivity for the studied compositions in reducing conditions is 4 S/cm at 800 °C, a value that is still too low for use as an electrode in SOFCs.

#### 4. Conclusion

The solid solution formation range, determined by X-ray diffraction and Mössbauer spectroscopy studies in the A-site-deficient perovskite system  $\text{La}_{0.5-x}\text{Sr}_{0.5-x}\text{Ti}_{0.6}\text{Fe}_{0.4}\text{O}_{3-\delta}$ , corresponds in oxidizing conditions to approximately 0–10% of the A-site concentration, similar to lanthanum–strontium cobaltites. Reduction and reoxidation of the oxides at 1000 °C leads to a narrowing of this range and the segregation of hematite at  $x=0.05$ , a phenomenon probably due to the kinetic limitations associated with slow cation diffusion at intermediate temperatures. Increasing the A-site deficiency results in the formation of oxygen vacancies and decreasing stability in reducing environments. The total conductivity of  $\text{La}_{0.5-x}\text{Sr}_{0.5-x}\text{Ti}_{0.6}\text{Fe}_{0.4}\text{O}_{3-\delta}$  ( $x=0.02-0.10$ ) ceramics is essentially independent of the composition in air and increases with  $x$  in reducing atmospheres, due to the increasing concentrations of n-type charge carriers in the perovskite and the formation of metallic iron. The partial decomposition of the perovskite phase in hydrogen, resulting in metal Fe formation, is reversible when the A-site deficiency is small ( $x < 0.05$ ). Contrary to other perovskite-type ferrites, Mössbauer spectroscopy revealed that no tetravalent iron cations exist in the lattice of  $\text{La}_{0.5-x}\text{Sr}_{0.5-x}\text{Ti}_{0.6}\text{Fe}_{0.4}\text{O}_{3-\delta}$  in air. This factor leads to poor levels of the p-type conductivity obtainable in oxidizing conditions. The maximum total conductivity values observed for these composition at 800 °C are 0.55 S/cm in air and 4 S/cm in reducing conditions, values that are too low for electrochemical applications such as SOFC electrodes or electrochemical membranes for hydrocarbon oxidation.

#### Acknowledgements

This work was supported by the FCT (Praxis program and the contract P/CTM/14170/98).

#### References

- [1] S. Steinvik, R. Bugge, J. Gjonne, J. Tafto, T. Norby, *J. Phys. Chem. Solids* 6 (1997) 969.
- [2] S. Steinvik, T. Norby, P. Kofstad, in: R. Waser (Ed.), *Proc. Int. Conf. Electroceramics IV*, vol. 2, Aachen, Germany, 1994, p. 691.
- [3] R. Moos, W. Meneskou, H.-J. Schreiner, K.H. Haerdtl, *Sens. Actuators, B* 67 (2000) 178.
- [4] V.V. Kharton, A.V. Kovalevsky, A.P. Viskup, J.R. Jurado, F.M. Figueiredo, E.N. Naumovich, J.R. Frade, *J. Solid State Chem.* 156 (2001) 437.
- [5] V.V. Kharton, F.M. Figueiredo, A.V. Kovalevsky, A.P. Viskup, E.N. Naumovich, J.R. Jurado, J.R. Frade, *Defect Diffus. Forum* 186–187 (2000) 119.
- [6] D.P. Fagg, V.V. Kharton, A.V. Kovalevsky, A.P. Viskup, E.N., Naumovich, J.R. Frade, *J. Eur. Ceram. Soc.* 21 (2001) 1831.
- [7] D.P. Fagg, V.V. Kharton, J.R. Frade, A.A.L. Labrincha, Stability and mixed ionic-electronic conductivity of (Sr, La) (Ti, Fe)O<sub>3- $\delta$</sub>  perovskites, *J. Materials Chemistry*, submitted.
- [8] J.C. Waerenborgh, F.M. Figueiredo, J.R. Frade, M.T. Colomer, J.R. Jurado, *J. Phys.: Condens. Matter* 13, No. 35 (3 September 2001) 8171.
- [9] D.E. Mack, S. Wissmann, K.D. Bekker, *Solid State Ionics* 135 (2000) 625.
- [10] S. Wissmann, K.D. Becker, *Solid State Ionics* 85 (1996) 279.
- [11] J. Rodriguez-Carvajal, *Physica B* 192 (1993) 55.
- [12] J.-C. Grenier, M. Pouchard, P. Hagenmuller, M.J.R. Enche, M. Vallet, J.M.G. Calbert, M.A. Alario-Franco, *Rev. Chim. Miner.* 20 (1983) 726.
- [13] M.A. Alario-Franco, J.M.G. Calbert, M. Vallet-Regi, J.-C. Grenier, *J. Solid State Chem.* 49 (1983) 219.
- [14] V.V. Kharton, A.A. Yaremchenko, E.N. Naumovich, *J. Solid State Electrochem.* 3 (1999) 303.
- [15] A.V. Kovalevsky, V.V. Kharton, V.N. Tikhonovich, E.N. Naumovich, A.A. Tonoyan, O.P. Reut, L.S. Boginsky, *Mater. Sci. Eng., B* 52 (1998) 105.
- [16] J. Mizusaki, *Solid State Ionics* 52 (1992) 79.

## The effect of thermal treatment on the resistance of LSCF electrodes on gadolinia doped ceria electrolytes

D. Waller\*, J.A. Lane, J.A. Kilner, B.C.H. Steele

Department of Materials, Imperial College of Science, Technology and Medicine, Prince Consort Road, London SW7 2BP, United Kingdom

---

### Abstract

The effect of thermal treatment on the structure and electrical characteristics of  $\text{La}_{1-x}\text{Sr}_x\text{Fe}_{1-y}\text{Co}_y\text{O}_{3-\delta}$  (LSCF) electrodes on  $\text{Ce}_{0.9}\text{Gd}_{0.1}\text{O}_{1.95}$  (CGO) electrolytes has been investigated. Low calcination temperatures and short sintering times leads to the formation of a cubic A-site deficient perovskite, with the composition  $\text{La}_{0.6}\text{Sr}_{0.13}\text{Co}_{0.2}\text{Fe}_{0.8}\text{O}_{2.52}$ , which exhibits a low electrode resistance. Higher calcination temperatures and longer sintering times leads to the incorporation of strontium, derived from the decomposition of  $\text{SrCO}_3$ , into the perovskite structure, producing a stoichiometric rhombohedral perovskite. Electrodes containing a larger proportion of the stoichiometric perovskite had a higher resistance than those consisting largely of the A-site deficient perovskite.

**Keywords:** Solid oxide fuel cell; Perovskite; Cerium oxide electrolyte; Ionic conductor-oxygen; Fuel cell

---

### 1. Introduction

In recent years much interest has been expressed in gadolinia doped ceria electrolytes (CGO), for use in solid oxide fuel cells (SOFC's) and electrically pumped ceramic oxygen generators (COG's). In these electrochemical devices a dense CGO electrolyte membrane separates two different gaseous environments. In the case of the fuel cell the membrane separates the oxidant and the fuel gases and in the COG, the membrane separates the oxygen product from the oxygen source (air). Both of these devices require an electrode on each surface of the electrolyte membrane. Meadowcroft originally suggested that mixed conducting oxides, with the perovskite structure, would be suitable candidate materials

for fuel cell cathodes due to their high electrical and ionic conductivities [1]. For use with ceria based electrolytes,  $\text{La}_{1-x}\text{Sr}_x\text{CoO}_{3-\delta}$  (LSC), and more recently  $\text{La}_{1-x}\text{Sr}_x\text{Fe}_{1-y}\text{Co}_y\text{O}_{3-\delta}$ , are very promising electrode materials [2,3]. Research into reducing the electrode resistance is importance because in a typical device, such as a COG based on a 100  $\mu\text{m}$  CGO plate with LSCF electrodes, some 95 to 98% of the resistance of the membrane is due to the electrode [4]. Therefore, even a small reduction in the electrode resistance can lead to a large increase in the ion current through the membrane and hence, an increase in the current produced by a fuel cell or an increase in the flux of oxygen in a COG.

We have investigated some of the parameters in the preparation of  $\text{La}_{0.6}\text{Sr}_{0.4}\text{Co}_{0.2}\text{Fe}_{0.8}\text{O}_{3-\delta}$  electrodes on CGO electrolytes. The thermal treatment of the LSCF powder before depositing on the CGO

---

\*Corresponding author.

surface and its subsequent sintering treatment are both found to effect the resistance of the electrode. The change in resistance of the LSCF electrode was a reflection of the changes in the bulk structure of the LSCF during thermal treatment.

## 2. Experimental methods

### 2.1. Preparation of materials

$\text{Ce}_{0.9}\text{Gd}_{0.1}\text{O}_{1.95}$  electrolyte powders were obtained from S.S.C. Inc., Woodinville, Washington. Electrolyte pellets were prepared by uniaxially pressing in a 13 mm diameter die. The pellet was subsequently isostatically pressed at a pressure of 350 MPa. The pellets were then sintered at 1500°C for 4 h. The density of the pellets exceeded 98% of the theoretical density.

The LSCF powders were prepared by the Pechini method [5]. Analar grade lanthanum, cobalt and ferric nitrates and strontium carbonate were dissolved in aqueous nitric acid. Citric acid and ethylene glycol were added in sufficient quantities to bind all the cations. After neutralisation with ammonium hydroxide, the solution was heated to 100°C to allow the polymerisation reaction to occur. The amorphous polymer gel was heated to 400°C to decompose the organics and nitrates and was then calcined at 800°C for 4 h. A portion of this calcined material was further calcined at 1000°C for 4 h. Electrode paints were prepared by ball milling the calcined LSCF powders with a polymer, plasticiser, surfactant and solvent. These paints were used to prepare electrodes on CGO pellets, which were then sintered for varying periods of time at 1000°C.

Some LSCF reference powders of varying composition were prepared by a glycine pyrolysis method [6]. These materials, which had been calcined at 1300°C, were more crystalline than the LSCF electrode powders and they were prepared to aid the interpretation of the X-ray diffraction data.

### 2.2. Structural characterisation

A Phillips PW1710 X-ray diffractometer using  $\text{CuK}_\alpha$  radiation was used to determine the structure

of the LSCF electrode powders, LSCF electrodes and the LSCF reference materials. A LINK EDS system fitted to a JEOL T200 scanning electron microscope was used to determine the bulk composition of the electrodes. Preliminary Fe K-edge X-ray absorption measurements have been made on station 7.1 of the SRS at Daresbury, to determine the room temperature oxidation states of iron in the 800 and 1000°C LSCF powders.

### 2.3. Electrical characterisation

AC impedance spectroscopy of the CGO pellets with LSCF electrodes were carried out using a Schlumberger 1260 frequency response analyser. The samples were held in a purpose built sample holder that fitted within a tube furnace. AC spectra in the frequency range of 1 mHz to 10 MHz were recorded with an RMS excitation voltage of 40 mV, in the temperature range of 300 to 900°C.

## 3. Results and discussion

The bulk composition of LSCF electrodes derived from LSCF powders calcined at 800°C and 1000°C are shown in Table 1. It is observed that the LSCF calcination temperature has little effect on their bulk composition and they are close to the compositions calculated from the metal nitrate and carbonate ratios used in their preparation.

The X-ray diffraction patterns of the calcined LSCF powders are shown in Fig. 1. The LSCF powders showed quite distinct diffraction patterns. The LSCF calcined at 800°C exhibited a pattern of a "high symmetry" perovskite that was either cubic or a slightly distorted pseudo-cubic phase (orthorhombic or tetragonal). A definite assignment of the crystal system was not possible because of the line

Table 1  
Bulk compositions of LSCF electrodes determined by EDS (Molar ratios)

Sample	La	Sr	Co	Fe
800°C LSCF	0.61	0.40	0.20	0.79
1000°C LSCF	0.60	0.41	0.21	0.80
LSCF-AS	0.60	0.13	0.20	0.74

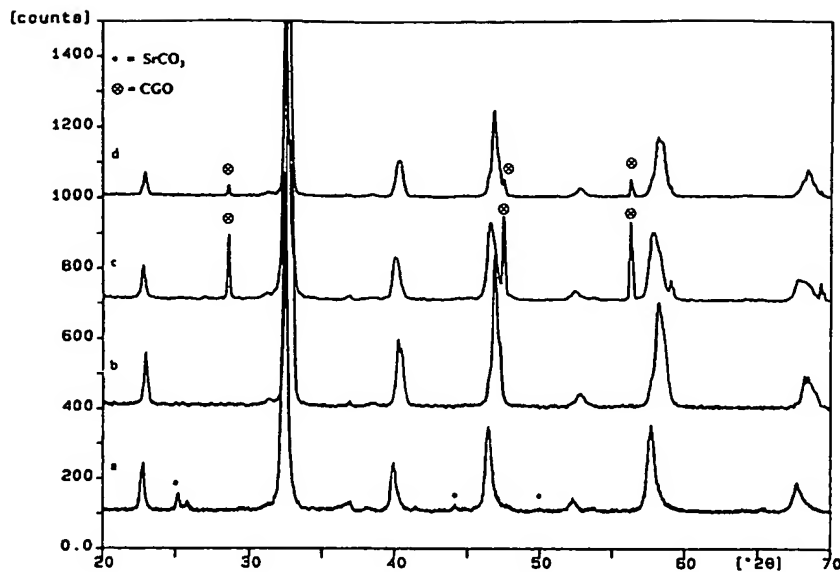


Fig. 1. X-ray diffraction patterns of LSCF powders and electrodes (a) and (b), calcined at 800 and 1000°C, respectively. (c) and (d), LSCF electrodes made from LSCF powders (a) and (b), respectively.

broadening and the presence of a secondary phase identified as strontium carbonate. The LSCF powder calcined at 1000°C consisted largely of a rhombohedrally distorted perovskite, which is consistent with the results of Anderson et al. [7]. A small proportion of the higher symmetry perovskite, as observed in the material calcined at 800°C, was present and was reflected in small shoulders on the low  $2\theta$  side of the rhombohedral perovskite. No strontium carbonate was observed but this was expected as it begins to decompose in the range of 950 to 1000°C [8].

X-ray diffraction patterns of electrodes prepared from the 800 and 1000°C powders by sintering onto CGO pellets at 1000°C for 4 h are also shown in Fig. 1. The 1000°C electrode has the rhombohedral perovskite structure. The electrode prepared from the 800°C powder consists of a mixture of the high symmetry perovskite, observed in the 800°C LSCF powder, and the rhombohedral perovskite. No strontium carbonate was observed.

We conclude that the LSCF powder and electrode that received the high temperature calcination and sintering treatment is a stoichiometric perovskite, incorporating all the cations that are present (e.g., with La/Sr/Co/Fe in a 6/4/2/8 mole ratio). The

800°C powder contains a quantity of strontium that is not incorporated into the perovskite lattice, in the form of strontium carbonate, suggesting that the high symmetry perovskite has an A-site deficiency.

A portion of the 800°C LSCF powder was soaked in dilute aqueous nitric acid to remove the strontium that was not incorporated into the perovskite structure. The EDS analysis of this acid soaked LSCF is reported in Table 1 as LSCF-AS. We observe that the La/Co ratio is very similar to that observed with the bulk LSCF electrodes. The iron content of the phase has decreased slightly. However, the main observation is that the strontium content of the phase is greatly reduced from  $\text{Sr}_{0.40}$  to  $\text{Sr}_{0.13}$ , giving it the composition  $\text{La}_{0.6}\text{Sr}_{0.13}\text{Co}_{0.2}\text{Fe}_{0.8}\text{O}_{3-\delta}$  (i.e., the perovskite phase is 27% A-site deficient). X-ray diffraction confirmed that the LSCF maintained the high symmetry perovskite structure after acid treatment (see Fig. 2(a)).

LSCF standards, with LSCF ratios of 6/4/2/8 and 6/1/2/8, were prepared by the glycine pyrolysis method and were then calcined at 1300°C to improve crystallinity. X-ray diffraction patterns of these LSCF standards are shown on Fig. 2 and the crystallographic data for these phases is summarised in Table 2. The 6/4/2/8 standard has the rhom-

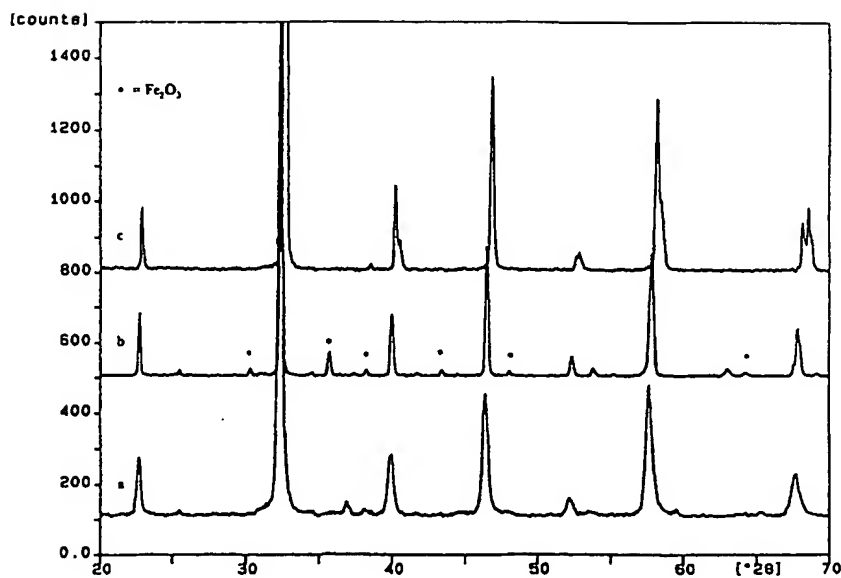


Fig. 2. X-ray diffraction patterns of (a) LSCF-AS, (b) LSCF 6/1/8/2 and (c) LSCF 6/4/8/2 (standards).

Table 2  
Crystallographic data for the 6/1/2/8 and 6/4/2/8 LSCF standards

Sample	Crystal system	<i>a</i> /Å	<i>c</i> /Å	Cell volume/Å <sup>3</sup>	Density/g.cm <sup>-3</sup>
LSCF 6/1/2/8	cubic	$3.906 \pm 0.004$		59.57	5.34
LSCF 6/4/2/8	rhombohedral*	$5.496 \pm 0.003$	$13.34 \pm 0.03$	349.1	6.36

\* = Hexagonal axes.

bohedral structure. The A-site deficient LSCF standard, with the 6/1/2/8 composition, is a cubic perovskite. The presence of a small quantity of  $\alpha$ - $\text{Fe}_2\text{O}_3$  indicates that the strontium content of 0.13, in the acid soaked LSCF powder, is close to the A-site deficiency stability limit, and attempts to synthesise a more A-site deficient phase (e.g.,  $\text{La}_{0.6}\text{Sr}_{0.1}\text{Co}_{0.2}\text{Fe}_{0.8}\text{O}_{3-\delta}$ ) leads to the loss of Fe from the B-site. Preliminary X-ray absorption spectroscopy of the iron K-edge of the 6/1/2/8 and 6/4/2/8 LSCF powders, at room temperature, suggests that the predominant oxidation state of the iron is 3+ indicating that the charge compensation mechanism in the A-site deficient perovskite is oxygen vacancies rather than a higher B-site cation valency.

Therefore, we conclude that a strontium deficient perovskite, with a cubic structure, crystallises from the amorphous precursor, along with strontium car-

bonate. Above 950°C, after the strontium carbonate has decomposed, Sr(II) diffuses into the bulk of the perovskite, producing a stoichiometric perovskite ( $\text{La}_{0.6}\text{Sr}_{0.4}\text{Co}_{0.2}\text{Fe}_{0.8}\text{O}_{3-\delta}$ ), with the rhombohedral structure. X-ray diffraction patterns of electrodes, produced from the cubic LSCF powder and sintered onto CGO pellets for varying periods of time are shown in Fig. 3, along with an electrode prepared from the rhombohedral LSCF powder. We observe that after sintering at 1000°C for 12 min, the LSCF electrode is still largely a cubic phase along with a lesser quantity of rhombohedral LSCF. As the sintering time is lengthened, the proportion of the LSCF with the rhombohedral perovskite structure increases.

The areal electrode resistance of the LSCF electrodes, after different sintering treatments, is shown in Fig. 4. We observe that the LSCF prepared from the LSCF powder calcined at low temperature (800°C) and sintered for the shortest period of time

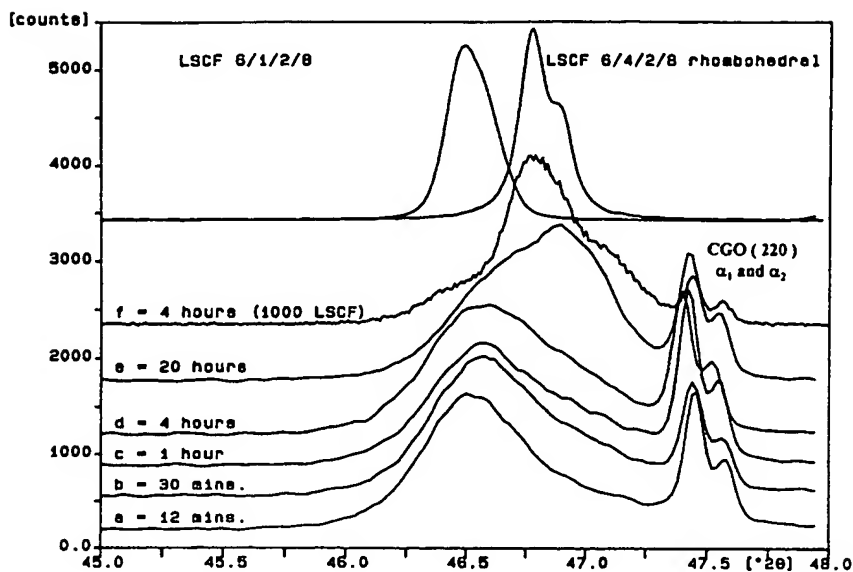


Fig. 3. X-ray diffraction patterns of the LSCF electrodes as a function of sintering time. (a) to (e) derived from LSCF calcined at 800°C and (f) derived from LSCF calcined at 1000°C.

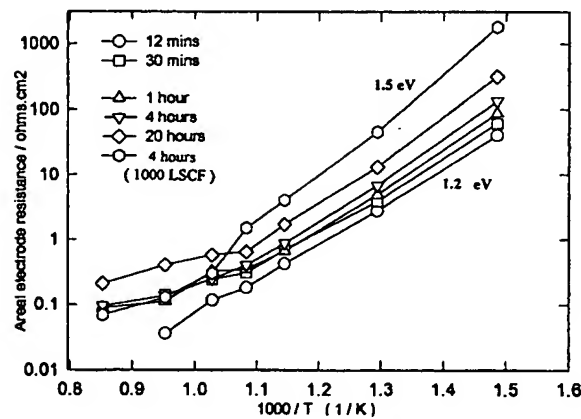


Fig. 4. Areal electrode resistance of LSCF electrodes as a function of sintering time.

(12 min) has both the lowest electrode resistance and activation energy. Longer sintering times of this electrode leads to increases in the electrode resistances and activation energies. The resistance of the LSCF electrode prepared at high temperature (1000°C) was found to be the highest and both the resistance values and the activation energies were comparable to the literature values of

$\text{La}_{0.6}\text{Ca}_{0.4}\text{Co}_{0.2}\text{Fe}_{0.8}\text{O}_{3-\delta}$  electrodes sintered onto  $\text{Ce}_{0.9}\text{Sm}_{0.1}\text{O}_{1.95}$  at high temperatures [9].

#### 4. Conclusions

We have shown that the thermal history of LSCF electrodes can have a profound effect on their composition and performance. We have demonstrated that lanthanum strontium iron cobalt perovskites can accommodate a large degree of A-site deficiency ( $\approx 27\%$ ) and that this A-site deficiency leads to a change in the perovskite symmetry from rhombohedral, in the stoichiometric perovskite, to cubic in the A-site deficient perovskite. A substantial decrease in the resistance of electrodes derived from the A-site deficient perovskites was observed. There is evidence that the charge compensation mechanism is due to oxygen vacancies. We intend to investigate the reasons for the improvement in the performance of the A-site deficient LSCF electrodes using  $\text{O}^{18}$  isotope exchange to determine the oxygen diffusion coefficient and the surface exchange coefficient and dc and TGA measurements to obtain the electrical and oxygen content, respectively. We also intend to carry in-situ X-ray absorption measurements at ele-

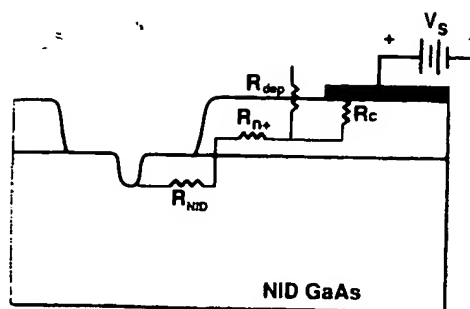
vated temperatures to determine the iron and cobalt oxidation states and local coordination in the environment envisaged for an operational oxygen separation membrane.

### Acknowledgments

I would like to thank EPSRC for financial support for this work and Dr J. McAleese for carrying out the EDS analysis of the LSCF materials.

### References

- [1] D.B. Meadowcroft, *Nature (London)* 226 (1970) 847.
- [2] L.W. Tau, M.M. Nasrallah and H.U. Anderson, Proc. 3rd Int. Symp. on SOFC., S.C. Singhal and H. Iwahara, eds., 183rd Electrochemistry Meeting (Electrochem. Soc., NJ, 1993) p. 241.
- [3] C.C. Chen, M.M. Nasrallah and H.U. Anderson, Proc. 3rd Int. Symp. on SOFC., S.C. Singhal and H. Iwahara, eds., 183rd Electrochemistry Meeting (Electrochem. Soc., NJ, 1993) p. 252.
- [4] D. Waller, J.A. Kilner and B.C.H. Steele, 1st Int. Symp. on Ceramic Membranes, 188th Electrochemistry Meeting (Electrochem. Soc., Chicago, 1995).
- [5] M. Pechini, U.S. patent 3 330 697, July 11 (1967).
- [6] L.A. Chick, L.R. Pederson, G.D. Maupin, J.L. Bates, L.E. Thomas and G.J. Exarhos, *Materials Letters* 10 (1990) 6.
- [7] H.U. Anderson, L.-W. Tai, C.C. Chen, M.M. Nasrallah and W. Huebner, Proc. 4th Int. Symp. on SOFC, Yokahama, 1995, p. 375.
- [8] C. Beck, *American Mineralogist* 35 (1950) 985.
- [9] J.A. Lane, H. Fox, B.C.H. Steele and J.A. Kilner, *Electroceramics: Production, Properties and Microstructure*, W.E. Lee and A. Bell, eds. (British Ceramic Proc., 1994) Vol. 52, p. 264.

Fig. 7. Schematic cross section of  $n^+$ /NID structure with resistances.

gible.  $R_{NID}$  and  $R_{n^+}$  are roughly proportional to the product of the resistivity of the material times the path length of the carriers in the particular material. That is

$$R_{NID} \propto \rho_{NID} \times L_{NID}$$

$$R_{n^+} \propto \rho_{n^+} \times L_{n^+}$$

As the etch proceeds, however, the relative contribution of  $R_{NID}$  increases, diminishing the current, and hence the etch rate. In the limit, of course, the situation approaches that of etching NID GaAs alone. That is, as the pathlength in the NID material increases, the effect of the  $n^+$  layer becomes negligible. Therefore, the etching of the NID GaAs saturates at some depth, as observed in Fig. 6. The lateral etching of the  $n^+$  GaAs promotes this effect by increasing the effective current path in the NID GaAs, and therefore increasing the relative contribution of  $R_{NID}$  to the total resistance. There is then the qualitatively inverse relationship between limiting etched depth in the NID GaAs substrate and the laterally etched radius in the  $n^+$  overlayer.

#### Conclusion

We have observed that the etch behavior of a material can change significantly when it is embedded in a doped homostructure. Extremely high etch selectivities were

found for an  $n^+$  GaAs layer on a  $p^+$  GaAs substrate, regardless of applied bias. The results were in accordance with values extrapolated from the individually measured bulk etch rates. However, only limited selectivities were observed for  $n^+$  GaAs on a NID GaAs substrate. While bulk NID GaAs alone etched less than 5 Å/min, etched depths of as great as 6  $\mu\text{m}$  were achieved after 20 min of etching into the  $n^+$ /NID GaAs homostructure. The nature of the band bending at the etch pit/electrolyte interface was the major determinant in the etching of the  $n^+$  on  $p^+$  GaAs homostructure, as found for the bulk materials. We believe that the  $n^+$  overlayer of the  $n^+$ /NID GaAs structure serves to increase the transport of the photogenerated electrons to the cathode, where the reduction reactions take place. The increased electron current implies an increased anodic dissolution or NID GaAs etch rate.

#### Acknowledgments

The authors would like to thank Randy Geels for the growth of the samples and John Bowers, Greg Snider, and David Lishan for helpful discussions. This work was supported by the Xerox Corporation through the California Micro-Program.

Manuscript submitted July 27, 1990; revised manuscript received Nov. 26, 1990.

*The University of California, Santa Barbara, assisted in meeting the publication costs of this article.*

#### REFERENCES

1. J. van de Ven and H. J. P. Nabben, *This Journal*, **137**, 1603 (1990).
2. R. W. Haisty, *ibid.*, **108**, 790 (1961).
3. F. Kuhn-Kuhnenfeld, *ibid.*, **119**, 1063 (1972).
4. J. van de Ven and H. J. P. Nabben, *J. Appl. Phys.*, **67**, 12 (1990).
5. R. M. Osgood Jr., A. Sanchez-Rubio, D. J. Ehrlich, and V. Daneu, *Appl. Phys. Lett.*, **40**, 391 (1982).
6. G. C. Tisone and A. W. Johnson, *ibid.*, **42**, 530 (1983).
7. F. W. Ostermayer and P. A. Kohl, *ibid.*, **39**, 76 (1981).
8. M. N. Ruberto, A. E. Willner, D. V. Podlesnik, and R. M. Osgood, Jr., *ibid.*, **55**, 10 (1989).

## Changes in the Phases and Electrical Conduction Properties of $(\text{La}_{1-x}\text{Sr}_x)_{1-y}\text{MnO}_{3-\delta}$

Shoji Otoshi, Hirokazu Sasaki, Hisao Ohnishi, Minoru Hase, Kimio Ishimaru, and Masamichi Ippommatsu

Osaka Gas Company, Limited, Fundamental Research Laboratories, Konohana-ku, Osaka 554, Japan

Takamitsu Higuchi, Masaru Miyayama, and Hiroaki Yanagida

Research Center for Advanced Science and Technology, University of Tokyo, Meguro-ku, Tokyo 153, Japan

#### ABSTRACT

Perovskite oxides  $(\text{La}_{1-x}\text{Sr}_x)_{1-y}\text{MnO}_{3-\delta}$ ,  $[(\text{La}_{1-x}\text{Sr}_x)_{0.94}\text{MnO}_{3-\delta}]$  ( $0.08 \leq x \leq 0.30$ ) and  $(\text{La}_{0.89}\text{Sr}_{0.11})_{1-y}\text{MnO}_{3-\delta}$ , ( $0.06 < y < 0.11$ ) containing A site defects were studied by thermal analysis, measuring of the temperature dependence of electrical conductivity (373-1273 K) and x-ray diffraction. The results showed that  $(\text{La}_{1-x}\text{Sr}_x)_{0.94}\text{MnO}_{3-\delta}$  ( $0.08 \leq x \leq 0.21$ ) underwent a phase transition accompanied by oxygen desorption at about 1000 K in air. The electrical conduction mechanism also changed from small-polaron conduction. The amount of oxygen desorption accompanying the phase transition decreased stoichiometrically with increasing Sr content.

Global environmental problems, such as the warming of the earth due to the increase in  $\text{CO}_2$  levels in the atmosphere and the destruction of forests by acid rain resulting from  $\text{SO}_2$  and  $\text{NO}_x$ , have recently become factors affecting the growth of the world economy.

To reduce these problems, the efficient and clean use of energy is essential and hence the importance of developing a fuel cell expected to have 40-60% generating efficiency and 80-90% combined efficiency with little  $\text{NO}_x$

emission has increased. Studies on solid electrolyte fuel cells (SOFC) with a high generating efficiency and high exhaust heat recovery temperature are particularly important.

$\text{LaMnO}_3$  and  $\text{LaCoO}_3$  systems have been considered for the cathode materials, and in particular, Sr or Ca doped  $\text{LaMnO}_3$  has been highly rated (1) because (i) it has approximately the same coefficient of thermal expansion as  $\text{Y}_2\text{O}_3$  stabilized  $\text{ZrO}_2$  (YSZ), the electrolyte, (ii) it is unreactive at

1300 K in air even in the presence of YSZ, and (iii) it has electrode properties as well as a practical level of electrical conductivity. Doped Sr generated Sr<sup>+</sup>La and holes.

Shimoyama *et al.* (2) found that in LaMnO<sub>3</sub> oxides, a phase with La vacancies at the A site was stable in air and compounds with the A site defect underwent a phase change accompanied by oxygen desorption at around 800–1500 K. Yokokawa *et al.* (3), by conducting thermodynamic analysis, showed that the La deficiency had to be within a certain range in order to prevent the formation of a La<sub>2</sub>Zr<sub>2</sub>O<sub>7</sub> layer resulting from the reaction between LaMnO<sub>3</sub> and ZrO<sub>2</sub>. Although for LaMnO<sub>3</sub> electrodes, the nonstoichiometry of La at the A site and Mn at the B site is very important, as shown above, no detailed analysis of the phase change and the accompanying change in electrical properties of A site deficient LaMnO<sub>3</sub> has been made.

In this study the authors investigated the relationship between the change in oxygen nonstoichiometry and electrical conduction by changing the A site deficiency and Sr doping of A site deficient LaMnO<sub>3</sub> [(La<sub>1-x</sub>Sr<sub>x</sub>)<sub>1-y</sub>MnO<sub>3-y</sub>] and found changes in the electrical conduction mechanism which were thought to result from a phase transition (change in oxygen nonstoichiometry), reported below.

### Experimental Procedures

La<sub>2</sub>O<sub>3</sub>, SrCO<sub>3</sub>, and MnCO<sub>3</sub> (Rare Metallic Corporation; purity, 99.99%) were used as starting materials. They were reacted in the required proportions (water content adjusted by ICP) by mixing thoroughly in an agate mortar, grinding after being calcined at 1273 K in air for 15 h and further fired at 1573 K in air for 48 h, to obtain La<sub>1-x</sub>Sr<sub>x</sub>)<sub>1-y</sub>MnO<sub>3-y</sub> powder. The powder was ground and molded under 250 kg/cm<sup>2</sup> to 1 t/cm<sup>2</sup> using a uniaxial press and sintered at 1573 K for 24 h in air to prepare pellets for measuring the electrical conductivity. The composition of the powders obtained was confirmed with ICP by dissolving the sample in hydrochloric acid. To analyze the crystal structure, the ordinary powder x-ray diffraction method was used. Thermogravimetric measurements were conducted at a temperature increase rate of 10°C/min using a TGR-50 thermobalance manufactured by Shimadzu Corporation.

Electrical conductivity measurements were conducted in an electric furnace using the dc four-terminal method. The contact between the sample and electrodes was ohmic.

### Experimental Results and Discussion

**Crystal structure analysis.**—The crystal structures of six samples of (La<sub>1-x</sub>Sr<sub>x</sub>)<sub>0.94</sub>MnO<sub>3-y</sub> with x = 0.08, 0.11, 0.14, 0.17, 0.21, and 0.30 were investigated. The results showed that four samples with x = 0.08 to 0.17 were all single phases having almost identical hexagonal or rhombohedral structures. As a typical example of this, Fig. 1a shows the x-ray diffraction pattern of the sample with x = 0.11. In the case of x = 0.30, as shown in Fig. 1b, improved symmetry was clearly seen with the crystal form closer to a cubic system. With x = 0.20 as shown in Fig. 1c the structure was an intermediate between the above two. The crystal structures of seven samples of (La<sub>0.98</sub>Sr<sub>0.1</sub>)<sub>1-y</sub>MnO<sub>3-y</sub> with y = 0.15, 0.11, 0.09, 0.06, 0.03, 0.00, and -0.04 were investigated, but four samples with y = 0.15 and y = 0.03 to -0.04 were not used in this study because Mn<sub>2</sub>O<sub>3</sub> separated in the case of y = 0.15 while La<sub>2</sub>O<sub>3</sub> separated in the case of y = 0.03 to -0.04. For samples with y = 0.11–0.06, nearly the same results were obtained as for the y = 0.06 sample shown in Fig. 1a.

For brevity the sample used will be described by the abbreviations shown in Table I.

**Thermogravimetric analysis.**—Figure 2a shows the results of the thermogravimetric analysis of sample B. The results show a decrease in weight due to oxygen desorption in the vicinity of 1023 K and above, which agrees well with the results obtained by Mizusaki *et al.* for the system without doped Sr (4). Using x-ray diffraction measurements, Higuchi *et al.* (5) found that the cell constant changes with the change due to oxygen desorption. When the same experiments were conducted on samples A, B, C,

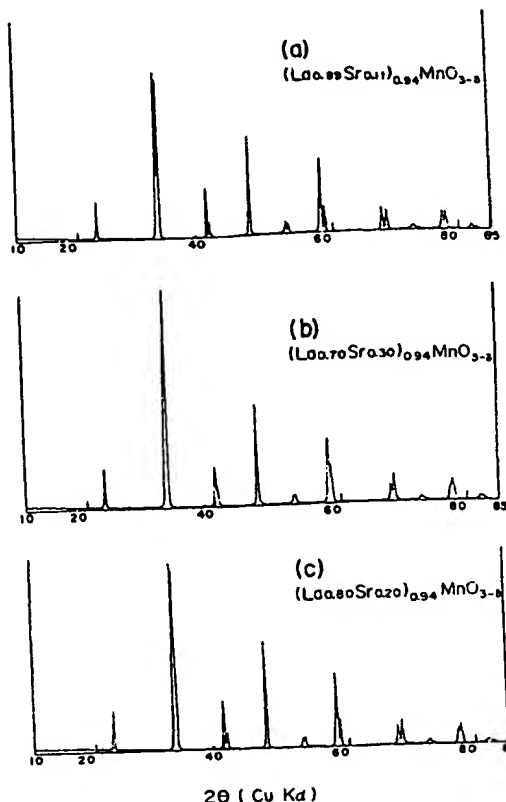
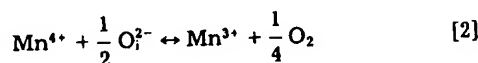
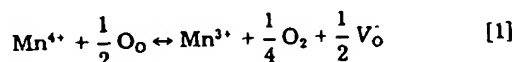


Fig. 1. XRD spectra of (La<sub>1-x</sub>Sr<sub>x</sub>)<sub>1-y</sub>MnO<sub>3-y</sub> at room temperature.

D, E, and F with varying Sr doping, the desorbed oxygen amount decreased with the increase in doped Sr content and for sample F, no oxygen desorption was seen, as shown by Fig. 2b. Figure 3 shows the results of the experiments illustrating the relationship between the Sr content and the amount of desorbed oxygen. As is clearly seen, there is a good linear relationship between the two values, with a gradient of about 0.5.

Several models on the nonstoichiometry of LaSrMnO<sub>x</sub> have been suggested (4, 6), but this relation has not been clarified. We propose the following model to explain the experimental results. From electrical neutrality conditions, it is obvious that oxygen desorption is accompanied by a change in Mn valence. The amount of Mn<sup>4+</sup> is determined by Eq. [1] and [2]



where V<sub>0</sub> is oxygen vacancy, O<sub>0</sub> is oxygen ion at lattice point, and O<sub>i</sub> is oxygen ion within the lattice.

In the problem of Mn reduction and oxidation, these equations are equal to the equations reported by Kuo *et al.* (8). From Eq. [1] and [2] the number of desorbed oxygen atoms is equal to half of the change in Mn<sup>4+</sup> amount.

Table I. Sample list.

Symbol	Chemical contents	d/d <sub>th</sub>
A	(La <sub>0.92</sub> Sr <sub>0.08</sub> ) <sub>0.94</sub> MnO <sub>3-y</sub>	0.59
B	(La <sub>0.90</sub> Sr <sub>0.11</sub> ) <sub>0.94</sub> MnO <sub>3-y</sub>	0.60
C	(La <sub>0.88</sub> Sr <sub>0.14</sub> ) <sub>0.94</sub> MnO <sub>3-y</sub>	0.59
D	(La <sub>0.93</sub> Sr <sub>0.17</sub> ) <sub>0.94</sub> MnO <sub>3-y</sub>	0.58
E	(La <sub>0.70</sub> Sr <sub>0.21</sub> ) <sub>0.94</sub> MnO <sub>3-y</sub>	0.55
F	(La <sub>0.70</sub> Sr <sub>0.30</sub> ) <sub>0.94</sub> MnO <sub>3-y</sub>	0.51
G	(La <sub>0.80</sub> Sr <sub>0.11</sub> ) <sub>0.91</sub> MnO <sub>3-y</sub>	0.67
H	(La <sub>0.90</sub> Sr <sub>0.11</sub> ) <sub>0.89</sub> MnO <sub>3-y</sub>	0.69

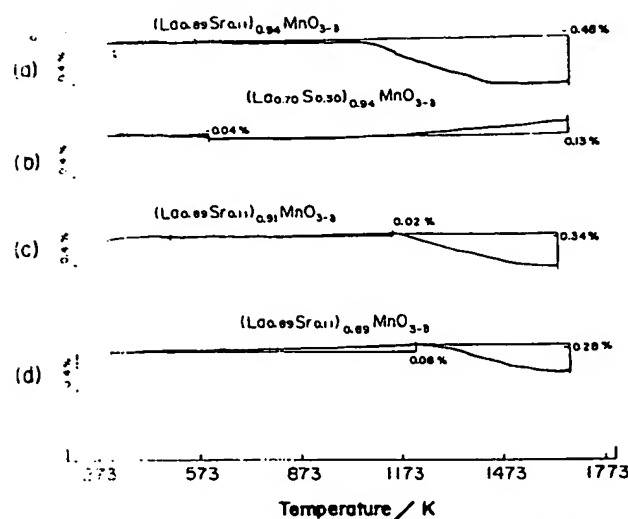


Fig. 2. TG spectra of  $(La_{1-x}Sr_x)_{0.94}MnO_{3-\delta}$  in air: (a) sample B, (b) sample F, (c) sample G, (d) sample H.

In the low-temperature phase, crystal strain energy is decreased by  $Mn^{4+}$ , which is smaller than  $Mn^{3+}$ . Strain energy is independent of the amount of doped Sr because the  $Sr^{2+}$  ion radius is nearly equal to  $La^{3+}$ . The amount of  $Mn^{4+}$  at low temperature is constant, independent of the amount of doped Sr. In the high-temperature phase, the amount of  $Mn^{4+}$  is determined by the holes generated by Sr doping.

Here, on the basis of the above assumptions, the sum of doped Sr and the decrease in  $Mn^{4+}$  due to the change from the low-temperature phase to the high-temperature phase are equal. Therefore, the decrease in the number of desorbed oxygen atoms is half of the number of doped Sr atoms. Hence, these assumptions allow a reasonable explanation of the experimental results in Fig. 3. Furthermore, these assumptions can explain the experimental results of sample F which is highly doped by Sr, because the amount of  $Mn^{4+}$  is determined by the electrical neutrality condition even in the low-temperature phase. These assumptions are supported by the results of the iodometry analysis obtained by Higuchi *et al.* (5).

Figure 2c and d show the results of thermal analysis of samples G, H with larger A site deficiencies. As shown by the results, the phase transition starting temperature in-

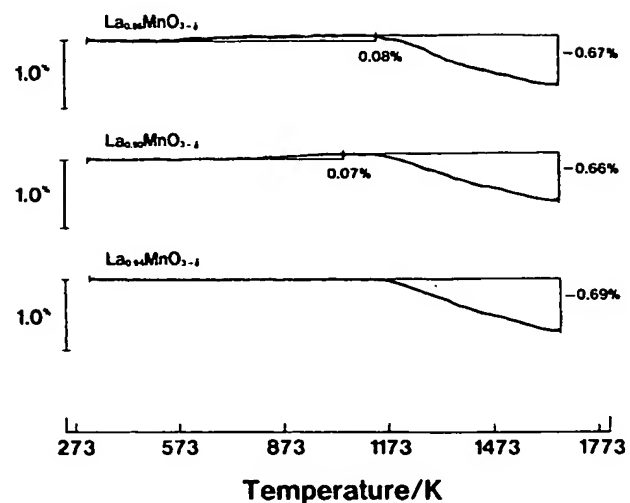


Fig. 4. TG spectra of  $La_{1-x}MnO_{3-\delta}$  after annealing at 1073 K for one week.

creased and the desorbed oxygen amount decreased with an increase in the A site deficiencies. We have proposed two models to explain these phenomena:

Model 1. Oxygen vacancies were stabilized by the interaction between the A site vacancies and the oxygen vacancies. Therefore, the oxygen desorption decreased with the stabilization of oxygen vacancies for the low temperature phase as well.

Model 2. The diffusion rate of oxygen into the bulk decreased with the increase in A site vacancies, and the uptake rate of oxygen decreased accordingly during the process of cooling the sample with a large number of A site vacancies. That is, specimens at low temperatures have low oxygen concentrations corresponding to those at higher temperatures.

In order to verify these two models, a thermogravimetric analysis of the sample which was obtained by rapid cooling in an air atmosphere after annealing in air at 1073 K for one week was carried out. The measurements were made on samples without Sr to simplify the discussion. As shown in Fig. 4, the quantity of desorbed oxygen was independent of the number of A site defects. However, the desorption starting temperature increased as the A site defects increased. From these results it was evident that differences in the amount of oxygen desorption and desorption temperature in relationship to A site defects in gradually cooled samples depended on differences in the oxygen diffusion rate in crystals. Results similar to Fig. 3 were obtained in samples whose A site defects were fixed and the doped Sr amount was varied.

**Temperature dependence of electrical conductivity.**—Figure 5a shows the temperature dependence of electrical conductivity,  $\sigma$ , of sample A. The ordinate represents the logarithm of the product of electrical conductivity and absolute temperature  $T$  and the abscissa represents the reciprocal of the absolute temperature. There is a linear relationship between  $\log(\sigma T)$  and  $1/T$  in the range 423–973 K, suggesting that the small-polaron conduction mechanism is dominant (7). In contrast, above 1073 K this relationship does not hold. To clarify the behavior above 1073 K, the results were plotted with  $\log \sigma$  on the ordinate and  $1/T$  on the abscissa as shown in Fig. 5b. This figure reveals that in contrast to the case below 973 K, electrical conductivity depends little on the temperature, like metallic conduction. The temperature at which the conduction mechanism changed coincides with the starting temperature of the phase transition. Experiments were made on samples B, C, D, and E whose phase transition starting temperatures are in the range 973–1073 K, as in the case of sample A. Electrical conductivity behavior similar to that of sample A was obtained. No such change in electronic conductivity has been found in other studies, for example, the study by Kertesz *et al.* (8) for samples without A site defects. As a counter experiment, electrical conductivity

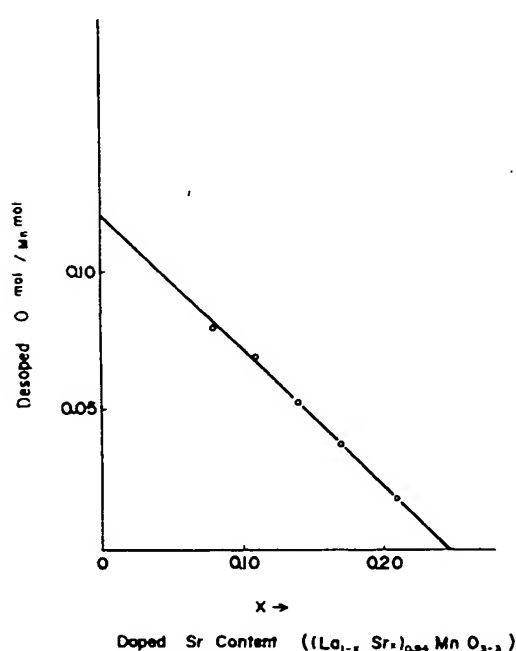


Fig. 3. Desorbed O molecule as a function of doped Sr content in  $(La_{1-x}Sr_x)_{0.94}MnO_{3-\delta}$  between 900 and 1650 K.

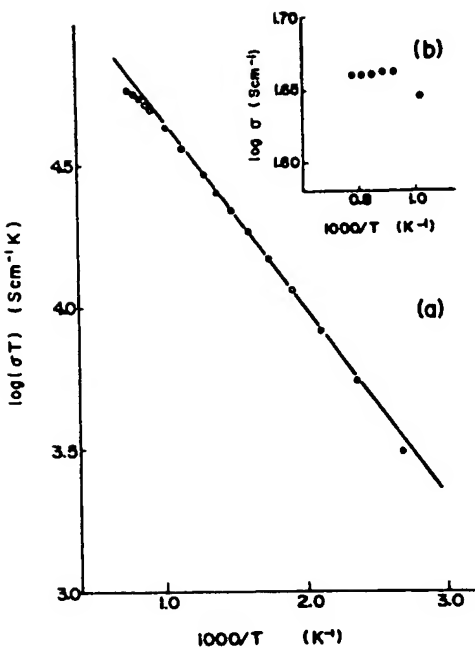


Fig. 5. Temperature dependence of the conductivity of  $(La_{0.92}Sr_{0.08})_{0.94}MnO_{3-\delta}$  (sample A).

was measured for high-density samples ( $d/d_{th} = 0.9$ ) with the same composition as sample B. As shown in Fig. 6, there was a linear relationship between  $\log(\sigma T)$  and  $1/T$  throughout the entire range measured in this sample, and no change in the conduction mechanism was observed. Based on this result, it is assumed that no oxygen desorption occurred in the high density samples either during the sintering process or during the measuring process due to the low oxygen diffusion. Figure 7a shows the temperature dependence of the electrical conductivity of sample F with a low density which underwent no phase transition. The figure reveals that a linear relationship exists between  $\log(\sigma T)$  and  $1/T$  over the range of temperatures 373-1273 K. Figure 8 shows the temperature dependence of the electrical conductivity of sample H containing a large number of A site defects. The figure shows that in sample H the con-

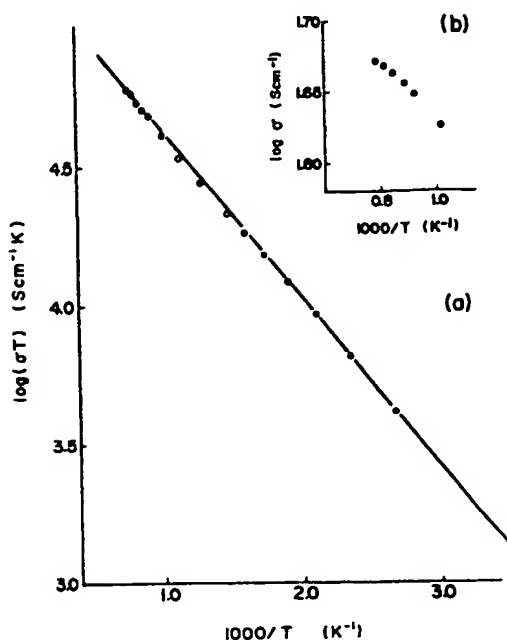


Fig. 7. Temperature dependence of the conductivity of  $(La_{0.70}Sr_{0.19})_{0.89}MnO_{3-\delta}$  (sample F).

duction mechanism changes from small-polaron conduction in the range of 1173-1223 K. This coincides with the starting temperature of the phase transition of sample H in Fig. 2d. For sample G, almost the same results were obtained as for sample H.

To summarize the above results for all the samples, except the high density sample, there was good agreement between the starting temperatures of the phase transition and the temperatures at which the conduction behavior changed. Thus, the results suggest that a change in the conduction mechanism of  $(La_{1-x}Sr_x)_{1-x}MnO_{3-\delta}$  above 1000 K occurs at the phase transition accompanied by oxygen desorption shown in Fig. 2.

The desorption rate of oxygen is found to be dependent on the relative density of the sintered specimen. This effect is important for industrial use.

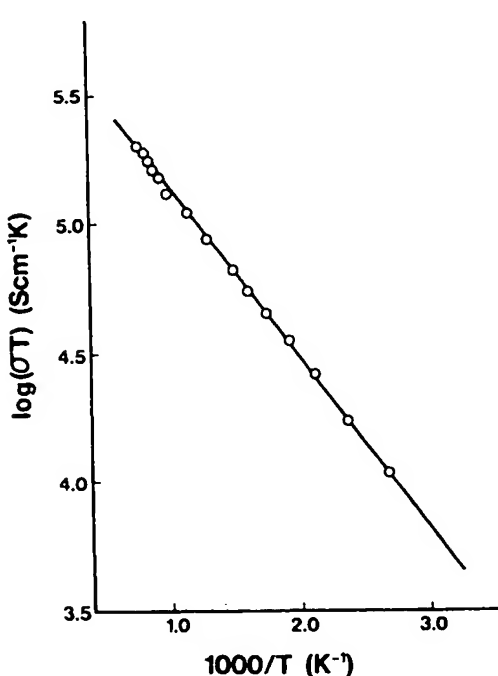


Fig. 6. Temperature dependence of the conductivity of high density  $(La_{0.88}Sr_{0.11})_{0.89}MnO_{3-\delta}$  ( $d/d_{th} = 0.90$ ).

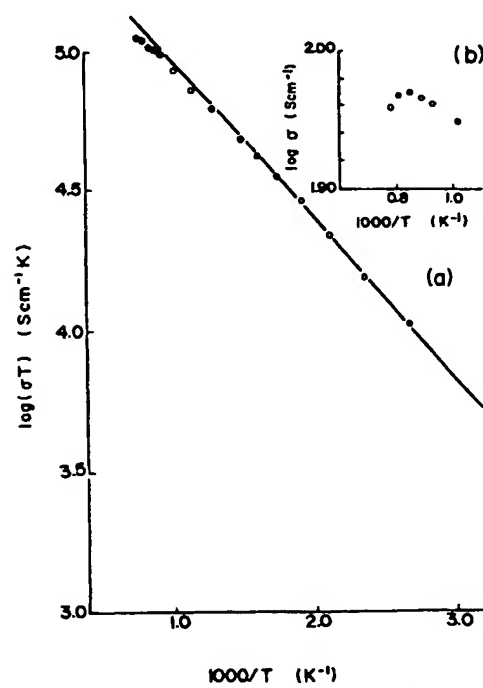


Fig. 8. Temperature dependence of the conductivity of  $(La_{0.75}Sr_{0.19})_{0.89}MnO_{3-\delta}$  (sample H).

Manuscript submitted Feb. 12, 1990; revised manuscript received Dec. 4, 1990.

Osaka Gas Company, Limited, assisted in meeting the publication costs of this article.

#### REFERENCES

1. T. Nakanishi, *Ceram. Bull. Soc. Jpn.*, **25**, 614 (1990).
2. J. Shimoyama, J. Mizusaki, and K. Fueki, in "Proceedings of 53th Chemical Society of Japan," I-263 (1988).
3. H. Yokokawa, N. Sasaki, T. Kawata, and M. Dokya, *Denki Kagaku*, **57**, 829 (1989).
4. J. Mizusaki and H. Tagawa, in "Proceedings of SOFC-Nagoya," p. 65 (1989).
5. T. Higuchi, M. Miyayama, H. Yanagida, S. Ohtoshi, H. Ohnishi, S. Sasaki, K. Ishimaru, and M. Ippommatsu, To be published.
6. J. H. Kuo, H. U. Anderson, and D. M. Sparlin, *J. Solid State Chem.*, **83**, 52 (1989).
7. D. P. Karim and A. T. Aldred, *Phys. Rev. B*, **20**, 2255 (1979).
8. M. Kertesz, I. Riess, and D. S. Tannhauser, *J. Solid State Chem.*, **42**, 125 (1989).

## A Mathematical Model for Chemical Vapor Deposition Processes Influenced by Surface Reaction Kinetics: Application to Low-Pressure Deposition of Tungsten

Rikhit Arora\* and Richard Pollard\*\*

Department of Chemical Engineering, University of Houston, Houston, Texas 77204-4792

#### ABSTRACT

A model for the simultaneous reaction kinetics and transport processes in chemical vapor deposition (CVD) reactors has been extended to treat deposition of materials that have a broad range of surface characteristics, e.g., sites with multiple dangling bonds and adsorbates with multiple bonding configurations. The model uses the nature of the surface to determine the elementary processes that can take place during growth. Rate constants for these processes are calculated from first principles using statistical thermodynamics, transition state theory, and bond dissociation enthalpies. In this way, deposition rates are determined without either assuming the reaction mechanism or arbitrarily choosing any kinetic parameter values. The utility of the approach is illustrated by modeling low-pressure CVD of tungsten from tungsten hexafluoride and hydrogen. The treatment considers 14 species and eight reactions in the gas together with 21 species and 65 processes at the surface. The calculations indicate that, for the range of operating conditions considered, the process is controlled by surface reaction kinetics and that gas-phase reactions are unimportant. Deposition rates and surface fluxes predicted by the model show quantitative agreement with available experimental data. In addition, the major reaction pathways and rate-limiting steps are identified. This information is used to develop simplified rate expressions (still without using any fitted rate constants) that give reasonable predictions for the growth rate. Sensitivity studies are performed to assess the impact of uncertainties in species properties and rate constants on the theoretical results.

Many models have been developed to help improve our understanding of chemical vapor deposition (CVD) processes. Examples range from analytic expressions for diffusion across a boundary layer (1) to computer codes for multidimensional heat, mass, and momentum transport (2). Some studies (3) have included elementary gas-phase reactions but, up until now, the rates of surface reactions have been determined empirically, i.e., using overall or lumped reactions and choosing kinetic parameter values to give deposition rates that match experimental results. This approach to the surface kinetics may be adequate for systems that are controlled primarily by rates of diffusion or gas-phase decomposition. However, for processes where surface reactions play a significant role, questions arise concerning the uniqueness of an empirical kinetic model and its ability to describe the system behavior outside the range of operating conditions for which data are already available. Therefore, a more fundamental approach is needed to describe the kinetics of heterogeneous reactions in CVD, especially since there is a trend towards operating at lower pressures and temperatures where surface processes tend to be more important.

Recently, a CVD model has been developed that uses statistical mechanics, transition state theory, and bond dissociation enthalpies to obtain the rate constants for elementary processes in the gas phase and at the growing surface (4, 5). The calculations treat the many plausible simultaneous chemical reactions and the finite rates of adsorption and desorption on different types of sites as well as the fluid flow of the gas mixture and multicomponent heat and mass transport. In this way, major reaction path-

ways are predicted rather than assumed and local compositions, deposition rates, and rate-limiting factors are determined without arbitrarily choosing the values for any rate constants. Previously, application of the model to metalorganic vapor-phase epitaxy of GaAs provided considerable insight into the system behavior and yielded growth rates that agree quantitatively with available experimental data (4, 5).

In this paper, the treatment of elementary surface processes in the model is generalized to give rate equations that can be applied to a broader spectrum of CVD systems. For example, effects associated with the availability of more than one dangling bond per surface site are taken into consideration as well as the ability of a given species to adsorb in several different bonding configurations and the possibility of steric hindrance. The utility of the extended CVD model is illustrated by considering low pressure deposition of tungsten using  $WF_6$  and  $H_2$  as reactants. Interest in this material for contacts and interconnects in VLSI circuits stems from its high conductivity and high melting point and its compatibility with silicon (6, 7).

The model for CVD of tungsten includes 14 species and eight reactions in the gas phase and 21 species and 65 elementary processes at the surface. Theoretical predictions are compared with experimental data for a wide range of operating conditions and the rate-controlling steps and dominant intermediate species are identified. Sensitivity studies are used to assess the impact of uncertainties in species properties and rate constants on the predicted deposition rates. Furthermore, results from the complete model are used to obtain simplified kinetic expressions that yield accurate predictions for the deposition rate and that still use parameter values determined from first principles.

\* Electrochemical Society Student Member.

\*\* Electrochemical Society Active Member.

## Development of lanthanum ferrite SOFC cathodes

S.P. Simner\*, J.F. Bonnett, N.L. Canfield, K.D. Meinhart, J.P. Shelton, V.L. Sprenkle, J.W. Stevenson

Materials Sciences Department, Pacific Northwest National Laboratory, 902 Battelle Boulevard, P.O. Box 999, Richland, WA 99352, USA

Received 9 August 2002; accepted 18 August 2002

### Abstract

A number of studies have been conducted concerning compositional/microstructural modifications of a Sr-doped lanthanum ferrite (LSF) cathode and protective Sm-doped ceria (SDC) layer in an anode supported solid oxide fuel cell (SOFC). Emphasis was placed on achieving enhanced low temperature (700–800 °C) performance, and long-term cell stability. Investigations involved manipulation of the lanthanum ferrite chemistry, addition of noble metal oxygen reduction catalysts, incorporation of active cathode layer compositions containing Co, Fe and higher Sr contents, and attempts to optimize the ceria barrier layer between the LSF cathode and YSZ electrolyte.

© 2002 Elsevier Science B.V. All rights reserved.

**Keywords:** SOFC; Lanthanum ferrite; SDC

### 1. Introduction

The purpose of this paper is to detail recent investigations at Pacific Northwest National Laboratory (PNNL) directed towards the improved lower temperature (700–800 °C) performance of anode-supported solid oxide fuel cells (SOFCs) by optimizing the cathode and its interfaces. It is widely established that the performance of low-temperature SOFCs is highly dependent on cathode polarization losses, which must be minimized to optimize the SOFC power densities. In our own research  $\text{La}_{0.8}\text{Sr}_{0.2}\text{FeO}_{3-\delta}$  (LSF-20) has demonstrated high power outputs ( $\sim 0.9$ – $0.95 \text{ W/cm}^2$  at  $750^\circ\text{C}$ /0.7 V), and good long-term stability [1]. It should be noted that the aforementioned performance is atypical, and a more consistent, reproducible power value is  $0.75$ – $0.8 \text{ W/cm}^2$  ( $750^\circ\text{C}$ /0.7 V). The exact phenomena behind the inconsistencies have not been precisely established, though this subject and possible explanations will be considered throughout the text. Other perovskite compositions previously considered at PNNL with Co, Ni and Mn B-site cations have indicated either poor chemical, and long-term performance stability, or the materials simply exhibited lower power densities than our optimized LSF cathode. Therefore, most of the recent cathode research efforts at PNNL have been directed towards LSF. This present study

predominantly considers non-stoichiometric LSF-20 compositions,  $(\text{La}_{0.8}\text{Sr}_{0.2})_x\text{FeO}_{3-\delta}$  ( $x = 0.95$ – $1.05$ ), the addition of second phases to the LSF (in particular ceria and noble metals), and optimization of the relevant microstructures and interfaces in an attempt to enhance the ultimate cell performance and longevity.

### 2. Experimental

Anode ( $\text{NiO}$ –YSZ)–electrolyte (YSZ) substrate samples were produced via standard organic tape casting and tape lamination procedures, co-sintered at  $1375^\circ\text{C}$  for 1 h, and subsequently creep-flattened at  $1350^\circ\text{C}$  for 2 h. The post-sintered/post-reduced anode ( $\sim 500 \mu\text{m}$  thick) was comprised of a bulk layer with a solids ratio of 40/60 vol.% Ni/YSZ (and approximately 30 vol.% porosity), and a 5–10  $\mu\text{m}$  thick active anode layer with 50/50 vol.% solids Ni/YSZ. The sintered thickness of the YSZ membrane was 5–10  $\mu\text{m}$  thick. All cathode and  $\text{Ce}_{0.8}\text{Sm}_{0.2}\text{O}_{1.9}$  (SDC-20) powders used in this investigation were synthesized using a glycine-nitrate combustion technique [2]. Post-synthesized powders were typically calcined from  $1000$  to  $1200^\circ\text{C}$  for 1 h, and then attrition milled for 10–30 min to achieve the desired particle size distribution (typically  $d_{50} < 1 \mu\text{m}$ ,  $d_{90} < 2 \mu\text{m}$ ). SDC-20 interlayers ( $\sim 5 \mu\text{m}$  post-sintered thickness) were applied to creep-flattened anode substrates via screen-printing, and sintered from  $1100$  to  $1300^\circ\text{C}$  for 2 h.

\* Corresponding author. Tel.: +1-509-943-6264; fax: +1-509-375-2186.  
E-mail address: steven.simner@pnl.gov (S.P. Simner).

The cathodes were also applied by screen-printing (25–40  $\mu\text{m}$  post-sintered thickness). Cathode compositions were typically sintered from 1100 to 1250 °C. The diameter of the anode support was 25 mm, and that of the screen-printed cathode initially 22 mm. Recently, however, concerns of chemical interaction between the cathode and the seal material have led to a decrease in the cathode diameter to 19.5 mm. The cathode area was used as the active cell area to calculate current and power densities. Screen-printed Pt grids with embedded Pt gauze, and screen-printed NiO grids with embedded Ni gauze were used as current collectors for the cathode and anode, respectively. Figs. 1 and 2 show a schematic of the single cell set-up, and a photo of the cell (air side) in place on the test fixture, respectively. The cells were sealed to alumina test fixtures using Aremco cements, and current–voltage data recorded from 700 to 850 °C using an Arbin BT2000 potentiostat–galvanostat electrochemical testing system. Cells were held at 0.7 V and periodically subjected to current sweeps from 0 to 7 A. A 97%  $\text{H}_2$ –3%  $\text{H}_2\text{O}$  gas mixture was flowed to the anode at 200 sccm, and air to the cathode at 300 sccm. At least two samples of each cathode composition were analyzed to verify cell performances. Thermal expansion in air was conducted on sintered bars ( $\sim 25 \text{ mm} \times 3 \text{ mm} \times 3 \text{ mm}$ ) using a Unitherm model 1161 dilatometer.

### 3. Results and discussion

It is important to note that the studies reported in this paper have been conducted over an 12–18-month period, during which time the performance of the base LSF material has periodically changed to a small degree, apparently coinciding with the use of newly synthesized powder

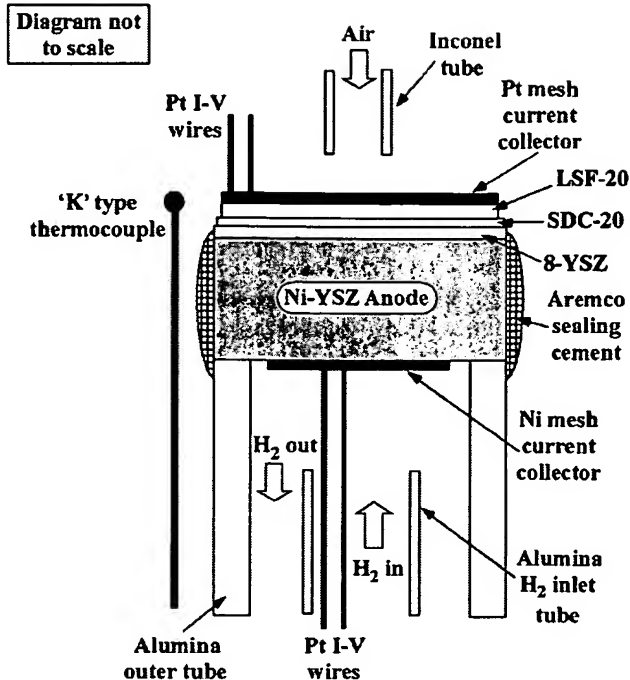


Fig. 1. Schematic of single cell apparatus.

batches. Laboratory scale processing typically enables the production of a 200 g batch of powder, and approximately every 3 months a new batch is required. Despite maintaining established protocols for powder synthesis each powder batch indicates a slight degree of performance variation. As such it is not possible to directly compare each and every result to be presented in this paper. However, within each given investigation all powders used were taken from the same synthesis batch, and hence at the very least these

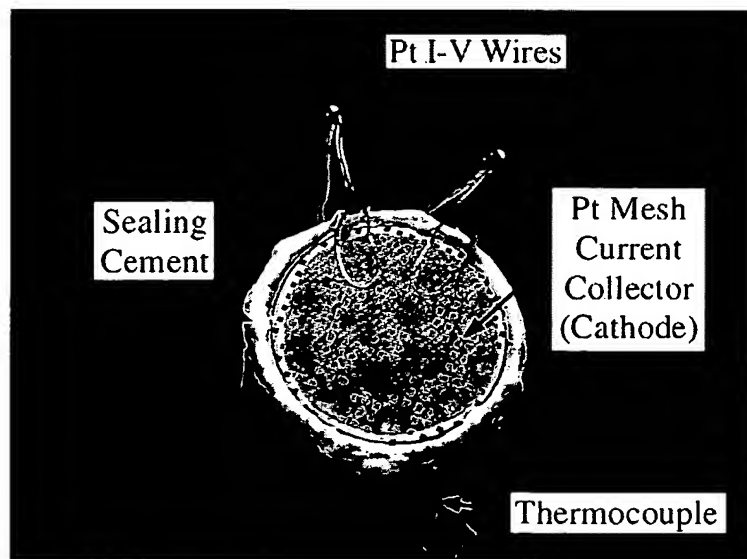


Fig. 2. Photograph of single cell apparatus—cathode side.

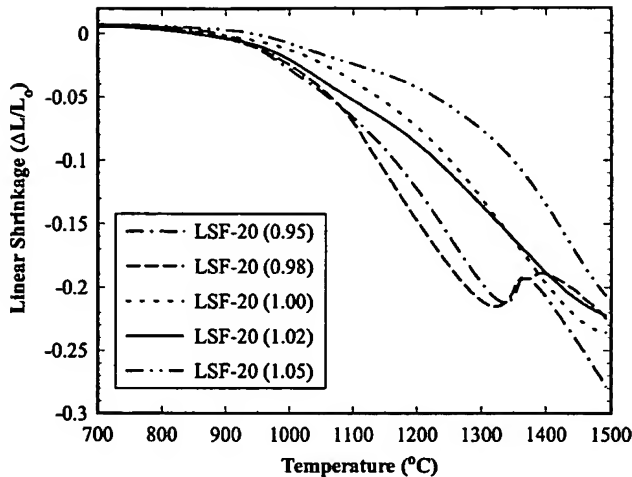


Fig. 3. Sintering shrinkage behavior of  $(La_{0.8}Sr_{0.2})_xFeO_{3-\delta}$  ( $x = 0.95$ – $1.05$ ).

results can be confidently compared and hopefully accurate conclusions drawn.

### 3.1. Non-stoichiometric $(La_{0.8}Sr_{0.2})_xFeO_{3-\delta}$ compositions

Many perovskites, in particular lanthanum chromites [3–5], exhibit markedly different sintering characteristics with small variations in A/B stoichiometry. Varied sintering characteristics can in turn lead to over- or under-sintering of the cathode (at a given temperature), and subsequent

performance reduction due to lack of porosity or insufficient cathode adherence. Slight variations in the A/B ratio are, however, not expected to significantly affect physical characteristics such as electrical conductivity and thermal expansion. Compositions of the form  $(La_{0.8}Sr_{0.2})_xFeO_{3-\delta}$ , where  $x = 0.95, 0.98, 1.00, 1.02$  and  $1.05$ , were considered. Fig. 3 shows the sintering shrinkage behavior of the investigated compositions (calcined at  $800$  °C/4 h). To provide an idea of the varied sintering behaviors of these compositions, for  $x = 0.98$  a 15% shrinkage is achieved by  $\sim 1150$  °C compared to  $1350$  °C for  $x = 1.05$ . A-site depleted samples exhibit enhanced densification while B-site depleted compositions show retarded sintering behavior compared to the stoichiometric A/B = 1 composition. Fig. 4 shows XRD traces for each composition after calcination at  $1200$  °C. Compositions with  $x = 1.00$  appeared relatively phase pure (possibly containing a trace phase tentatively identified as  $Sr_7Fe_{10}O_{22}$ ), while samples with  $x > 1.00$  indicated  $SrLaFeO_4$  as an additional phase. Interestingly A/B < 1.00 compositions do not show a precipitated Fe-O phase, and A/B > 1.00 no La-O phases.  $La_2O_3$  is often observed in B-site depleted manganites and chromites, and extremely detrimental to sample integrity due to hydration, and subsequent volume expansion, of the oxide. Fig. 5(a) and (b) indicate I–V data at  $700$  °C for the aforementioned compositions (sintered at  $1150$  °C/2 h) at 0 h (start of test) and 72 h. For diagram clarity the power curves have been omitted but power densities can be easily established knowing the active cathode area is  $3\text{ cm}^2$ . Not surprisingly, the  $x = 1.00$

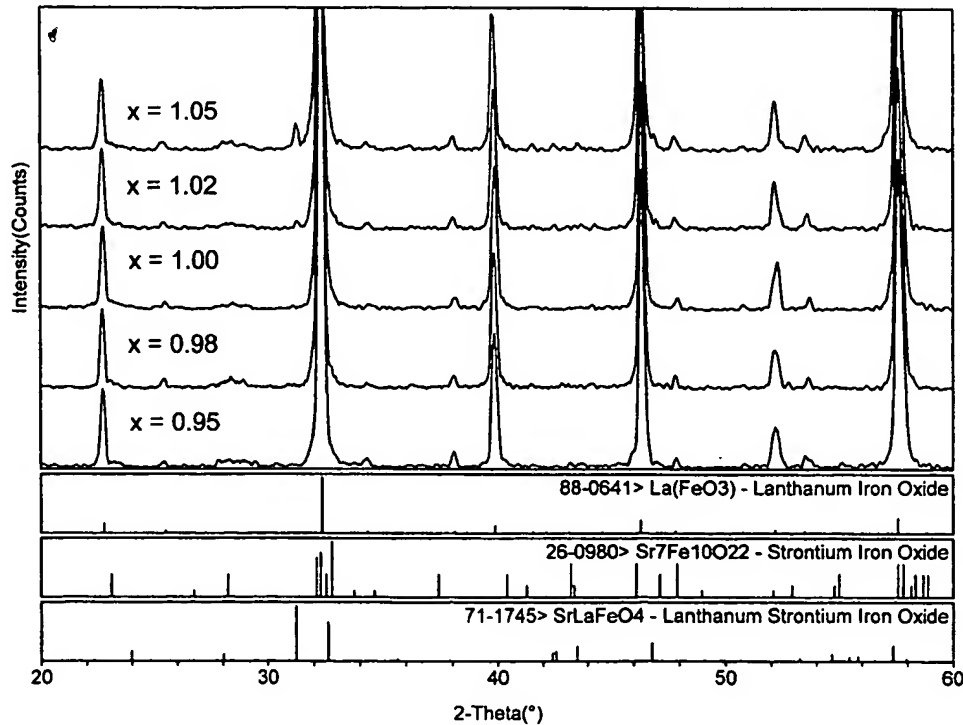


Fig. 4. X-ray diffraction data for  $(La_{0.8}Sr_{0.2})_xFeO_{3-\delta}$  ( $x = 0.95$ – $1.05$ ) after calcination at  $1200$  °C.

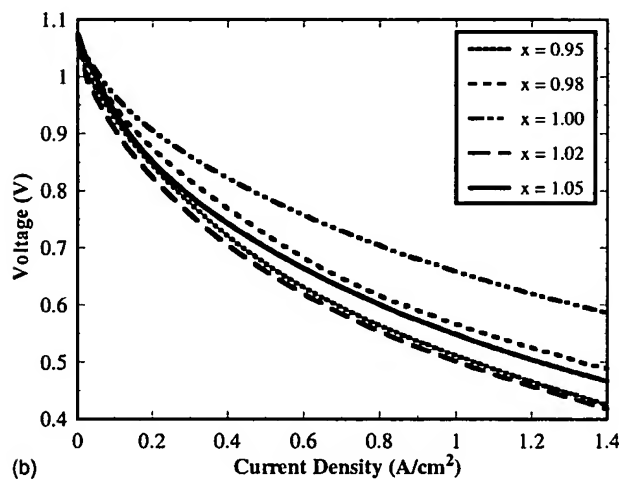
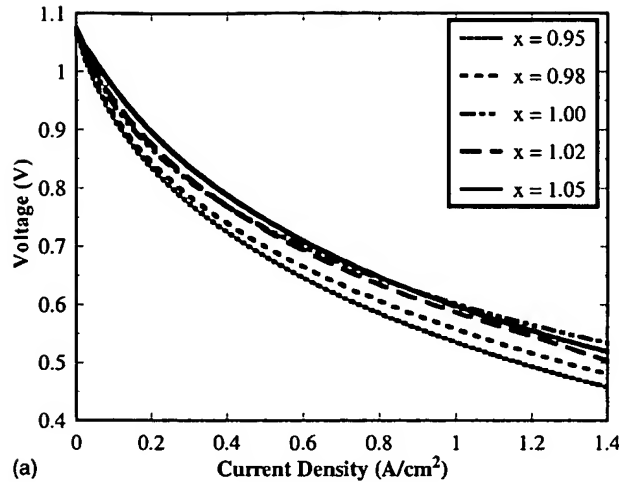


Fig. 5. Current-voltage data for  $(La_{0.8}Sr_{0.2})_xFeO_{3-\delta}$  ( $x = 0.95$ – $1.05$ ) at  $700$  °C after (a)  $0$  h, and (b)  $72$  h.

composition indicates the best cell performance for cathodes sintered at  $1150$  °C. This sintering temperature had previously been established as the optimum sintering temperature for LSF-20 ( $x = 1.00$ ) [1], and hence the non-stoichiometric compositions are likely either over-sintered (for  $x < 1.00$ ) or poorly adhered (for  $x > 1.00$ ). Indeed SEM of the LSF-20 ( $x = 0.95$ ) sample (Fig. 6) indicates coarser particles in both LSF and Sm-doped ceria (SDC) layers compared to LSF-20 ( $x = 1.00$ ) (Fig. 7). Larger particles in the LSF-20 ( $x = 0.95$ ) are simply due to over-sintering (coarsening) of the microstructure. The disparity between the morphology of the SDC layer for  $x = 0.95$  and  $1.00$  is explained by the presence of high proportions of Fe in the SDC interlayer (detected by EDX). As will be described in greater detail later in this paper the incorporation of transition metal cations into the SDC layer can have a marked affect on the sintering and microstructural evolution of this layer. It may be possible to sinter the LSF-20 ( $x < 1.00$ ) compositions at lower temperatures to prevent particle coarsening and Fe diffusion into the SDC layer, but with

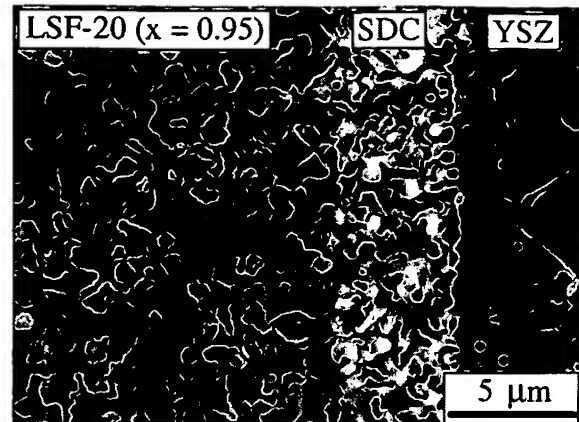


Fig. 6. SEM micrograph of an anode-supported YSZ cell utilizing a  $(La_{0.8}Sr_{0.2})_{0.95}FeO_{3-\delta}$  cathode sintered at  $1150$  °C for  $2$  h.

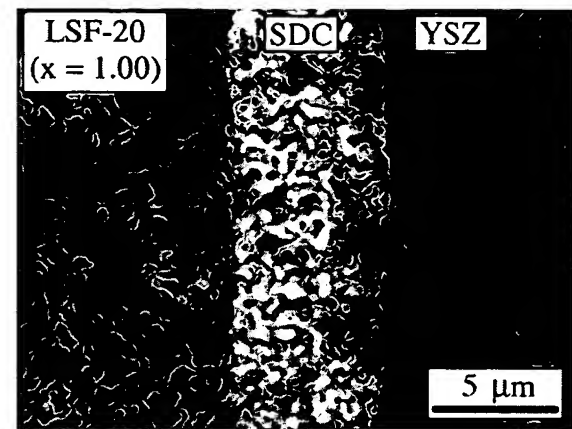


Fig. 7. SEM micrograph of an anode-supported YSZ cell utilizing a  $La_{0.8}Sr_{0.2}FeO_{3-\delta}$  cathode sintered at  $1150$  °C for  $2$  h.

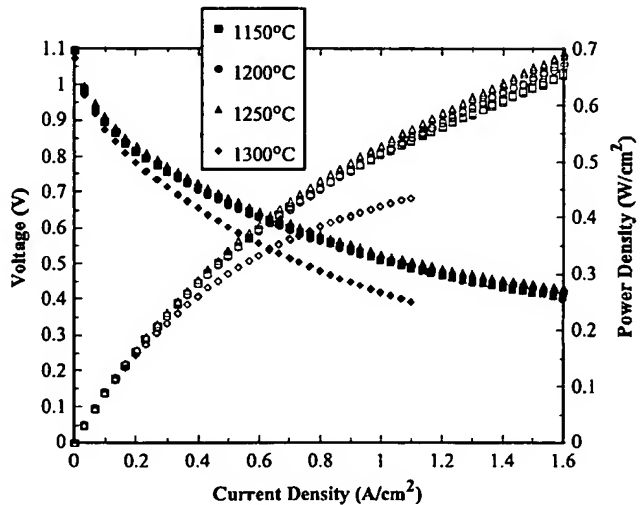


Fig. 8. Current-voltage data at  $700$  °C for an anode-supported YSZ cell utilizing a  $La_{0.8}Sr_{0.2}FeO_{3-\delta}$  cathode ( $1150$  °C/ $2$  h) and  $Ce_{0.8}Sm_{0.2}O_{1.9}$  interlayer ( $1150$ – $1300$  °C/ $2$  h).

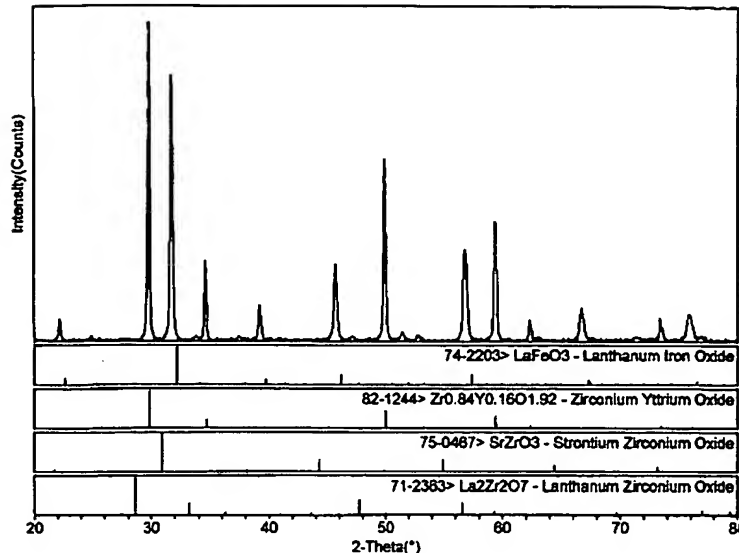


Fig. 9. X-ray diffraction data indicating no Sr-La zirconate formation after reaction of 8-YSZ and LSF-20 at 1200 °C for 2 h.

respect to the LSF-20 ( $x > 1.00$ ) samples, which appear to be under-sintered, using higher temperatures is probably not possible for two reasons. Firstly, above 1200 °C YSZ reacts with doped ceria to form a resistive interfacial layer [6]—Fig. 8 illustrates reduced performance for cells with SDC interlayers applied above 1250 °C. Secondly, preliminary studies on LSF cathode-supported cells at PNNL have shown that above  $\sim 1250$  °C La readily diffuses from the cathode into the SDC layer—studies by Eguchi et al. [7] indicate that La incorporation reduces the ionic conductivity of doped ceria materials. What this does indicate is that slight variations in stoichiometry can dramatically affect the cell performance, and that highly accurate standardization of precursor solutions is required to ensure optimal and reproducible data. As expected, the thermal expansion of LSF-20 showed little dependence on the A/B ratio, and was measured to be between  $12.50 \times 10^{-6}$  and  $12.65 \times 10^{-6}$  °C $^{-1}$  for LSF-20 ( $x = 0.95$ –1.05) (25–1200 °C).

### 3.2. SDC with transition metal dopants

The exact role of the Sm-doped ceria layer has not been established though previous data at PNNL has indicated significant performance improvements when the ceria layer is present between the LSF cathode and the YSZ electrolyte [8]. Reaction of iso-statically pressed LSF-20 and YSZ powder mixtures at 1200 °C (Fig. 9) indicates no La- or Sr-zirconate formation (this is in agreement with Ralph et al. [9])—zirconate formation is typically observed with cobaltite and manganite cathodes on a YSZ electrolyte [10–14]. However, a small shift in the LSF peak positions indicating increased unit cell volume (240–247 Å $^3$ ) is apparent. Even after reaction at 1400 °C for 24 h no zirconate phases could be positively identified, though trace phases (with peak intensities barely above background) indicated possible

matches with SrFe<sub>12</sub>O<sub>19</sub>, ZrO<sub>2</sub>, SrZrO<sub>3</sub>, SrY<sub>2</sub>O<sub>4</sub> and Sr<sub>2</sub>Zr<sub>2</sub>O<sub>7</sub>. This aforementioned peak shift (LSF–YSZ reacted at 1200 °C) phenomenon and its implications are under investigation, and will be reported in a future article. Currently, it is assumed that the improved cell performance observed when a ceria layer is present is a consequence of the higher ionic conductivity and surface exchange kinetics of SDC relative to YSZ.

Though the precise function of the SDC layer is not understood, it is generally accepted that since this layer is an ionic conductor (and hence an extension of the electrolyte), it should be of sufficiently high density to maximize ionic transport through the layer, and cathode reaction sites at the LSF–SDC interface. However, the SDC layer is applied onto a post-sintered anode–YSZ substrate (rather than co-fired with the anode support) to avoid detrimental SDC–YSZ interactions at the anode-support firing temperature close to 1400 °C. As such, sintering of the SDC is

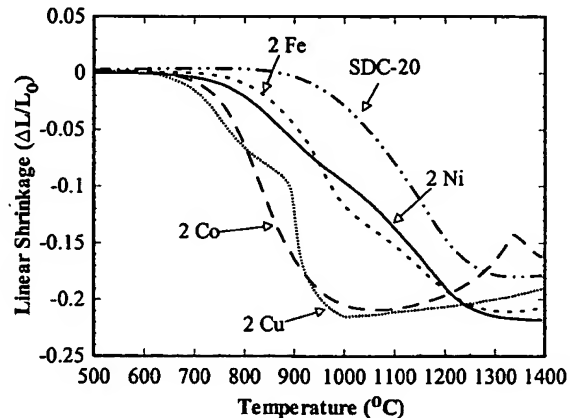


Fig. 10. Sintering shrinkage data for Ce<sub>0.8</sub>Sm<sub>0.18</sub>M<sub>0.02</sub>O<sub>1.9</sub> compositions where M = Co, Cu, Fe and Ni.

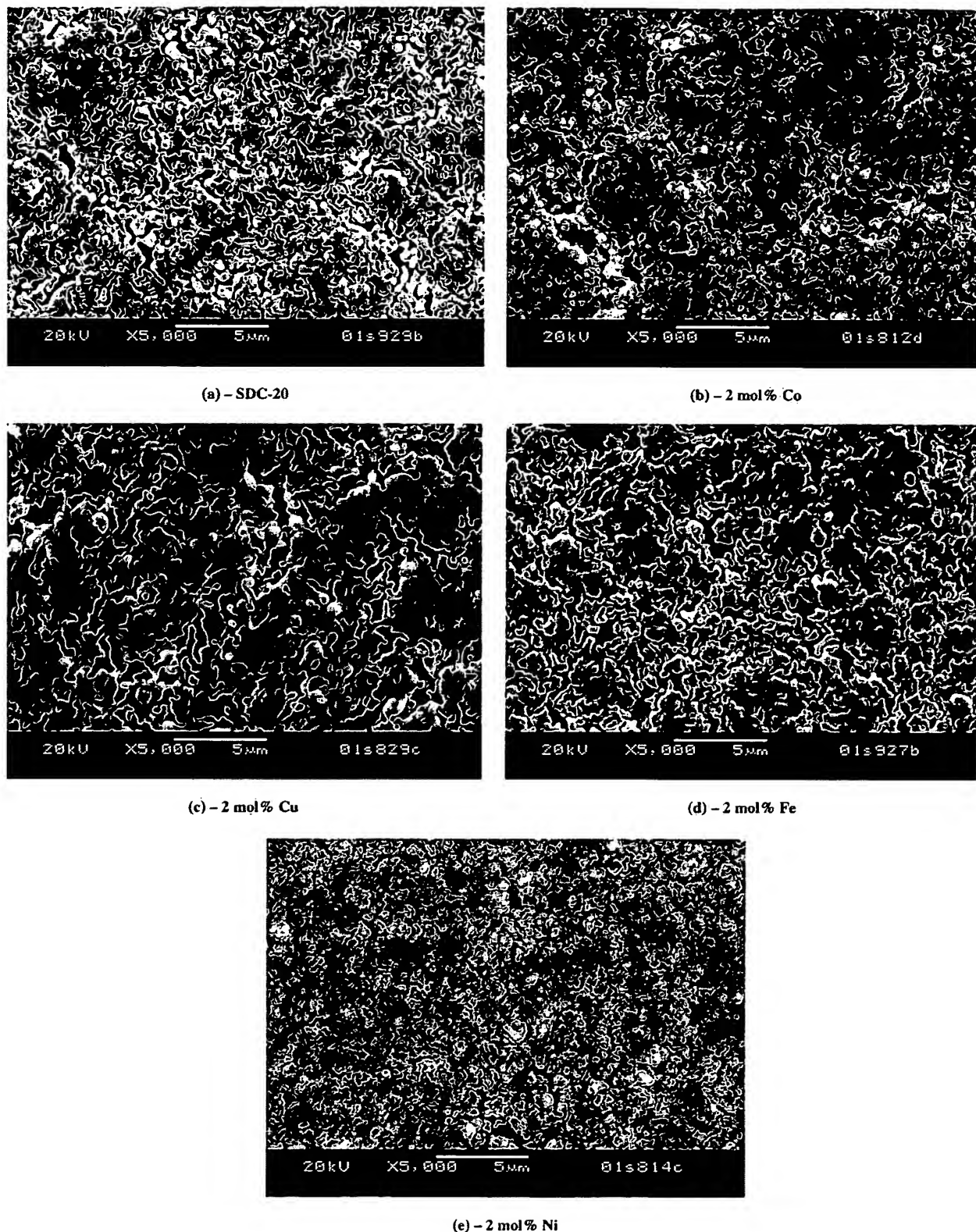


Fig. 11. SEM micrographs of screen-printed  $\text{Ce}_{0.8}\text{Sm}_{0.18}\text{M}_{0.02}\text{O}_{1.9}$  films sintered onto the post-sintered anode-YSZ substrate—fired between 1000 and 1200 °C. (a) SDC-20; (b) 2 mol% Co; (c) 2 mol% Cu; (d) 2 mol% Fe; (e) 2 mol% Ni.

restricted to the “z” direction since the “x–y” plane remains constrained by the anode–YSZ support. There are of course many processing techniques that would yield a highly densified ceria layer such as PVD, ECVD, etc., though these methods are both slow and expensive, and a universal goal within the SOFC community is to develop an economical and commercially viable SOFC system. In an attempt to improve the sinterability of the SDC layer, 2 mol% of transition metal dopants were added to the SDC to give compositions  $\text{Ce}_{0.8}\text{Sm}_{0.18}\text{M}_{0.02}\text{O}_{1.9}$  (where M = Co, Cu, Fe and Ni). Fig. 10 indicates the sintering shrinkage behavior of bulk samples of these materials. Similar findings were observed by Kleinlogel and Gauckler [15]. Each transition metal dopant addition produces enhanced sintering behavior with a lower sintering onset temperature than SDC-20 with no additional dopants. The subsequent expansion of the Cu- and Co-doped samples is the result of entrapped air where the surface of the sample has fully densified, so that any trapped air expands on further heating causing the sample to bloat. Figs. 11a–e show screen-printed layers of the aforementioned transition metal doped compositions, which were sintered from 1000 to 1200 °C. None of the compositions shows improved density compared to the base SDC material, and subsequent single cell testing with identical cathodes indicated the highest power densities for cells using the standard SDC material. Hence, although it's possible to improve the bulk sintering of SDC-20 with transition metal dopants, the “x–y” sintering restriction of the screen-printed layers still prevents complete densification of the ceria interlayer. Current studies are focused on improving the particle packing of the screen-printed layer to yield a higher green density and hence post-fired density.

### 3.3. LSF-20–SDC-20 cathode mixtures

Mixed LSM–YSZ compositions have received considerable attention, and show improved cell performance over pure LSM cathodes. As such, 20–60 wt. % SDC proportions were added to LSF-20 cathodes to evaluate the affects of incorporating a pure ionic conducting phase. The LSF–SDC layer was incorporated as a thin (5–10 μm) interfacial layer between the SDC and a bulk LSF cathode. Fig. 12 shows cell performances at 750 °C after 1 day of operation. The optimum power density is observed for an LSF-20–SDC-20 (60–40 wt. %) mixture (~650 mW/cm<sup>2</sup> at 750 °C/0.7 V), approximately 150–200 mW/cm<sup>2</sup> lower than pure LSF-20 cathodes. This should probably be expected since LSF-20 is a mixed conductor, and replacement of this phase with SDC may marginally enhance the ionic conductivity of the cathode, but is likely to significantly reduce the electronic conductivity.

### 3.4. Noble metal catalysts

A number of studies have been conducted on the catalytic benefits of small noble metal additions to SOFC cathodes

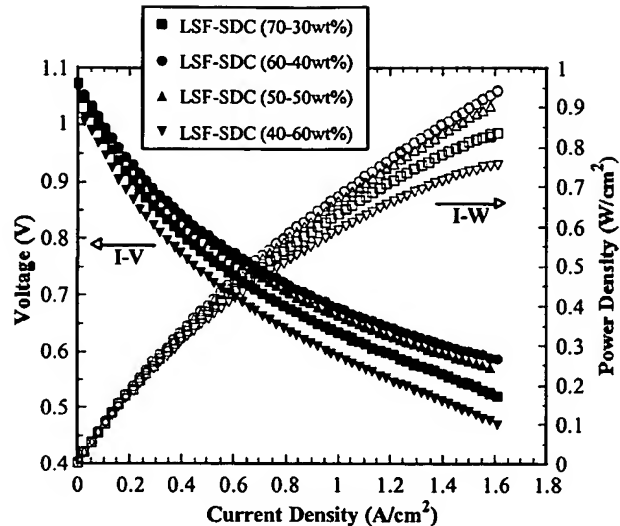


Fig. 12. Current and power density data for  $\text{La}_{0.8}\text{Sr}_{0.2}\text{FeO}_{3-\delta}$   $\text{Ce}_{0.8}\text{Sm}_{0.19}\text{O}_{1.9}$  cathode mixtures.

[16–18]. For this study 1–2 vol. % Pd or Pt was added to either the base LSF-20 or to an LSF-20–SDC-20 (60–40 wt. %) cathode. Noble metals were incorporated into the cathodes via two methods: (1) diammine–palladium (or –platinum)II nitrite (Strem Chemicals) was added to the pre-combusted La–Sr–Fe nitrate solution; (2) high surface area Pd or Pt (~20 m<sup>2</sup>/g, Alfa Aesar) was milled with post-synthesized LSF-20 powders. A thin (~5 μm post-sintered) layer of the Pd/Pt containing cathodes was screen-printed onto the sintered ceria interlayer followed by a bulk LSF-20 cathode (~40 μm post-sintered thickness). Fig. 13 shows an SEM micrograph of a Pd containing cathode. Fig. 14 indicates the performance of 2 vol. % additions of Pd or Pt to the LSF–SDC mix. Compared to the base LSF–SDC the Pd addition results in a 50% power density improvement at 0.7 V/700 °C, whereas the Pt addition affords no discernible enhancement. Similar trends were obtained for Pd/Pt additions to the LSF-20. However, long-term testing of samples incorporating Pd indicates performance instability. Fig. 15 shows a long-term plot (700 °C/0.7 V) for a cell utilizing an LSF-20 cathode with 2 vol. % Pd. After 2 h the performance reached a maximum of ~610 mW/cm<sup>2</sup> followed by a rapid degradation in less than 24 h to <400 mW/cm<sup>2</sup> (comparable to the power density of a cell without Pd additions). Thus, it appears that Pd facilitates initial cathode improvements with respect to the catalytic activity for  $\text{O}_2$  reduction, but this enhancement is not sustainable. A tentative reason for the observed performance decrease may be related to the migration of Pt to the cathode–SDC interface during cell operation. This phenomenon was reported in a previous study conducted at PNNL [8], and is believed to be related to the volatilization of Pt–O species at the surface of the Pt current collector, and subsequent reduction to Pt metal at the cathode–SDC interface; the fact that no Pt is ever observed in the bulk cathode

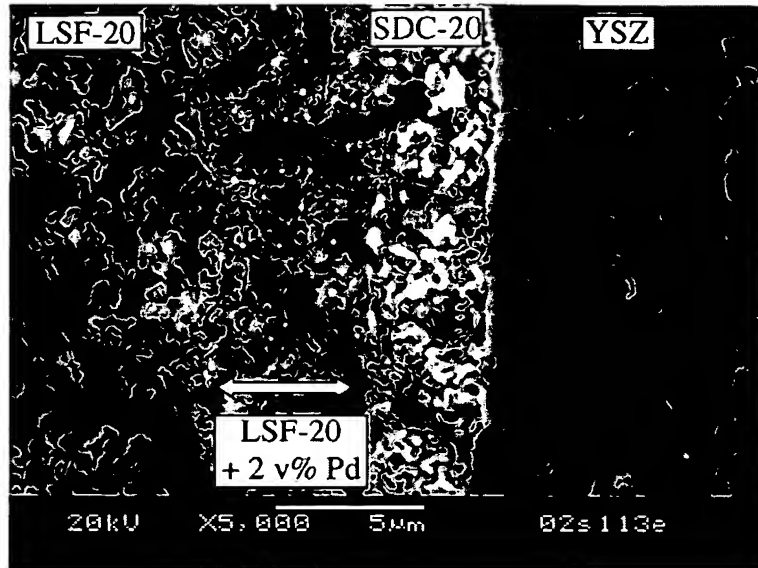


Fig. 13. SEM micrograph of a  $\text{La}_{0.8}\text{Sr}_{0.2}\text{FeO}_{3-\delta}$  bulk cathode with a 5  $\mu\text{m}$   $\text{La}_{0.8}\text{Sr}_{0.2}\text{FeO}_{3-\delta}$  + 2 vol.% Pd active cathode layer.

probably rules out solid state or surface diffusion processes. It should also be noted that this phenomenon only occurs when the cell is discharged electrically for a period of time (rather than being merely held at temperature). SEM/EDX examination of Pd containing cells show that after only 24 h of operation the Pd particles have become significantly alloyed with Pt, which has presumably migrated from the cathode current collector. From Fig. 14 it is evident that Pt does not aid the cathode reaction processes, and the alloying of Pt with the Pd particles may be responsible for the observed degradation phenomenon. Hence, at present it is uncertain if Pd will give long-term improvements in cell performance and the exact role (if any) of Pt the aforementioned instability must be assessed. To accurately establish this, the Pt current collector should be completely removed,

and work is currently underway to design/fabricate an alternative cell fixture configuration that would not require a Pt cathode current collector.

### 3.5. High ionic conductors as interfacial cathode phases

It is generally accepted that improved ionic conductivity with the cathode close to the electrolyte interface should significantly improve the cathode activity. However, as reported by Ullmann et al. [19] there is a proportional linear relationship between ionic conductivity and thermal expansion coefficient (TEC). The anode support structure has a TEC close to  $12 \times 10^{-6} \text{ }^{\circ}\text{C}^{-1}$ , and hence the need to avoid large thermal mismatches limits the TEC of other cell components. However, it was considered that a very thin

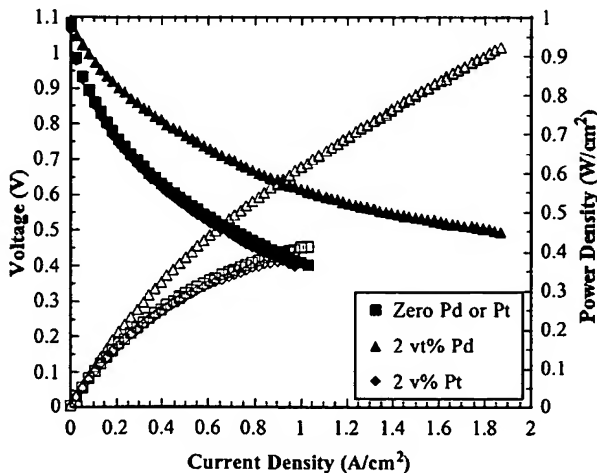


Fig. 14. Current and power density data for  $\text{La}_{0.8}\text{Sr}_{0.2}\text{FeO}_{3-\delta}$  bulk cathodes with  $\text{La}_{0.8}\text{Sr}_{0.2}\text{FeO}_{3-\delta}\text{--Ce}_{0.8}\text{Sm}_{0.2}\text{O}_{1.9}$  (60–40 wt.%) active cathode mixtures containing 2 vol.% Pd or Pt.

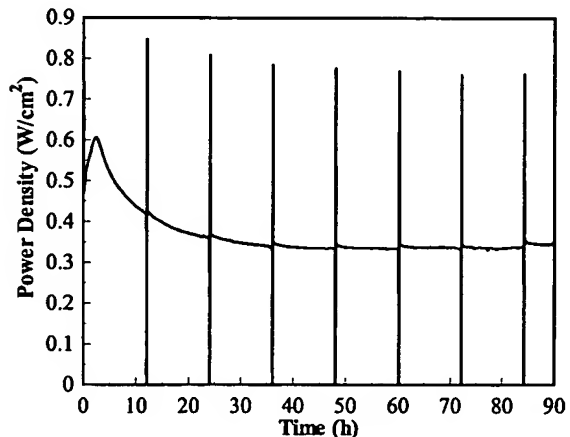


Fig. 15. Long-term performance data at  $700 \text{ }^{\circ}\text{C}/0.7 \text{ V}$  for a  $\text{La}_{0.8}\text{Sr}_{0.2}\text{FeO}_{3-\delta}$  bulk cathode with  $\text{La}_{0.8}\text{Sr}_{0.2}\text{FeO}_{3-\delta}$  active cathode mixture containing 2 vol.% Pd.

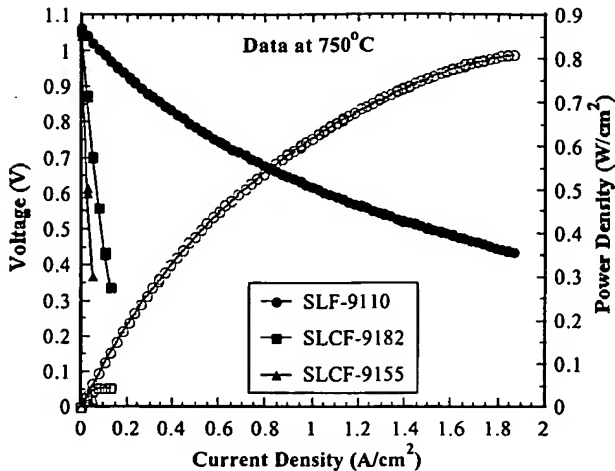


Fig. 16. Current and power density data for  $\text{La}_{0.8}\text{Sr}_{0.2}\text{FeO}_{3-\delta}$  bulk cathodes with thin interfacial  $\text{Sr}_{0.9}\text{La}_{0.1}\text{Co}_x\text{Fe}_{1-x}\text{O}_{3-\delta}$  cathode layers ( $x = 0, 0.2$  and  $0.5$  denoted by SLF-9110, SLCF-9128, and SLCF-9155, respectively).

high ionic conducting layer between the LSF-20 and SDC-20 layers may have less induced stress resulting from any thermal expansion mismatches. Compositions of the type  $\text{Sr}_{0.9}\text{La}_{0.1}\text{Co}_x\text{Fe}_{1-x}\text{O}_{3-\delta}$  ( $x = 0, 0.2$  and  $0.5$  denoted by SLF-9110, SLCF-9128, and SLCF-9155, respectively) were considered. Fig. 16 indicates *IV*-*IW* data for cells incorporating the aforementioned layers at  $750^\circ\text{C}$ . The Co-containing compounds have significantly reduced performance compared to the straight Sr-La-Fe-O compound (SLF-9110), but even this compound indicates considerably lower power densities compared to the base LSF-20 cathode (SLF-9110,  $\sim 525 \text{ mW/cm}^2$ , LSF-20,  $\sim 800 \text{ mW/cm}^2$  at  $750^\circ\text{C}$  /  $0.7 \text{ V}$ ). The phenomenon responsible for the poor performance of these cathode configurations is readily apparent

from the SEM micrograph in Fig. 17, which shows a  $1 \mu\text{m}$  thick interfacial phase, identified by EDX as Sr-Zr-O rich (probably a resistive Sr-zirconate phase), between the SDC interlayer and YSZ electrolyte. Presumably during sintering of the cathode a liquid phase was formed within the SLCF layer, which subsequently wicked through the porous SDC layer and reacted at the YSZ interface. All three compositions indicated the presence of the Sr-Zr-O layer, the thickness of which increased with Co content. Hence, though the SLCF layer appears well adhered without any discernible cracking resulting from potential thermal mismatch induced stresses the presence of the detrimental liquid phase is likely to inhibit the use of the aforementioned interfacial layers or the incorporation of the SLCF phases as a second phase mixed in with the LSF. However, if the resulting reaction layer arises from liquid wicking through the ceria, the ability to better densify the ceria layer may prevent the liquid diffusion to the SDC-YSZ interface and subsequent reaction.

### 3.6. Long-term cell stability

Whilst substantial cathode improvements are still necessary to facilitate increased power densities for low temperature SOFCs, an equally important goal is that of long-term stability. There are many phenomena that can affect long-term cell performance including chemical interaction of adjacent cell components to form insulating phases, volatilization of chemical species (e.g. Cr in the case of Cr containing alloy separator plates), and sintering of the cathode and/or anode. Despite the importance of long-term cell performance, little extended cell data has been presented in the published literature for the array of cathodes currently being studied in the SOFC community. With our own research instability has been observed for  $\text{La}(\text{Sr})\text{CoO}_3$

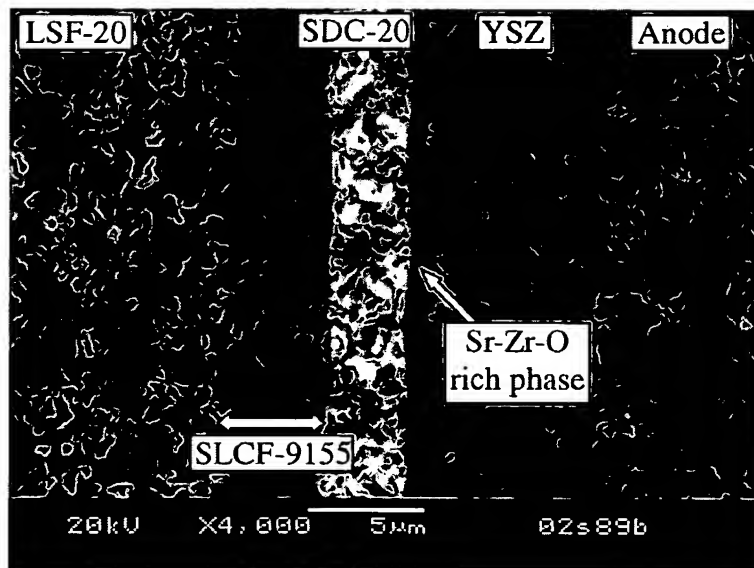


Fig. 17. SEM micrograph depicting Sr-Zr-O rich phase at the YSZ-SDC interface for a cell utilizing a  $\text{La}_{0.8}\text{Sr}_{0.2}\text{FeO}_{3-\delta}$  bulk cathode with a thin interfacial  $\text{Sr}_{0.9}\text{La}_{0.1}\text{Co}_{0.5}\text{Fe}_{0.5}\text{O}_{3-\delta}$  layer.

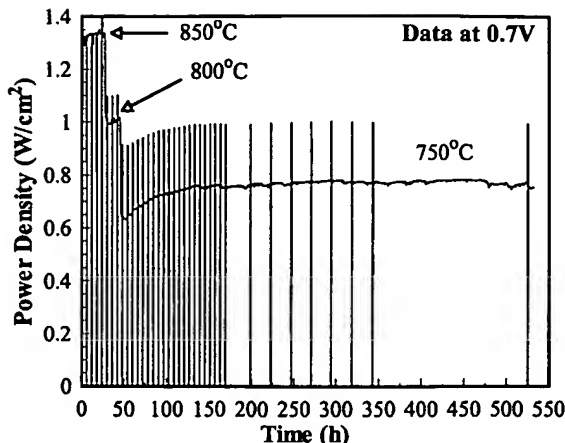


Fig. 18. Long-term performance data for an  $\text{La}_{0.8}\text{Sr}_{0.2}\text{FeO}_{3-\delta}$  cathode at 750 °C and 0.7 V.

and  $\text{La}(\text{Sr})\text{Fe}(\text{Ni})\text{O}_3$  cathodes—the former indicated phase separation and Co diffusion at 750 °C/0.7 V. However, LSF-20 has shown very promising long-term data. Fig. 18 illustrates the most recent long-term performance data of an anode-supported YSZ cell utilizing a base LSF-20 cathode. After initial data acquisition at 850 and 800 °C the cell was held at 0.7 V and 700 °C, and achieved a power density of 770  $\text{mW/cm}^2$  with no discernible degradation over a 500 h period. The vertical lines on the graph are the result of periodic IV sweeps.

#### 4. Conclusions

Research with respect to improved activity SOFC cathodes is of paramount importance to realize the commercialization of low temperature (high performance) SOFCs. At PNNL reasonable success has been achieved towards this goal with the use of anode-supported SOFCs utilizing a thin YSZ electrolyte and Sr-doped lanthanum ferrite cathode. Current studies (not all detailed in this paper) involve optimizing the base LSF-20 cathode with respect to microstructure and thickness, the incorporation of high electronic conducting bulk cathodes, e.g. lanthanum nickel ferrites, with an LSF-20 active cathode layer to reduce sheet resistances and aid current collection, engineering the cathode–ceria interlayer interface to maximize the contact area (triple phase boundaries), maximizing the sintered density of the ceria layer (since it is essentially an extension of the electrolyte), understanding the role of the ceria interlayer to enable possible removal of said layer while maintaining high performance (previous tests have shown more than a doubling in power density for an YSZ–SDC–LSF configuration compared to YSZ–LSF), compositional modification of the base LSF-20 material to induce higher electronic/ionic conductivities, and the addition of noble metal phases to an active cathode layer to enhance the oxygen reduction reaction. As demonstrated by this article not all of these research

avenues will necessarily lead to improved cathode performance, but it is envisaged that they will provide a better understanding of this particular cathode system, and a basis on which to eventually exact significant enhancements in low temperature power and cell longevity.

#### Acknowledgements

The authors would like to thank Jim Coleman for SEM/EDX analysis. The work summarized in this paper was funded as part of the Solid-State Energy Conversion Alliance (SECA) Core Technology Program by the US Department of Energy's National Energy Technology Laboratory (NETL). PNNL is operated by Battelle Memorial Institute for the US Department of Energy under Contract DE-AC06-76RLO 1830.

#### References

- [1] S.P. Simner, J.F. Bonnett, N.L. Canfield, K.D. Meinhardt, V.L. Sprenkle, J.W. Stevenson, *Electrochim. Solid State Lett.* 5 (7) (2002) A173.
- [2] L.A. Chick, L.R. Pederson, G.D. Maupin, J.L. Bates, L.E. Thomas, G.J. Exarhos, *Mater. Lett.* 10 (1–2) (1990) 6.
- [3] S.P. Simner, J.S. Hardy, J.W. Stevenson, T.R. Armstrong, *J. Mater. Sci.* 34 (1999) 5721.
- [4] S.P. Simner, J.S. Hardy, J.W. Stevenson, T.R. Armstrong, *J. Mater. Sci. Lett.* 19 (2000) 863.
- [5] L.A. Chick, J. Liu, J.W. Stevenson, T.R. Armstrong, D.E. McCready, G.D. Maupin, G.W. Coffey, C.A. Coyle, *J. Am. Ceram. Soc.* 80 (8) (1997) 2109.
- [6] K. Eguchi, N. Akasaka, H. Mitsuyasu, Y. Nonaka, *Solid State Ionics* 135 (2000) 589.
- [7] K. Eguchi, T. Setoguchi, T. Inoue, H. Arai, *Solid State Ionics* 52 (2000) 165.
- [8] S.P. Simner, J.W. Stevenson, K.D. Meinhardt, N.L. Canfield, *Solid oxide fuel cells VII*, in: H. Yokokawa, S.C. Singhal (Eds.), *The Electrochemical Society Proceedings Series*, Pennington, NJ, 2001, PV 2001-16, p. 1051.
- [9] J.M. Ralph, J.T. Vaughney, M. Krumpelt, *Solid oxide fuel cells*, vol. VII, in: H. Yokokawa, S.C. Singhal (Eds.), *The Electrochemical Society Proceedings Series*, Pennington, NJ, 2001, PV 2001-16, p. 466.
- [10] M. Mori, T. Abe, H. Itoh, O. Yamamoto, G.Q. Shen, Y. Takeda, N. Imanishi, *Solid State Ionics* 123 (1999) 113.
- [11] H.Y. Lee, S.M. Oh, *Solid State Ionics* 90 (1996) 133.
- [12] A. Mitterdorf, L.J. Gauckler, *Solid State Ionics* 111 (1998) 185.
- [13] G.C. Kostogloudis, G. Tsiniarakis, C. Ftikos, *Solid State Ionics* 135 (2000) 529.
- [14] F.M. Figueiredo, J.A. Labrincha, F.M.B. Marques, *Solid State Ionics* 101–103 (1997) 343.
- [15] C. Kleinlogel, L.J. Gauckler, *Solid Oxide Fuel Cells VI*, in: H. Yokokawa, S.C. Singhal (Eds.), *The Electrochemical Society Proceedings Series*, Pennington, NJ, 1999, PV 99-19, p. 225.
- [16] J.W. Erning, T. Hauber, U. Stimming, K. Wippermann, *J. Power Sources* 61 (1996) 205.
- [17] H. Uchida, S. Arisaka, M. Watanabe, *Solid State Ionics* 135 (1–4) (2000) 347.
- [18] M. Sahibzada, S.J. Benson, R.A. Rudkin, J.A. Kilner, *Solid State Ionics* 113–115 (1998) 285.
- [19] H. Ullmann, N. Trofimienko, F. Tietz, D. Stöver, A. Ahmad-Khanlou, *Solid State Ionics* 138 (1–2) (2000) 79.